Development of Moving Particle Semi-Implicit Method for Simulating Sodium-Water Chemical Reactions in SFR

(高速炉におけるナトリウム-水反応に関する粒子法シミュレーションの開発)

李　佳智

Acknowledgements

Foremost, I would like to express my sincere gratitude to my supervisor Prof. Yamaguchi for his continuous encouragement to support me to complete my Ph.D study, for his patience to allow me making mistakes again and again, and for his guidance on assisting me to make progression of my research. Without his assistance and care, I could never finish this research work.

I also would like to thank Prof. Takata for his immense knowledge to help me have a better understanding of my research topic and help me overcome many difficulties in the research. My sincere gratitude also goes to Dr. Uchibori who spent considerable working time preparing SERAPHIM results for the validation work in this thesis.

I wish to acknowledge Prof. Koshizuka, Prof. Sakai and Prof. Morita for their serious and valuable comments on my research. Without their professional judgement, I could never realize what the highest level of research looks like and could not have a correct self-evaluation on my current work. I appreciate to have their participance in my oral defence to improve my work.

Besides the above help I got concerning my research, I also get the assistance from many people in Yamaguchi laboratory in many aspects of life. Most importantly I would like to express my gratitude to Kakuta san without whom I could not even submit my thesis and continue my study here. Thanks to her always concern, I could refresh myself every time when I felt frustrated and helpless. Without her patient teaching on good manners to me, I could not get the chance to correct myself to become a better person in my future life. I also would like to thank other students in this lab, Yi san, Tan san, Asano san, Nakamura san and Tokoro san, for sharing the same feelings and getting comfort from them. I am grateful to meet you all in my Ph.D. study. I also would like to thank Dr. Jang who provides me the training on experiencing the power harassment for the first time before I start my career life. With his help in the past few years, I become much stronger to deal with such treatment.

Finally, I would like to express my gratitude to my parents, my sister and my girlfriend for their concern on me always. It seems to take pretty long time and much effort for me complete the story of my final study life. I'm looking forward to new adventures in my following life.

JIAZHI LI

Abstract

Liquid sodium as the excellent coolant in the Sodium-cooled faster reactor has the superiority of high thermal conductivity and a large margin to sodium boiling, while it also poses safety issues due to its intense chemical reactivity with water and oxygen. Experimental investigation on the sodium reactivity is limited by the opaque property of liquid sodium. Particle methods are superior to field approaches for investigating sodium-water reaction in terms of its simplicity for modelling chemical reaction without restriction by the flow regime. In the present thesis, a multi-disciplinary, multi-component and multi-phase methodology using the moving particle semi-implicit method (MPS) for simulating sodium-water reactions has been proposed.

The original MPS method was developed for the free-surface flow simulation, whereas it suffers from the limitation of being not applicable to a multiphase and chemical reaction models. To start with, the original MPS is extended with the capability of simulating multi-density flows with high stability, through suppressing the pressure oscillation with modifications on pressure gradient and poison equations. Moreover, a contoured surface tension model with a proposed approach of curvature calculation is applied for depicting the multiphase model.

Two reaction models, reactions of water vapor with liquid sodium and gas-phase sodium, are developed by means of discrete methods in this research. The former one, named as surface reaction, is modelled under the assumption of an infinite reaction rate upon water vapor approaches to the interface by convection. At the same time, the latter gas-phase reaction adopting an empirical equation of reaction rate is competitive to the surface reaction. Particles containing multiple components of reaction products are modelled with the consideration of component diffusion among neighbouring particles.

The present methodology is applied to simulate a configuration with tube bundles where chemical reaction takes place between leaked water vapor and liquid sodium. The distribution of build-up products and temperature are investigated and evaluated. Validation is done by comparing the simulation results from the proposed particle method to that calculated in a mesh-based code, SERAPHIM. Results show the similarity in terms of the temperature distribution of the reaction zone. By implementing the present methodology, the sodium-water chemical reaction is available for further investigation by particle methods.

Key words: Sodium water reaction, Particle methods, MPS, Chemical reaction simulation, Sodium cooled fast reactor

Contents

Acknowledgements **i**

Abstract **iii**

List of figures **vii**

List of tables **ix**

Nomenclatures **xi**

1 Introduction **1**
1.1 Background of Sodium-Water Incidents in SFR 1
1.2 Observation in Experimental Research 2
1.3 Overview of Numerical Methods for SWR Simulation 3
1.4 Motivation and Objectives 5

2 Particle Methods for Multi-phase and Multi-component Flow **7**
2.1 MPS Methods 8
2.2 Pressure Solver 9
2.3 Surface Tension Force 14
2.4 Variable Density Flow 23
2.5 Multi-Component Particles 24

3 Sodium-Water Reaction Models **27**
3.1 Review of Sodium-Water Reactions 27
3.2 Assumptions for Simplification of Modelling 28
3.3 Surface Reaction Model 29
3.4 Gas-Phase Reaction Model 32
3.5 Evaporation and Condensation 33
3.6 Modelling of Reaction Energy 35
3.6.1 Enthalpy and Heat Transfer 35
3.6.2 Governing Equations 37
3.6.3 Numerical Procedure 38

4 Simulation and Verification **43**
4.1 Particle and Time-Step Size 43
4.2 Analytical Conditions 44
4.3 Investigation of Simulation Results 45
4.3.1 Velocity Field 45
4.3.2 Distribution of Reactants and Products 47
4.3.3 Temperature Field 49
4.4 Verification of Mass and Energy Conservation 49

5 Application in Configuration with Tube Bundles **63**
5.1 Simulation with a Single Tube 64
5.2 Simulation with Multiple Tube Bundles 65
5.3 Simulation in a Full-Scale Steam Generator 66
5.4 Comparison to SERAPHIM Results 67

6 Conclusions **93**

Bibliography **95**

List of Figures

2.1 Schematic view of the hydrostatic pressure model 13
2.2 Pressure evolution at the bottom center of the wall layer 14
2.3 Schematic view of the dam break model 15
2.4 Pressure evolution at the right bottom corner of the wall 16
2.5 Pressure profiles of Case 0 and Case 1 at t = 1.3s 17
2.6 Pressure profiles of Case 2 and Case 3 at t = 1.3s 18
2.7 Pressure profiles of Case 4 and Case 5at t = 1.3s 19
2.8 Pressure profiles and interface curvatures in the bubble rising model at t=0.1 . 21
2.9 Pressure profiles and interface curvatures in the bubble rising model at t=1.0 . 22
2.10 Pressure profiles and interface curvatures in the bubble rising model at t=3.0 . 22

3.1 Schematic of surface reaction model and gas-phase reaction model 28
3.2 Dependence of binary diffusivity coefficient between H_2O and H_2 on temperature 30
3.3 Dependence of rate constant on the temperature 32

4.1 Absolute velocity profile at 5ms and 10ms 46
4.2 Mole amount distribution of H_2O at 1, 5, 10 15ms 51
4.3 Mole amount distribution of H_2 at 1, 5, 10 15ms 52
4.4 Mole amount distribution of Na Vapor at 1, 5, 10 15ms 53
4.5 Mole amount distribution of NaOH Vapor at 1, 5, 10 15ms 54
4.6 Volume fraction of H_2 at 1, 5, 10 15ms 55
4.7 Evolution of molar amount of H_2O, H_2, Na(g), NaoOH(g), Na(l), NaoOH(l) within 20 ms. 56
4.8 Vapor fraction of NaOH within 20 ms. 57
4.9 Temperature Profile at 1, 5, 10 and 15 ms 58
4.10 Time-averaged temperature profile in 1, 5, 10 and 15ms 59
4.11 Mass conservation of element H, O and Na 60
4.12 Enthalpy conservation over 20ms 61

5.1 Model configuration with a single tube 64
5.2 Transient temperature profile 70
5.3 Mole amount distribution of H_2O vapor at 10, 20, 40 and 60 ms 71
5.4 Mole amount distribution of H_2 at 10, 20, 40 and 60 ms 72
5.5 Model configuration with 21 tubes 73

5.6 Transient temperature profile 74
5.7 Time-averaged temperature profile within 10 and 20ms respectively 75
5.8 Molar evolution of six species within 60 ms. 76
5.9 Enthalpy evolution of six species within 60 ms. 77
5.10 Conservation of mass and enthalpy within 60ms 78
5.11 Mole amount distribution of H_2O vapor at 10, 20, 40 and 60 ms 79
5.12 Time-averaged mole amount of H_2O vapor within 10, 20, 40 and 60 ms 80
5.13 Mole amount distribution of H_2 at 10, 20, 40 and 60 ms 81
5.14 Volume fraction of $H2O$ and H_2 at 20ms 82
5.15 Mole amount distribution of Na vapor at 10, 20, 40 and 60 ms 83
5.16 Mole amount distribution of $NaOH$ liquid at 10, 20, 40 and 60 ms 84
5.17 Diffusion coefficient of H_2O among gaseous particles at 10, 20, 40 and 60 ms. . 85
5.18 Model configuration of a full-scale steam generator 86
5.19 Time-averaged absolute velocity in [m/s] of gaseous particles from MPS during 1.0-2.0s 87
5.20 Time-averaged gas phase velocity from SERAPHIM during 1.0-2.0s[30] 87
5.21 Time and mass averaged temperature in [^oC] from MPS during 1.0-2.0s 88
5.22 Time-averaged mass-averaged temperature from SERAPHIM during 1.0-2.0s[30] 88
5.23 Time-averaged mole amount of NaOH in [mol] in gaseous particles from MPS during 1.0-2.0s 89
5.24 Time-averaged NaOH from SERAPHIM during 1.0-2.0s[30] 89
5.25 Time-averaged volume fraction of H_2O in gaseous particles from MPS during 1.0-2.0s 90
5.26 Time-averaged volume fraction of H_2O vapor from SERAPHIM during 1.0-2.0s[30] 90
5.27 Time-averaged volume fraction of H_2 in gaseous particles from MPS during 1.0-2.0s 91
5.28 Time-averaged volume fraction of H_2 from SERAPHIM during 1.0-2.0s[30] . . . 91
5.29 Time-averaged void fraction from SERAPHIM during 1.0-2.0s[30] 92

List of Tables

2.1 Illustration of simulated cases with the modifications applied. Case 0 is the original MPS method. 12

3.1 Dimensionless diffusion volumes of investigated species 31
3.2 Coefficients in the rate constant equation 32
3.3 Standard enthalpy of investigated species 36

4.1 Geometric dimensions and initial conditions for simulation cases. 45

5.1 Geometric dimensions and initial conditions for simulation cases. 64
5.2 Initial conditions for an integrated simulation with 95 tubes. 67

Nomenclatures

ρ	Particle mass density	$[kg/m^3]$
t	Time step size	$[s]$
$\mathbf{u}$	Velocity vector of particle	$[m/s]$
μ	Dynamic viscosity	$[N \cdot s/m^2]$
r	Distance between particles	$[m]$
r_e	Effective radius of particle interaction	$[m]$
ω	Weight function	[-]
n_i	Number density of particles i	[-]
n_0	Initial number density of particles	[-]
n^*	Intermediate number density of particles	[-]
N_i	Number of adjacent particles	[-]
N_o	Initial number of adjacent particles	[-]
Φ	Arbitrary scalar of physical variables	[-]
λ	Coefficient in the Laplacian model	$[m^2]$
P	Pressure	[Pa]
γ	A blending parameter	[-]
d	Dimension number	[-]
$\mathbf{C_{ij}}$	Corrective matrix	[-]
β	Parameter for detecting surface particles	[-]
η	Parameter for detecting surface particles	[-]
$\mathbf{v}$	Recoiling velocity vector of particles	$[m/s]$
l_{ij}	Collision distance of particles	$[m]$
l_0	Initial distance of particles	$[m]$
α	Parameter for detecting collision	[-]
σ	Surface tension coefficient	$[N/m]$
κ	Curvature	$[m^{-1}]$
$\mathbf{f_s}$	Vector of surface tension force	$[N]$
C_i	Phase indicator of particle i	[-]
$G(r, r_s)$	Gaussian kernel function	[-]

Γ_{sf}	Surface reaction rate	$[mol/s/particle]$
Mo_g	Total mole of gaseous species	$[mol/particle]$
Mo_i	Total mole of all species	$[mol/particle]$
S	Interfacial area density	$[m^{-1}]$
D_{H_2O}	Effective binary diffusivity	$[m^2/s]$
ΔH^{298}	Standard enthalpy change at 298 K	$[kJ/mol]$
Y_{H_2O}	Volume fraction of H_2O	[-]
$Y_{H_2O,interface}$	Volume fraction of H_2O at the interface	[-]
D_{A-B}	Binary gas phase diffusivity of A in B	$[m^2/s]$
T	Temperature	$[K]$
P_{abs}	Absolute pressure	$[atm]$
$M_A or M_B$	Mole mass of species A or B	$[g/mol]$
ν	Molecular volume	[-]
Z	Molar fraction of species	[-]
$\beta_{l,g}$	Fraction of adjacent liquid sodium number density	[-]
K	Rate constant	[-]
C_p	Molar heat capacity	$[kJ/mol]$
Γ^e	Evaporation rate	$[mol/s/particle]$
Γ^c	Condensation rate	$[mol/s/particle]$
$\Delta h_{l,NaOH}$	Latent heat of $NaOH$	$[kJ/mol]$
$h_{i,m}$	Total enthalpy of species m in particle i	$[kJ]$
k	Heat conductivity	$[W/(m \cdot K)]$
$S_{sf,Na}$	Enthalpy change due to sodium in surface reaction	$[kJ/s]$
$S_{dif,in}$	Enthalpy change due to incoming diffusion	$[kJ/s]$
$S_{dif,out}$	Enthalpy change due to outgoing diffusion	$[kJ/s]$
S_e	Enthalpy change due to evaporation	$[kJ/s]$
S_c	Enthalpy change due to condensation	$[kJ/s]$
C_c	Courant number	[-]
C_d	Diffusion number	[-]

1 Introduction

1.1 Background of Sodium-Water Incidents in SFR

Liquid sodium as the coolant in Sodium-cooled Faster Reactor (SFR) has intense chemical reactivity with leaked water from heat exchanger tubes in the steam generator. Excessive chemical heat generation and corrosive reaction products will deteriorate the integrity of tube bundles. When considering the design of tube bundles and the steam generator, it is required to have the capability to withstand the thermal and mechanical loads induced by the sodium-water reaction.

One concern of the chemical product from the sodium-water reaction is the accumulation of hydrogen. It has the possibility to induce a sequential incident known as hydrogen combustion or explosion. In addition to sodium-water reaction, sodium combustion is a frequent incident as well, which results from sodium leakage into the air. In case of sodium leakage into the containment, sodium concrete reaction takes place and has the potential to threaten the integrity of the containment [1].

In December of 1995, a sodium leakage occurred in the secondary cooling system of Monju, which is a Japanese sodium-cooled faster reactor. Due to the flow induced vibration at a defective weld point, the sodium transportation pipe broke by high cycle fatigue and huge amount of sodium are exposed to the air and concrete. Aggressive reaction of sodium with oxygen and concrete produced sodium compound aerosol and the maximum temperature was estimated above 1000 ^{o}C. The high temperature posed the safety issue on the integrity of structures. Another example of the incident induced by sodium leakage happened in BN-600, which caused insignificant radioactive discharges to atmosphere.

As mentioned, the sodium reaction with water vapor has the characteristic of producing hydrogen. In the SFR, the steam generator is the place with the possibility of the occurrence of sodium-water reaction. The steam generator can be deteriorated by exchanger tube ruptures, accompany with pressurised water leakage into the sodium side. In consequence, the research topic for sodium-water reaction is mainly in the steam generator.

The evaluation of sodium-water reaction effect requires a good understanding of the leakage initiation and the evolution of the leakage size. Tube failure or rupture starts with small leaks of pressurised water, which can evolve into large leaks by self-wastage before being detected. The corrosive products and high temperature induced by sodium-water reaction can propagate to adjacent tubes, resulting in adjacent tube failures. It is essential to monitor the propagation of tube failures and to take measures to mitigate the propagation [1].

Therefore, it raises the necessity of understanding the sodium-water chemical reaction process to ensure a safety operation. A good understanding of the reaction process can also improve the detection and mitigation systems. Investigation on reactions by experiments is limited by the opaque property of liquid sodium and the high cost, whereas numerical methods are turned out to be effective and economical.

1.2 Observation in Experimental Research

Concerning physical properties of sodium-water reaction, a few experimental research have been presented in Ref. [2]. The mostly important concern in the experiments is to estimate the maximum temperature and temperature distribution. As introduced in the mentioned paper, the maximum temperature depends on the water leakage rate. For example, when the water leakage rate is smaller than 4.5 kg/s, the maximum temperature is measured from 1100 to 1200 ^{o}C. When the water leakage rate is in the range from 7 to 15 kg/s, a maximum temperature range from 1140 to 1250 ^{o}C was measured. Another experiment in Ref. [3] also claims an observation of the transient maximum temperature from 1149 to 1371 ^{o}C. Those experimental data on the maximum temperature are very close to each other, which indicates a certain mechanism dominates the maximum temperature. It is explained in Ref. [2] that the sodium hydroxide evaporation plays an important role on depressing the maximum temperature formation due to the property of its large latent heat. This observation is convenient for judging the numerical results.

Ref. [4] presents an experiment of dropping solid sodium sample into the water. As it illustrated, the hydrogen is generated as soon as the sodium penetrating into the water and appear initially as millimeter size bubbles. But rapidly, those bubbles coalesce together and compose into a gas film surrounding the sodium sample. With the reaction going on, the gas film turns out to be large bubbles detaching from the sodium sample to move upwards to the water surface. The sodium sample move upwards as well due to its lighter density than the water in a very short time measured as 400 ms after the contact with water. It is observed that the thickness of gas layer around sodium sample is almost constant about 1 mm after it reaches to the water surface. Due to the gas generation, the sample is observed to spin quickly and moves randomly on the water surface. It is also noted in the Ref. [4] that the solid sodium changes into the liquid phase shortly after the beginning of reactions. Those phenomena observed from such simple experiments are valuable for the validation of numerical simulations.

1.3 Overview of Numerical Methods for SWR Simulation

A numerical code called SERAPHIM [5] has been developed and widely applied for assessing the sodium-water reaction process. It implements the filed approach to succeed in the simulation of sodium-water reaction known as a multi-phase, multi-component and multi-disciplinary code. This code is validated by many experiments and even a few coefficients used in SERAPHIM are obtained by experimental measurements. Recently, unstructured mesh plotting methodology has been developed for this code for the sake of achieving more accurate local investigation.

In SERAPHIM, two types of SWR mechanism depending on the sodium phase have been proposed, namely surface reaction and gas-phase reaction. The surface reaction represents the reaction takes place on between water vapor and liquid sodium, which is assumed as a water vapor diffusion-driven process. The surface reaction takes place in the early stage while the gas-phase reaction occurs at a later stage when chemical energy is sufficient to vaporize liquid sodium. This sophisticated method has the limitation on consuming considerable computational cost.

There is also a well developed code called LEAP-III, which is mainly used for further analysis on the prediction of occurrence of overheating tubes [6]. The code is characterised in implementing many empirical equations. It is advantageous in conducting the calculation on the temperature distribution in a faster speed than SERAPHIM. However, only temperature isolines can be calculated which neglects some local information easily.

Recently, a few new numerical models are developed by researchers to simulate the Sodium-water reaction using field approaches. In Ref. [7], a diffuse interface model in temperature and pressure equilibrium is used to simulate the reaction between sodium and liquid water through a gas file. The author considers both the surface reaction and gas-phase reaction same as the models developed in SERAPHIM. It is claimed that even the explosion can be qualitatively reproduced by the proposed model. For the validation part, the author computes the maximum temperature of the flame which is between 1600 K and 1800 K. Compared to the measurement in SOGRATE experiments [8] as 1670 K, the computed maximum temperature in Ref. [7] is consistent to the experimental data. The measured temperature of 1670 K is very close to the boiling point of sodium hydroxide, which indicates the same fact concluded in Ref. [5] that sodium hydroxide plays an important role on limiting the maximum temperature by its evaporation.

In Ref. [4], the proposed model considers the sodium evaporation as the action to trigger the sodium-water reaction, which differs from the above mentioned methods. The author mentioned that the diffusivity of sodium is about 500 times larger than that of water. Therefore, in this modelling method, water is remained as the background in large excess. Likewise, two reaction models of surface and gas-phase reactions are considered in this work. In the region near the sodium, only surface reaction takes place, while gas-phase reaction occurs from the surface reaction boundary to the interface with water. Evaporation of sodium is also taken

into account as both the initiation and consequence of the chemical reaction. In other word, the evaporation of sodium is modelled to be accompany with the surface reaction rather than considering its temperature exceeding the boiling point.

All the mentioned methods above adopt the field approach for the modelling, which faces the difficulty of interface modelling. In contrast, particle methods on simulating sodium-water reaction have not been developed yet. Particle methods are superior in tracking the fluid surface without the effort of surface reconstruction. Meanwhile, it is rather straightforward to model chemical reactions by the contact of particle interaction.

Among particle methods, the moving particle semi-implicit method (MPS) developed by Koshizuka and Oka was widely used for free-surface fluid flow simulation [9]. In the MPS method, the Navier-Stokes equations are represented and discretised by particle interactions. The original MPS method is advantageous in simulation incompressible free-surface flows but has the limitation on dealing with high-speed and large density ratio multiphase fluid simulations.

Regarding the extension of the original MPS methods in a wide range application, recently many improvement have been done by researchers. Multiphase MPS methods have been proposed by many researchers. The biggest difficulty by implementing the original MPS method in multiphase simulation is the instability caused by large density ratios of different phases. A multiphase moving particle semi-implicit method (MMPS) developed in Ref. [10] presents two schemes to averaging the density for interfacial particles to avoid extremely large acceleration, especially for the phase with lower density. The numerical stability can be obtained even for a large density ratio of 1000 and viscosity ratio of 100. However, this can only be considered as a multi-density and multi-viscosity MPS method because the compressibility for gaseous phase can not be reproduced. Ref. [11] also proposed a multiphase MPS method by implementing a density smoothening scheme for interfacial particles. It claims that the sharpness of spatial density variation can be retained even by applying the density smoothening scheme while enhancing the stability of pressure calculation. Likewise, no compressibility is considered.

There is no chemical reaction model developed in the original MPS method. Chemical reaction models using MPS method can be found in the field of simulating molten corium-concrete interaction. Ref. [12] introduced an application of MPS using an explicit pressure model to enhance the computational speed. However, only heat transfer and phase change models are proposed without considering any reaction energy and the transportation of species. Concerning the sodium-water reaction with multiphase, multi-density, multi-component and multi-disciplinary characteristics, the original MPS method needs a considerable development to have the feasibility of simulating the sodium-water reaction.

1.4 Motivation and Objectives

The experimental research on investigating the sodium-water reaction is constrained in many aspects, such as limited resources and difficulty in measurement. It is advantageous to utilise numerical methods for the investigation. Field methods have the benefits of considering compressibility for multiphase issues but the difficulty of interface tracking and computational cost can not be neglected. Instead, particle methods are more adequate for chemical reaction modelling. The interfacial particles represent the interface directly without any effort for the interface construction. It is also straightforward to be able to modelling chemical reactions triggering by particle contact. It can also provide an alternative solution on this study to compare to field methods.

The purpose of this research is to develop a multi-disciplinary sodium-water chemical reaction model on the basis of MPS method. As mentioned, the current MPS methods have not been used for a sophisticated chemical reaction modelling which takes into account the modelling of reaction energy, multiple species transportation, phase change and heat transfer among multi-component particles. This research can extend the applicability of particles method not only in thermal-dynamics field but also in chemical reaction field. The sodium-water chemical reaction model should be applicable or adaptable to other chemical reactions.

The whole work requires step-by-step improvement and development. Both liquid sodium and water vapor are discretized into particles. The pressurized water leaked from ruptured tubes in the steam generator is firstly depressurized and evaporated into water vapor with extremely large ejection velocity, which poses the difficulty to the original MPS method dedicated for incompressible fluid flow simulations. To ensure a stable calculation, particularly without unphysical pressure solutions, it is necessary to enhance the pressure stability for water vapor particles. It has been achieved in this work by applying a new kernel function, modifying pressure Poisson equation and partially allowing negative pressure values. Two characteristic sodium-water chemical reaction models, namely surface reaction model and gas-phase reaction model, are essential models to be developed in accordance with particle methods. Surface reaction model accounts for the reaction between water vapor and liquid sodium, which can be under the assumption that the reaction rate is infinitely fast on the interface of water vapor and liquid sodium. The gas-phase reaction model stands for the reaction taken place between water vapor and sodium vapor, which incorporates the rate equation for determining the reactivity. Additionally, heat conduction and mass diffusion among particles with multiple species are required to be modelled taking into consideration of mass and energy conservation.

The MPS method with improvements for multi-density flow is explained in Chapter2. Chapter 3 illustrates the details on modelling chemical reactions by considering many physical mechanisms. The verification of this research has been conducted by means of investigating the mass and energy conservation as shown in Chapter 4. Moreover, the reactant and products concentration and distribution are analysed to get reasonable results based on the sodium-

water reaction characteristics. Investigation has also been conducted on the transient and time-averaged temperature distribution to analyse the propagation features. The validation of this work is to compare the simulation with tube bundles to the SERAPHIM results in Chapter 5. The simulation results have shown a good consistency to SERAPHIM ones, which proves the applicability of this research work on the sodium-water chemical reaction. Finally, conclusions are summarised in Chapter 6.

2 Particle Methods for Multi-phase and Multi-component Flow

The moving particle semi-implicit method (MPS) was originally developed by Koshizuka and Oka, to simulate incompressible free-surface flows [9]. In the MPS method, the fluid is discretized into discrete particles with specific physical properties. Particles move and interact with adjacent ones under the guidance of governing equations. Physical quantities and their derivatives are determined by the total contribution from the neighboring particles. It indicates the approach of discretization for gradient and Laplacian operators in the governing equations is essential for the accuracy of numerical calculations in MPS.

Compared to numerical methods with grid systems, particle methods are superior in tracking the fluid surface without the effort for surface reconstruction. It is because that in the Lagrangian frame, the sharp change of the color function indicating particles with different phases are available and directly represents the interface. Particularly in multiphase flows, the front tracking is of high interest for detecting the interface as many phenomena such as the phase change and chemical reactions are prone to occur at the interface. Therefore, the accuracy of surface particles movement is important for representing the surface deformation. Achieving and maintaining the correct interface in the simulation can extend the functionality of particle methods in other disciplinary fields.

However, the original MPS method suffers from many defects such as the instability of pressure calculation and the absence of a surface tension model [13]. Due to the oscillation of pressure solution, particle motions are not sufficiently credible and surface particles are prone to be disordered to deteriorate the shape of the interface.

In the present study, a few methods are adopted for stabilizing pressure calculation and constructing the surface tension force for multiphase flows, by optimizing the collision model with an optimal collision coefficient, investigating a new weight function with finite values even when particles coincide, introducing another source term in the Laplacian model for guaranteeing the incompressibility [22], modifying the original gradient model with a corrective matrix [24] and implementing a contoured continuum surface tension model [16] with a proposed curvature calculation method. Numerical tests on the modified methods are

performed to judge their influence on stabilizing pressure calculation and the accuracy of curvature calculation of the interface. As proved by the simulation results, the pressure calculation is improved with high stability and smoothness in terms of the temporal evolution and the spatial distribution. By performing a simulation on a bubble rising model, it is observed that the accuracy of curvature calculation of the interface can be ensured.

2.1 MPS Methods

The governing equations for incompressible flows are the continuity and Navier-Stokes equations, given in the Lagrangian frame as follows:

$$\frac{\mathrm{D}\rho}{\mathrm{D}t} = -\rho\nabla\cdot\mathbf{u} = 0 \tag{2.1}$$

and

$$\frac{\mathrm{D}\mathbf{u}}{\mathrm{D}t} = -\frac{1}{\rho}\nabla P + \frac{1}{\rho}\nabla\cdot\left(\mu\nabla\mathbf{u}\right) + \mathbf{f} \tag{2.2}$$

where ρ is the density, $\mathbf{u}$ is the velocity, μ is the dynamic viscosity. The right side of Eq. (2.2) consists of pressure gradient, viscosity, and external-force terms. To be explicit, the external-force term is composed of the gravity, surface tension force and inter-particle collision. All terms in the governing equations expressed by differential operators should be discretized by the particle interaction scheme [9].

The concept of the particle interaction in MPS method is to use a kernel function to weigh the contribution of physical properties from adjacent particles. The kernel function employed in the original MPS method is as follows:

$$\omega_1(r, r_e) = \begin{cases} \frac{r_e}{r} - 1 & (0 \le r \le r_e) \\ 0 & (r_e < r) \end{cases} \tag{2.3}$$

where r is the distance between two particles and r_e represents the effective radius of particle interactions. The kernel function ω_1 approaches to the infinity as $r = 0$. A second kernel function with a finite value at $r = 0$ is proposed as shown in Eq. (2.4). The comparison between two kernels functions is presented in later numerical examples.

$$\omega_2(r, r_e) = \begin{cases} \left(1 - \frac{r_e}{r}\right)^3 \left(1 + \frac{r_e}{r}\right)^3 & (0 \le r \le r_e) \\ 0 & (r_e < r) \end{cases} \tag{2.4}$$

The particle number density (PND) is defined by the following equation:

$$n_i = \sum_{j \neq i} \omega\left(\left|\mathbf{r_j} - \mathbf{r_i}\right|, r_e\right) \tag{2.5}$$

PND is proportional to the fluid density and considered as a constant value n_0 based on the initial particle arrangement for satisfying the condition of incompressibility.

As for discretization methods of differential operators, a gradient vector is transformed by:

$$\left\langle \nabla \phi_i \right\rangle = \frac{d}{n_0} \sum_{j \neq i} \frac{\phi_j - \hat{\phi}_i}{\left|\mathbf{r_j} - \mathbf{r_i}\right|^2} \left(\mathbf{r_j} - \mathbf{r_i}\right) \omega\left(\left|\mathbf{r_j} - \mathbf{r_i}\right|, r_e\right) \tag{2.6}$$

where ϕ_j is a scalar quantity possessing by particle j, $\hat{\phi}_i$ is the minimum value in the effective radius of particle i, d is the number of dimensions.

The Laplacian operator can be considered as the diffusion process and represented by:

$$\left\langle \nabla^2 \phi_i \right\rangle = \frac{2d}{n_0 \lambda} \sum_{j \neq i} \left(\phi_j - \phi_i\right) \omega\left(\left|\mathbf{r_j} - \mathbf{r_i}\right|, r_e\right) \tag{2.7}$$

where λ is defined as

$$\lambda = \frac{\sum_{j \neq i} \omega\left(\left|\mathbf{r_j} - \mathbf{r_i}\right|, r_e\right) \left|\mathbf{r_j} - \mathbf{r_i}\right|^2}{\sum_{j \neq i} \omega\left(\left|\mathbf{r_j} - \mathbf{r_i}\right|, r_e\right)} \tag{2.8}$$

The original Laplacian model is conservative since the quantity of ϕ is interchanged by two particles, while the gradient model is non-conservative in the original pressure solver.

2.2 Pressure Solver

MPS adopts a two-step semi-implicit algorithm by separating the momentum governing equation. In the first step, temporary velocity is explicitly calculated by considering the viscosity and external-force term. After updating locations of all particles by enforcing the movement with the temporary velocity, the temporary particle number density n^* can be obtained. In the second step, for the sake of guaranteeing the incompressibility, the deviation of n^* from the initial value n_0, is compensated by the influence of the pressure distribution, which can be derived as the pressure poison equation (PPE):

$$\left\langle \nabla^2 P \right\rangle_i^{k+1} = -\frac{\rho_0}{\Delta t^2} \frac{n^* - n_0}{n_0} \tag{2.9}$$

The PPE equation can be modified by adopting a mixed source term on the right side, which was proposed by Tanaka and Masunaga [22]:

$$\left\langle \nabla^2 P \right\rangle_i^{k+1} = (1-\gamma)\frac{\rho_0}{\Delta t}\nabla\cdot\mathbf{u}^* - \gamma\frac{\rho_0}{\Delta t^2}\frac{n^*-n_0}{n_0} \tag{2.10}$$

where γ is a blending parameter from 0.01 to 0.05. The extra term on the right side of Eq. (2.10) is the divergence of temporary velocity, which contributes to smoothing and stabilizing pressure calculation but suffers from the accumulated error as time grows [21]. The original term without accumulating error has the disadvantages of inducing exaggerated pressure oscillation. The combination of both terms is therefore utilised in PPE.

After obtaining the pressure distribution by solving PPE, the calculation of the corrected velocity from the pressure gradient model is also essential for guaranteeing the condition of incompressibility and the stabilization of particle motions in the next step. The original pressure gradient model can be obtained by implementing the discretization method of Eq. 2.6 as follows:

$$\langle \nabla P \rangle_i = \frac{d}{n_0}\sum_{j\neq i}\frac{P_j-\hat{P}_i}{\left|\mathbf{r_j}-\mathbf{r_i}\right|^2}\left(\mathbf{r_j}-\mathbf{r_i}\right)\omega\left(\left|\mathbf{r_j}-\mathbf{r_i}\right|, r_e\right) \tag{2.11}$$

where $\hat{P}_i$ is the minimum pressure in the adjacent region of particle i.

A corrected gradient model developped by Khayyer and Gotoh [24] is adopted for minimizing particle disorders and perturbations in particle motions. Based on Tylor series expansion of the pressure term, it can be derived as follows:

$$\langle \nabla P \rangle_i = \frac{d}{n_0}\sum_{j\neq i}\frac{P_j-\hat{P}_i}{\left|\mathbf{r_j}-\mathbf{r_i}\right|^2}\left(\mathbf{r_j}-\mathbf{r_i}\right)\mathbf{C_{ij}}\omega\left(\left|\mathbf{r_j}-\mathbf{r_i}\right|, r_e\right) \tag{2.12}$$

where $\mathbf{C_{ij}}$ is the corrective matrix derived as below [23]:

$$\mathbf{C_{ij}} = \begin{bmatrix} \Sigma\frac{\omega\left(\left|\mathbf{r_j}-\mathbf{r_i}\right|,r_e\right)x_{ij}^2}{\left|\mathbf{r_j}-\mathbf{r_i}\right|^2 n_i^*} & \Sigma\frac{\omega\left(\left|\mathbf{r_j}-\mathbf{r_i}\right|,r_e\right)x_{ij}y_{ij}}{\left|\mathbf{r_j}-\mathbf{r_i}\right|^2 n_i^*} \\ \Sigma\frac{\omega\left(\left|\mathbf{r_j}-\mathbf{r_i}\right|,r_e\right)x_{ij}y_{ij}}{\left|\mathbf{r_j}-\mathbf{r_i}\right|^2 n_i^*} & \Sigma\frac{\omega\left(\left|\mathbf{r_j}-\mathbf{r_i}\right|,r_e\right)y_{ij}^2}{\left|\mathbf{r_j}-\mathbf{r_i}\right|^2 n_i^*} \end{bmatrix}^{-1} \tag{2.13}$$

For single phase flow, the particle number density gets decreasing when particles move toward the free surface. Thus, the criteria for detecting the free surface is to justify the ratio of temporary local density to the initial value as shown in Eq. 2.14.

$$n^* < \beta n_0 \tag{2.14}$$

where β is a parameter below 1.0 and $\beta = 0.97$ is suggested in [9].

The pressure at the surface boundary is set as the atmosphere level to satisfy the dynamic free surface condition. However, the above criteria may misjudge inner fluid particles as surface particles given that a local dilution or void is present during the simulation, which causes large fluctuation of the pressure solution around the misjudged particle.

To overcome the misjudgment of surface particles, another criteria implemented in this study is to check the number of neighboring particles:

$$N_i < \eta N_0 \tag{2.15}$$

where N_i is the number of adjacent particles around particle i, N^0 is the maximum number of adjacent particle in terms of the initial particle arrangement, and η = 0.83 is used. Both Eqn. 2.14 and Eqn. 2.15 are utilized for identifying the free surface particles.

In the original MPS method, the collision model was not necessary since the repulsive force originates from the local pressure difference when particles get closer to each other. However, since the relative pressure field is set to zero on the free surface, no repulsive force exists for preventing incoming particles coinciding with the ones on the free surface. It may further raises the local particle number density given a closer contact. Consequently, the neighboring surface particles may be regarded as the inner particles and produce excessive pressure to fail the stability of the pressure field [21]. Therefore, a two-body collision model is developed for the sake of maintaining a good stabilization.

The recoiling velocity of the colliding particles can be calculated by the following equation:

$$\mathbf{v_i} = \mathbf{u_i} - \frac{2\rho_j}{\rho_i + \rho_j} \frac{\left(\mathbf{u_i} - \mathbf{u_j}\right) \cdot \left(\mathbf{r_i} - \mathbf{r_j}\right)}{\left|\mathbf{r_i} - \mathbf{r_j}\right|^2} \left(\mathbf{r_i} - \mathbf{r_j}\right) \tag{2.16}$$

where $\mathbf{v_i}$ is the recoiling velocity of particle i with the incoming velocity $\mathbf{u_i}$, m_i and m_j are the mass of two colliding particles respectively.

As for the criteria of initiating the collision model, the distance between two particles l_{ij} should satisfy the below condition:

$$l_{ij} < \alpha l^0 \tag{2.17}$$

where l^0 is the constant distributed distance between particles in the initial uniform arrangement, and α, with the original value of 0.5, is the parameter for determining whether the collision is initiated. As shown in later sections, a larger α with a value of 0.9 contributes to less fluctuation of the pressure field.

In this section, five varied modifications on the original MPS method are tested. To investigate the contribution of each modification to the stabilization of pressure calculations, a

Table 2.1 – Illustration of simulated cases with the modifications applied. Case 0 is the original MPS method.

Case	ω_1, ω_2	α	η	β, γ	$\mathbf{C_{ij}}$
0	Eqn. (2.3)	0.5	Eqn. (2.14)	Eqn. (2.29)	Eqn. (2.11)
1	Eqn. (2.3)	0.5	Eqn. (2.14)	Eqn. (2.29)	Eqn. (2.11)
2	Eqn. (2.3)	0.9	Eqn. (2.14)	Eqn. (2.29)	Eqn. (2.11)
3	Eqn. (2.3)	0.9	Eqn. (2.14,2.15)	Eqn. (2.29)	Eqn. (2.11)
4	Eqn. (2.3)	0.9	Eqn. (2.14,2.15)	Eqn. (2.10)	Eqn. (2.11)
5	Eqn. (2.3)	0.9	Eqn. (2.14,2.15)	Eqn. (2.10)	Eqn. (2.12)
6	Eqn. (2.3)	0.9	Eqn. (2.14,2.15)	Eqn. (2.29)	Eqn. (2.12)

few specific cases with various combinations are illustrated in Table 2.1 and simulated for comparison.

The set up for calculating the hydrostatic pressure is presented with the dimensions depicted in Fig. 2.1. The water level height is 0.5 m, corresponding to the theoretical pressure of 5000 Pa at the bottom wall layer. For comparison between different cases, the pressure of the particle situated at the bottom center of the wall layer is extracted and plotted with respect to the simulation time in Fig. 2.2.

Case 0 referring the original MPS method shows the increasing oscillatory pressure behavior as concerned. Case 1 adopting a finite weight function has the tendency of postponing the occurrence of the pressure oscillation but it escalates the instability as time grows. The pressure oscillation in the previous two cases may arise out of the fact that the velocity of particles in the tank grow largely after 1 s because the pressure gradient model in Eq. (2.6) does not satisfy the conservation of momentum. Case 2 by decreasing the tolerance of the collision distance, first facilitates the frequency of inter-particle inelastic collision with energy dissipation. On the other hand, the larger collision coefficient prevents the longer penetration between particles and the extremely large pressure difference from happening.

Case 4 and Case 5 both implement the velocity divergence as the prominent source term in the PPE, where the fluid velocity has been already mitigated by the collision model. Case 4 is more fluctuated than Case 5, which applies the corrective matrix method. Due to the very small coefficient γ of the particle deviation term in Eq. (2.29), particles in both cases have a tendency of aggregating and resulting in a compact distribution compared to the initial arrangement. In consequence, on one hand the water level is slightly shrunk and the bottom pressure is smaller than the other cases. On the other hand, the velocity divergence is not applicable for guaranteeing the compressibility. Therefore, the model with mixed source terms should be more suitable for simulating the violent flows with comparable velocities.

Case 3 and Case 6 have a good consistence with the theoretical pressure of 5000 Pa and present very stable pressure evolution. As shown by Case 2, the collision model has the dominant

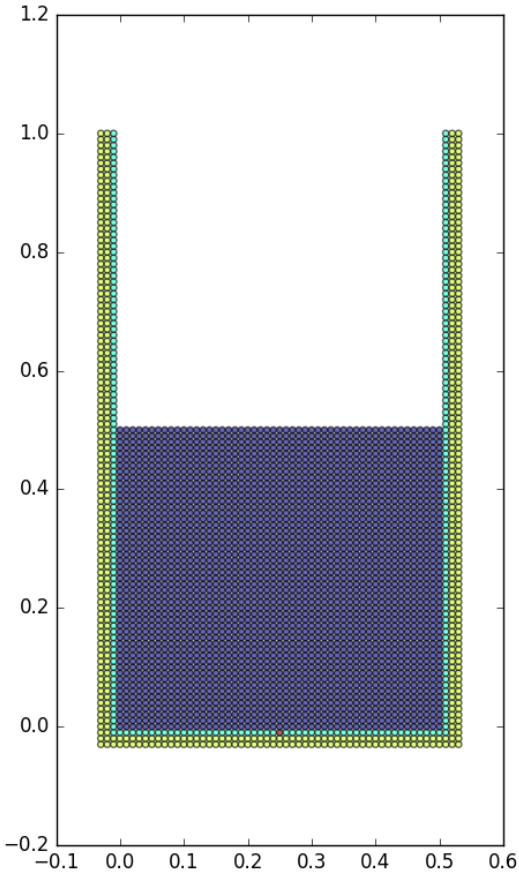

Figure 2.1 – Schematic view of the hydrostatic pressure model

influence on improving the pressure stability. The newly added criteria for defining the free-surface particles and the corrective matrix model does not reveal promotive effect on reducing the pressure fluctuation in the simulation.

As a difference from the previous model, the dam break simulation is representative for the violent free-surface flow. The set up of the dam break model used in the reference [21] is adopted for investigating the pressure stability with respect to different cases. In the dam break model, the width of the water tank is 1.6 m and the particle on the right wall layer situated at the height of 0.02 m is selected as the position detecting the pressure evolution when the water column starts to collapse and splash the tank wall.

Fig. 2.4 is plotted with the pressure evolution with respect to the time for different cases. As Case 3 produces the almost same result as the Case 2 like the similarity observed in Fig. 2.2, the pressure evolution in Case 3 is not plotted. In Fig. 2.7, the pressure profile of the dam break

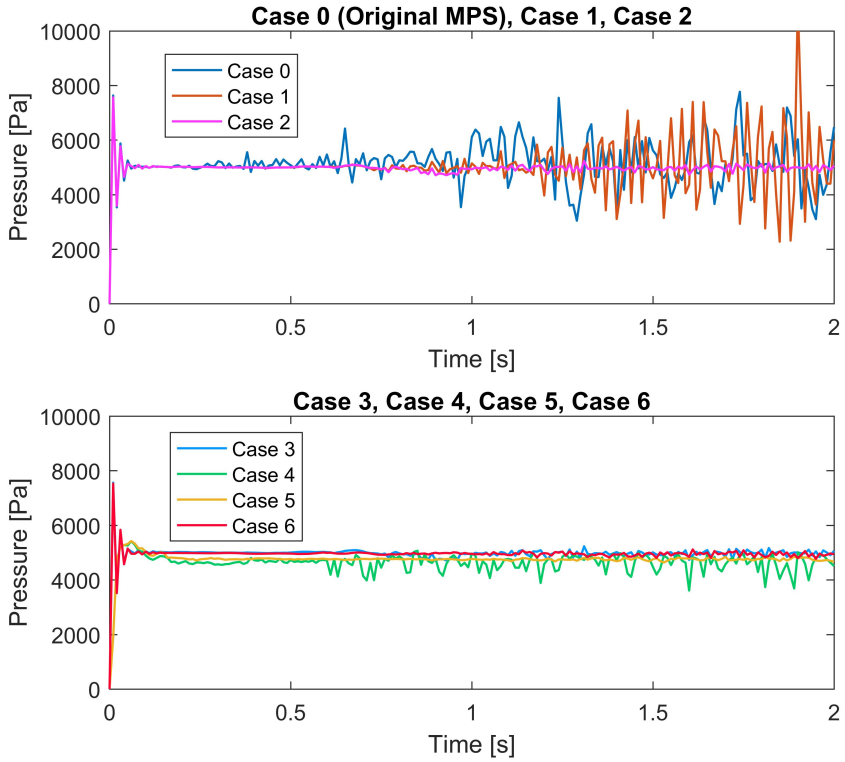

Figure 2.2 – Pressure evolution at the bottom center of the wall layer

at t = 1.3 *s* for each concerned case is illustrated.

From Fig. 2.4, it can be observed that Case 2 with the enlarged collision coefficient α dominates the effort to eliminate the pressure oscillation along the time evolution. Meanwhile in terms of the pressure profile, the pressure field get smoothed spatially compared to the first two cases with a collision coefficient of 0.5.

As for Case 4-6, Case 6 without including the source term of velocity divergence presents more fluctuation on the pressure solution compared to Case 4 and Case 5. It indicates that the velocity divergence source term can be beneficial for suppressing the instability of the pressure field in the violent fluid flow. The difference between Case 4 and Case 5 is whether to upgrade the gradient model with the corrective matrix for higher accuracy. The smoothness of pressure profiles for both cases are superior than other cases while the temporary pressure evolution in Case 4 is inferior to that in Case 5.

2.3 Surface Tension Force

In the classical continuum surface force model [17], a transition region between difference phases is considered as the interface where surface tension forces are applied. The surface

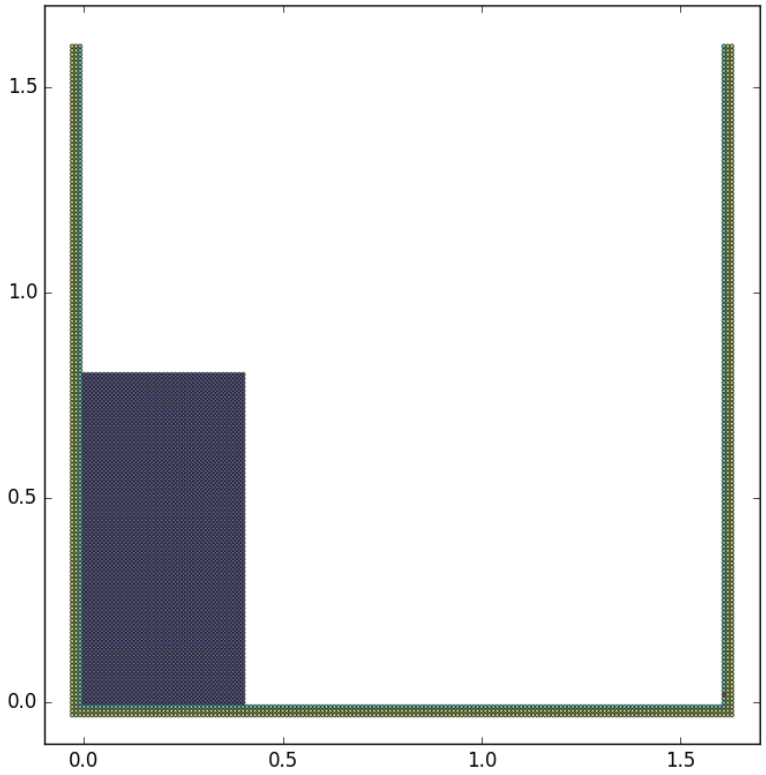

Figure 2.3 – Schematic view of the dam break model

tension force in the external-force term can be expressed as follows:

$$\mathbf{f_s} = \frac{\sigma \cdot \kappa}{\rho_i} \frac{\nabla C}{|\nabla C|} \tag{2.18}$$

where f_s is the volumetric surface tension force for each particle, σ is the surface tension coefficient, κ is the curvature, C is the phase indicator namely the color function and $\frac{\nabla C}{|\nabla C|}$ refers to the normal direction of the interface, which can be calculated via Eqn. (2.6).

$$C_i = \begin{cases} 0 & \text{(if i is in the specific phase)} \\ 1 & \text{(if i is in the other phase)} \end{cases} \tag{2.19}$$

A contoured continuum surface force model (CCSF) was developed by Duan [16]. The scheme of CCSF is to regard the contour curve of color magnitudes as the interface boundary. By calculating the curvature of the local contour passing through the interface particles, the local curvature of the interface is obtained. The Gaussian kernel function adopted for mollifying the color function is essential in terms of the consistency of the resulting contour curve and

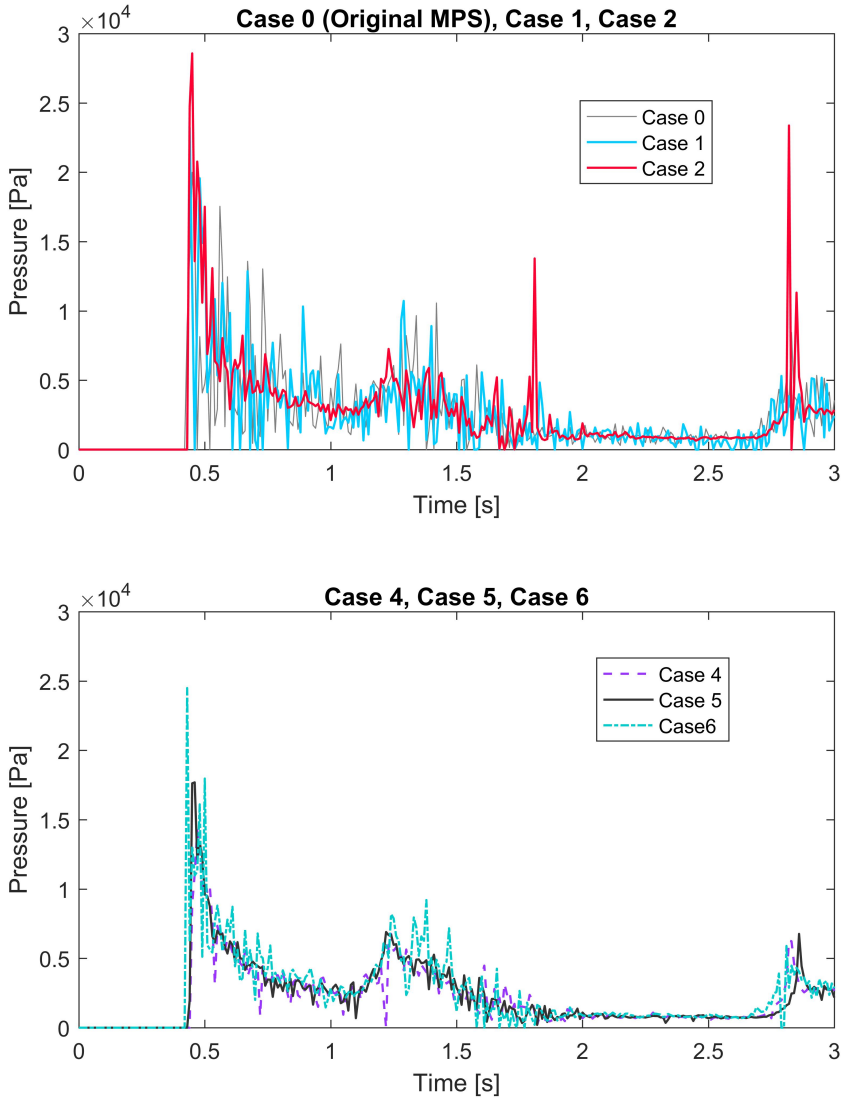

Figure 2.4 – Pressure evolution at the right bottom corner of the wall

the exact interface. If the contour curve of the smoothed color function deviates from the interface, the reproduced interface curvature is inaccurate as well.

The Gaussian kernel for smoothing the discontinuous color function C_i is selected as follows:

$$G(r, r_s) = \begin{cases} e^{-6r^2/r_s^2} & (0 \le r \le r_s) \\ 0 & (r_s < r) \end{cases} \tag{2.20}$$

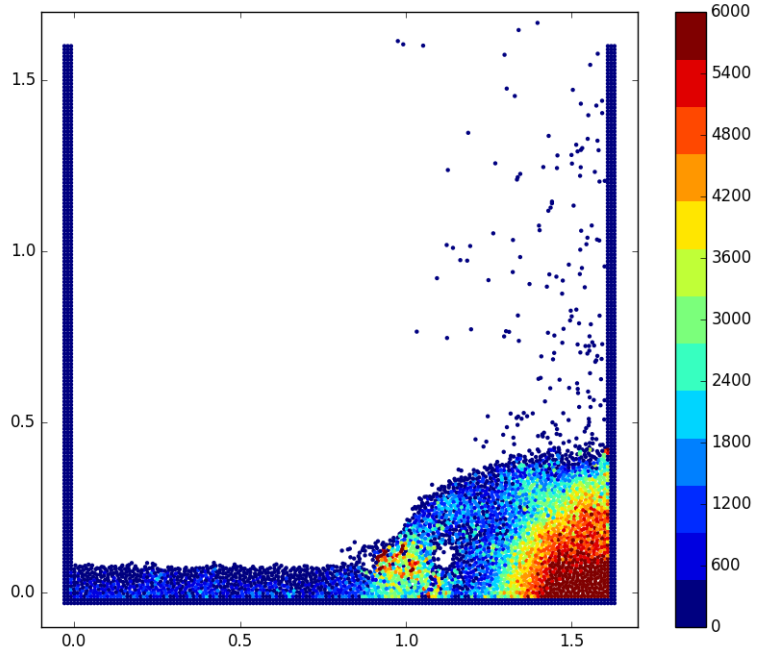

(a) Case 0

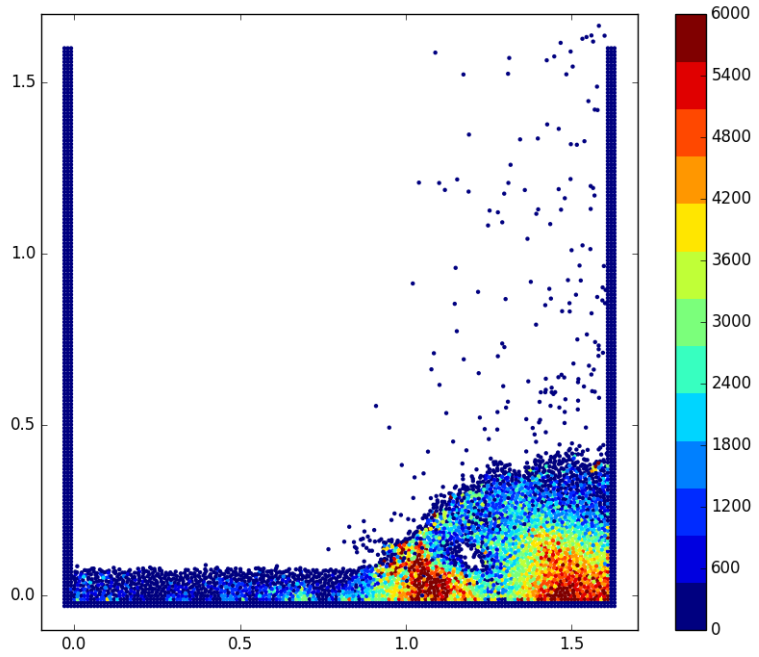

(b) Case 1

Figure 2.5 – Pressure profiles of Case 0 and Case 1 at t = 1.3s

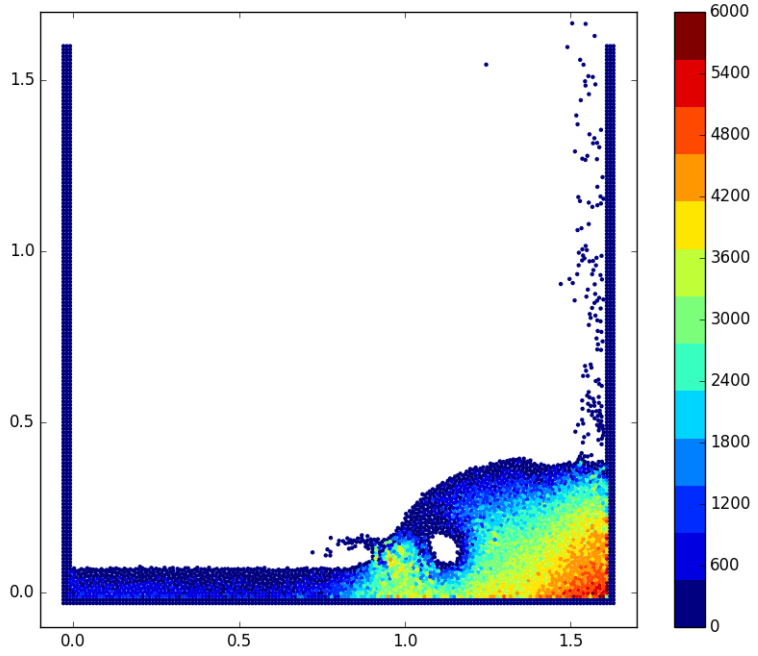

(a) Case 2

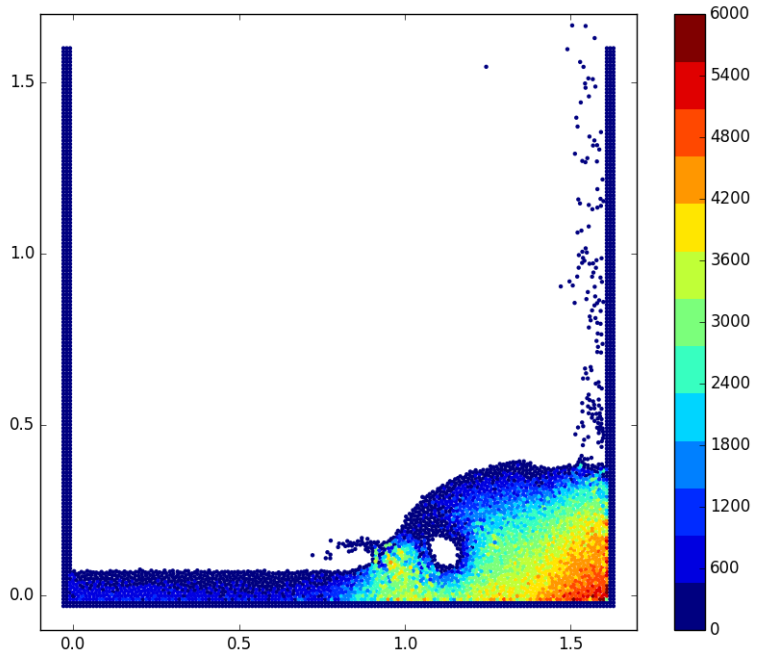

(b) Case 3

Figure 2.6 – Pressure profiles of Case 2 and Case 3 at t = 1.3s

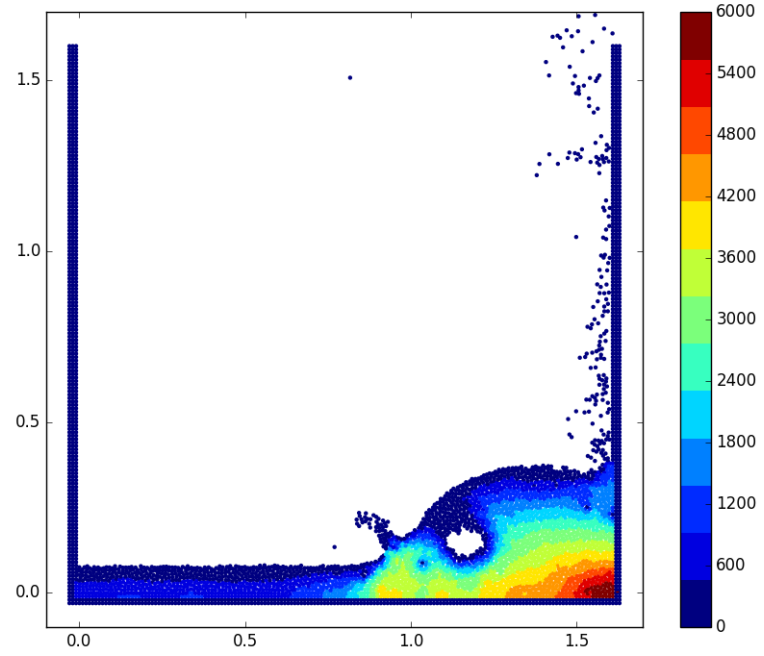

(a) Case 4

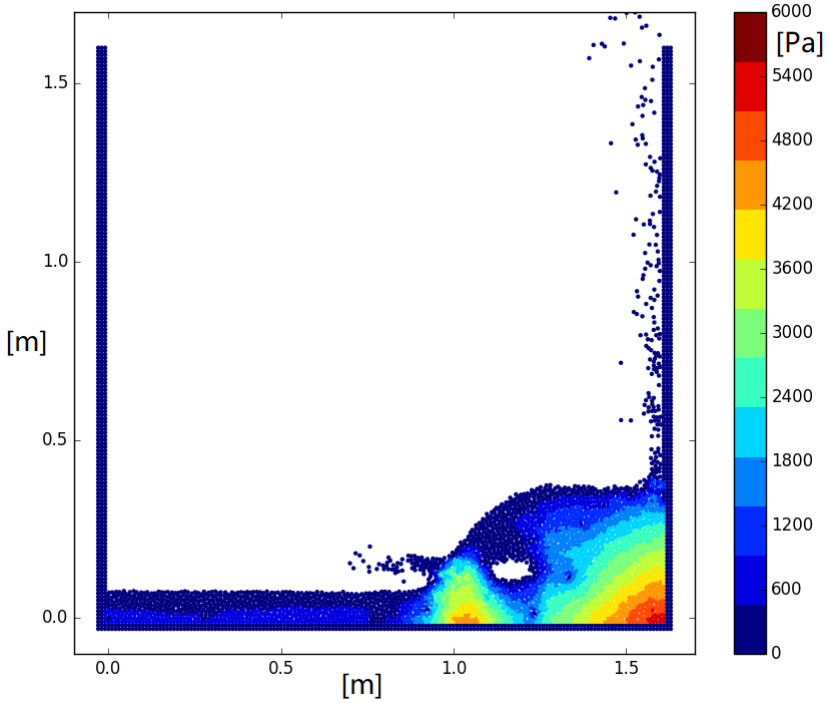

(b) Case 5

Figure 2.7 – Pressure profiles of Case 4 and Case 5at t = 1.3s

$$f_i = \frac{\sum_j C_j G\left(\left|\mathbf{r_j} - \mathbf{r_i}\right|, r_s\right)}{\sum_j G\left(\left|\mathbf{r_j} - \mathbf{r_i}\right|, r_s\right)} \tag{2.21}$$

where $G(r, r_s)$ is the Gaussian kernel for smoothing the color function, r_s is effective radius for smoothing and f_i is the mollified color value of the particle i. r_s is the most important parameter for affecting the accuracy and efficiency of the CCSF model. As r_s gets larger, it can lead to better coincidence of the contour curve of color magnitudes and the interface for local particles with small curvature values, while it may also eliminate the sharp angles of the interface and neglect detailed information of the sharp curvature.

The curvature can be derived based on the implicit smoothed color function [18]:

$$\kappa_i = \frac{2 f_{x,i} f_{y,i} f_{xy,i} - f_{x,i}^2 f_{yy,i} - f_{y,i}^2 f_{xx,i}}{\left(f_{x,i}^2 + f_{y,i}^2\right)^{3/2}} \tag{2.22}$$

where $f_{x,i}$ is the first derivative value with regard to x of the smoothed color function f of the particle i, $f_{xx,i}$ is second derivative value with regard to x of f_i and so on.

The original CCSF model used a cumbersome analytical method for calculating the above derivatives, which is difficult to reproduce the accuracy they achieved. Instead, the gradient model presented in Eqn. (2.6) is utilized for the calculation of the first and second derivatives sequentially.

$$f_{x,i} = \frac{d}{n_0} \sum_{j \neq i} \frac{f_j - f_i}{\left|\mathbf{r_j} - \mathbf{r_i}\right|^2} \left(x_j - x_i\right) \omega\left(\left|\mathbf{r_j} - \mathbf{r_i}\right|, r_s\right) \tag{2.23}$$

$$f_{xx,i} = \frac{d}{n_0} \sum_{j \neq i} \frac{f_{x,j} - f_{x,i}}{\left|\mathbf{r_j} - \mathbf{r_i}\right|^2} \left(x_j - x_i\right) \omega\left(\left|\mathbf{r_j} - \mathbf{r_i}\right|, r_s\right) \tag{2.24}$$

$$f_{xy,i} = \frac{d}{n_0} \sum_{j \neq i} \frac{f_{x,j} - f_{x,i}}{\left|\mathbf{r_j} - \mathbf{r_i}\right|^2} \left(y_j - y_i\right) \omega\left(\left|\mathbf{r_j} - \mathbf{r_i}\right|, r_s\right) \tag{2.25}$$

Likewise, $f_{y,i}$ and $f_{yy,i}$ can also be calculated by applying the discretization method for gradient models.

In this section, a bubble rising model is used for verifying the accuracy and applicability of the proposed surface tension model. The initial configuration of the set up is same as the first

dimensionless case of the benchmark presented in [20]. As a difference from the previous single phase simulation, this case includes two incompressible phases with both density and viscosity ratios as 10. Inside the configuration, a bubble with a diameter of 0.5 unit of the tank width, Re = 35 and Eo = 10 is lifting up due to the buoyancy. Moreover, the smoothing radius for the color function r_s equals to 4.1 r_e.

The simulation is conducted for a period of 3 time units during which the pressure profiles of the model and the curvature values at the bubble interface are recorded and plotted in Fig. 2.8 at t = 0.1, in Fig. 2.9 at t = 1.0 and in Fig. 2.10 at t = 3.0. The multiphase model for the MPS method has not been fully developed yet in this study but the curvature calculation as the most important step in the surface tension model is worth being verified.

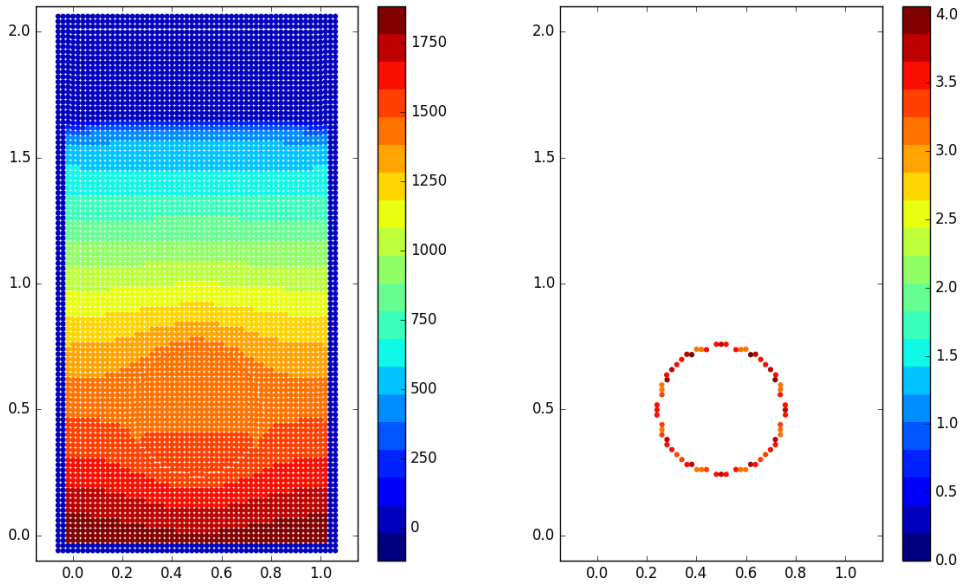

(a) Pressure

(b) Curvature

Figure 2.8 – Pressure profiles and interface curvatures in the bubble rising model at t=0.1

In Fig. 2.8, it can be noticed that at t = 0.1 the pressure inside the bubble is prone to be uniform due to the relatively large density difference between two phases, while the pressure profile outside the bubble is well stratified. On the right sub-figure, the curvature of the interface calculated to be 3.0 to 4.0 is consistent with the analytic value. At t = 1.0, the bottom of the bubble becomes flat due to the deformation, which indicates a curvature value of 0 as presented in the figure. The curvature will continue to evolve to negative values as the local interface turns into a concave shape. The local curvature value is relatively precise because the smoothing radius is comparably small compared to the whole bubble configuration. It results in a good reflection of the local deformation but may also induce large deviation if

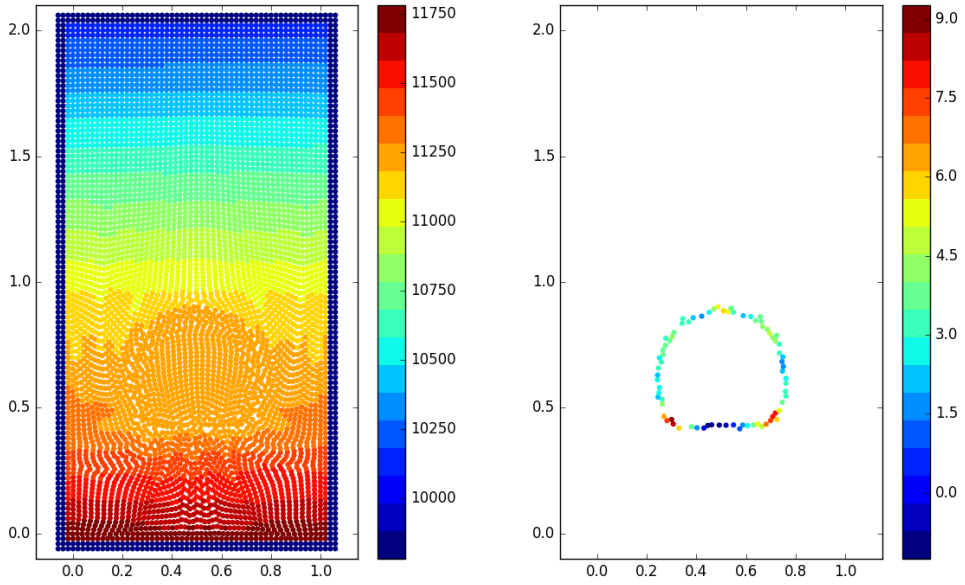

(a) Pressure (b) Curvature

Figure 2.9 – Pressure profiles and interface curvatures in the bubble rising model at t=1.0

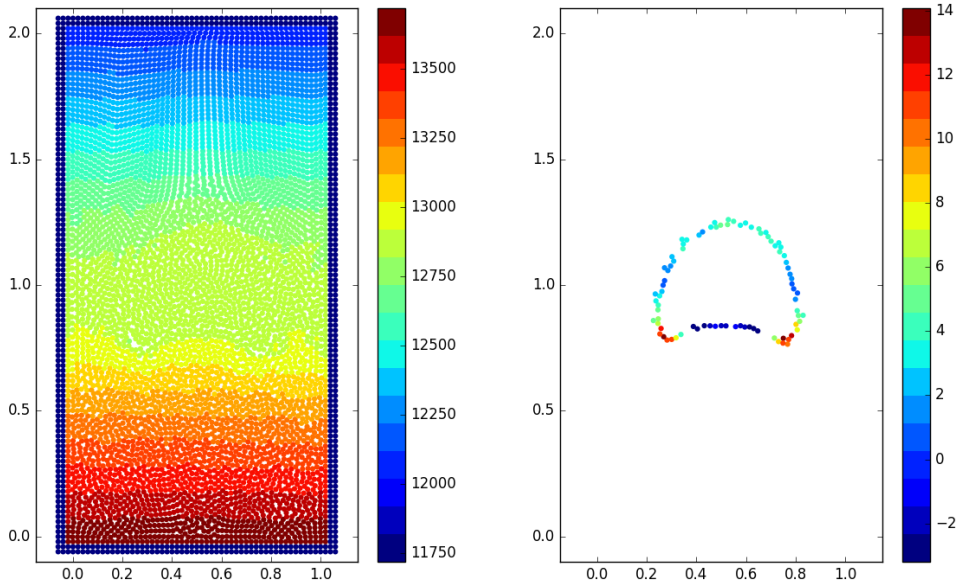

(a) Pressure (b) Curvature

Figure 2.10 – Pressure profiles and interface curvatures in the bubble rising model at t=3.0

many particles of the bubble phase gather locally. On the contrary, utilizing a larger smoothing radius can mollify the curvature results but has a defect of not being representative for sharp curvatures.

2.4 Variable Density Flow

In multi-viscosity and multi-density models, the viscosity μ and density ρ are not the same in different phases. To avoid the sharp variation at the phase interface and stabilize the calculation, the force terms in the governing equation are discretized using the harmonic mean value of viscosity and the arithmetic mean value of density respectively and represented as:

$$\left\langle \frac{1}{\rho}\nabla\cdot\left(\mu\nabla\mathbf{u}\right)\right\rangle_i = \frac{2d}{n_0\lambda}\sum_{j\neq i}\left\{\frac{2}{\rho_i+\rho_j}\frac{2\mu_i\mu_j}{\mu_i+\mu_j}\left(\mathbf{u_j}-\mathbf{u_i}\right)\omega(\left\|\mathbf{r_j}-\mathbf{r_i}\right\|)\right\} \tag{2.26}$$

where d is the number of dimensions, n_0 is the constant particle number density (PND), λ is the variance of neighbor particle distance, i refers to the investigated particle, j represent its adjacent particles and ω is a kernel function accounting for contribution from neighboring particles.

The weighting function ω used in the original MPS method is characterized with a magnitude of infinity when neighboring particles move to the same position. For the sake of allowing certain compressibility, the following weighting function is adopted in this research work.

$$\omega(\left\|\mathbf{r_j}-\mathbf{r_i}\right\|) = \begin{cases} \left(1-\frac{R}{\left\|\mathbf{r_j}-\mathbf{r_i}\right\|}\right)^3\left(1+\frac{R}{\left\|\mathbf{r_j}-\mathbf{r_i}\right\|}\right)^3 & (0\leq\left\|\mathbf{r_j}-\mathbf{r_i}\right\|\leq R) \\ 0 & (R<\left\|\mathbf{r_j}-\mathbf{r_i}\right\|) \end{cases} \tag{2.27}$$

where R represents the influential radius of the contribution from adjacent particles. Eq.[3] presents a threshold of the weight which can effectively eliminate the appearance of excessive pressure values when particles are compressed.

The viscosity term and the gravity can be calculated explicitly, whereas the pressure term is solved implicitly. A mixed term of the intermediate velocity divergence is adopted in the multiphase pressure Poisson equation (PPE), as represented in Eqn. (2.29), to mitigate the influence from large variation of PND induced by the aggregation of particles. As a result, the compression ratio can be enlarged in the calculation meanwhile with stabilized pressure solution.

$$\left\langle\nabla\cdot\left(\frac{1}{\rho}\nabla P\right)\right\rangle_i^{k+1} = \left(1-\gamma\right)\frac{1}{\Delta t}\nabla\cdot u^* - \gamma\frac{1}{(\Delta t)^2}\left\{\frac{n^*-n_0}{n_0}\right\} + \alpha\frac{1}{(\Delta t)^2}P_i^{k+1} \tag{2.28}$$

where γ is a relaxation coefficient, u^* is the predicted velocity, n^* is the intermediate PND, and α is an artificial compressibility ratio.

Likewise, the discretization of the left side of Eq.(3) is formulated as follows:

$$\left\langle \nabla \cdot \left(\frac{1}{\rho} \nabla P \right) \right\rangle_i^{k+1} = \frac{2d}{n_0 \lambda} \sum_{j \neq i} \left\{ \frac{2}{\rho_i + \rho_j} \left(P_j^{k+1} - P_i^{k+1} \right) \omega(\left\| \mathbf{r_j} - \mathbf{r_i} \right\|) \right\} \tag{2.29}$$

After obtaining the pressure solution based on Eq.(3) and Eq.(4), the pressure gradient among particles can be calculated as:

$$\left\langle \frac{1}{\rho} \nabla P \right\rangle_i = \frac{d}{n_0} \sum_{j \neq i} \left\{ \frac{2}{\rho_i + \rho_j} \frac{\left(P_j - P_{i,min} \right) \left(\mathbf{r_j} - \mathbf{r_i} \right)}{\left\| \mathbf{r_j} - \mathbf{r_i} \right\|^2} \mathbf{C_i} \omega(\left\| \mathbf{r_j} - \mathbf{r_i} \right\|) \right\} \tag{2.30}$$

where $P_{i,min}$ refers to the minimum pressure among neighboring particles of the reference particle, and C_i is a corrective matrix used for improving the accuracy of pressure gradient calculation.

With the implementation of above methods, a multiphase and multi-density fluid simulation can get enhanced numerical stability. However, it still has the difficulty to achieve numerical stability given models with particles moving at a high speed, unless a smaller time-step is used, which consequently limits the applicability of particle methods in our research. For particles in varied phases with a large density ratio, heavier particles tend to be slower than lighter particles. Particularly, if lighter particles are assigned with a high initial speed, for instance of gas jet into stagnant liquid, the velocity variation in different phases become even larger. Unphysical void space is likely to emerge around the trajectory of gas jet and particles around the void space are in a sparse distribution, which contributes to negative pressure values. However in the original MPS method, particles with negative pressure solutions are assigned to zero pressure. As a result, no pressure gradient exists for these internal particles and it is difficult for them to shrink to eliminate the unphysical void.

One solution to eliminate the unphysical void is to take into consideration of particle expansion, while it seems to be complicated for the current work. Instead, we propose to remain negative pressure solution for particle in the interior of the fluid and to assign zero pressure for particles on the real free-surface region. This method can effectively avoid the existence of unphysical void and enhance the stability of pressure calculation. On the other hand, it supports multiphase simulation cases featured with a large density and speed ratio for varied phase particles.

2.5 Multi-Component Particles

Due to the characteristic of chemical reaction, a number of chemical species have to be considered in the particle method. Differing from the common particle method with single component in each particle, this study implements particles with multiple components.

Inter-particle interaction has to be considered for multi-components in terms of many physical

models. In this case, mass and energy diffusion among neighbouring particles with multi-components raises difficulty on two aspects for the original MPS method. Firstly, the physical properties are definitely to be changed by the variation of types and amount of components. To be specific, the density is not identical after the mass diffusion given the particle volume is fixed. Moreover, the mass diffusivity and heat conductivity will depend on the composition of particles as well. Secondly, physics mechanism to be interpreted by particles methods need to be developed for being applicable to model the interaction of particles with varied composition.

For example, consider modelling particles with two different components A and B. For a binary composition, mass diffusion can take place once the concentration among neighbouring particles is not identical. The gradient of concentration induces the mass flux among particles. It is straightforward to find the diffusivity data for single component and implement it for the mass diffusion model given a single-component case. When dealing with more than one components, the diffusivity of one species among the others will differ in terms of the mole fraction of other species.

In the situation with two gaseous components, a binary diffusion model can be applied for calculating the diffusivity of each species. The equation is formulated as follows:

$$D_{A-B} = \frac{10^{-3} T^{1.75} \left[\frac{1}{M_A} + \frac{1}{M_B}\right]^{1/2}}{P_{abs}[(\sum \nu)_A^{1/3} + (\sum \nu)_B^{1/3}]^2} \tag{2.31}$$

where D_{A-B}, T, P_{abs}, M, $\sum \nu$ are binary gas phase diffusivity of A in B, temperature, absolute pressure in atm, molecular weights and molecular volumes, respectively.

As indicated from the above equation, the diffusivity of A in B is exactly the same as the diffusivity of B in A for a binary diffusion model.

3 Sodium-Water Reaction Models

3.1 Review of Sodium-Water Reactions

The Sodium-water reactions are carried out upon the leaked water vapor contacting with liquid sodium or gaseous sodium. The latter one is observed due to the evaporation of liquid sodium after absorbing excessive reaction heat. Accordingly, two different chemical reaction models are developed in particle methods, which are surface reaction and gas-phase reaction as shown in Fig. 3.1.

The surface reaction model represents the reaction between liquid sodium and water vapor, while the gas-phase reaction model refers to the reaction between sodium vapor and water vapor. Concerning the surface reaction model, it is assumed that water vapor at the interface contacting with liquid sodium particles is completely and instantaneously consumed by the reaction, which results in a concentration gradient inside the gaseous particle. Due to the diffusion and convection of water vapor from the other side to the interface, the surface reaction is triggered.

Surface reaction dominates the early stage of chemical reaction with chemical heat released. Neighbouring liquid sodium particles are heated up to vaporise into sodium vapor and mixes with water vapor. In this case, there is opportunity that water vapor can reacts with sodium vapor, which is the gas-phase reaction process.

The reaction equation is represented in the equation below, in which sodium hydroxide and hydrogen are regarded as main products. Particles are considered to contain multi-components after the reaction. In the reality, there are also many other intermediate products, which are considered in this study.

$$Na(l) + H_2O(g) \rightarrow NaOH(l) + 1/2H_2(g), \Delta H^{298} = -177.46 kJ/mol \tag{3.1}$$

where ΔH^{298} is the standard enthalpy change of formation.

As the Eq. 3.1 shows, it is characterised as an exothermal reaction. With one mole reaction,

the energy of 177.46 kJ will be released given that the reactants and the products are all at the standard temperature of 298 K. This value is not used in the following modelling. Instead, this study proposes to calculate the total enthalpy change for obtaining the reaction energy.

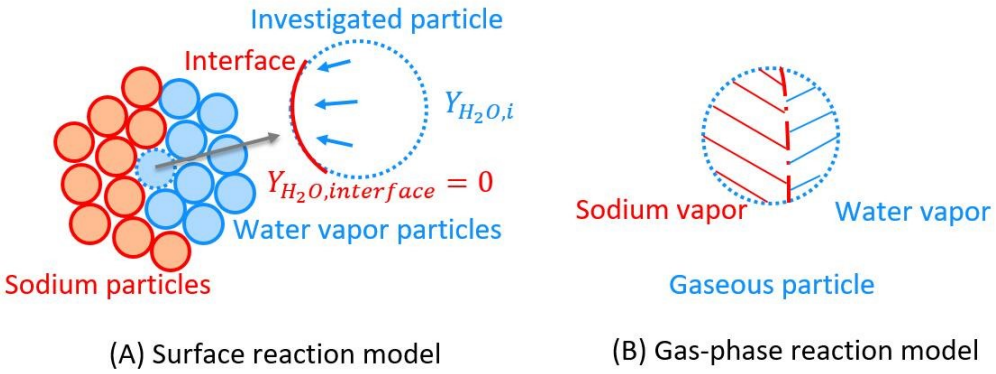

Figure 3.1 – Schematic of surface reaction model and gas-phase reaction model

3.2 Assumptions for Simplification of Modelling

The sodium-water chemical reaction is a complex and multi-disciplinary process which requires sophisticated modelling on each physical mechanism. However, some concerns have not been solved by using particle methods, such as the compressibility of gas phase and non-equilibrium thermal dynamics process. It is of great importance to simplify the physical mechanism and focus on modelling the main characteristics of this reaction process within limited time and computational cost. Here lists the assumptions for simplifying the physical model to make it available and easier for practical modelling and simulation.

List of Assumptions:

1. Multiple components inside the same particle have only one unified temperature.

Explanation: the heat exchange inside the particle is sufficiently frequent and effective which allows different components cooling down or heating up to a unified temperature within one computational step. This assumption raises a criterion for determining the particle size.

2. Evaporation and condensation rates of NaOH are infinitely fast within one computation step.

Explanation: This assumption is necessary for supporting the previous one. If the evaporation and condensation rates are finite during one time-step, some unphysical behaviour will occur. For example, liquid NaOH exists in the particle with a temperature higher than NaOH's boiling point.

3. Mass diffusion of gaseous components among gaseous particles are allowed, while mass

diffusion in liquid particles or between liquid and gas particles are not considered.

Explanation: Liquid sodium particles have the incompressibility and present uniform distribution of sodium concentration. However, gas particles are mainly composed of gaseous components, of which concentration variation among neighbouring particles will occur as a consequence of mass change by chemical reactions and pressure difference.

4. Products are only distributed in gaseous particles and the reaction energy is carried by products.

3.3 Surface Reaction Model

The surface reaction model is developed on the assumption of an instantaneous chemical reaction process. It indicates the surface reaction rate is controlled by the mass flow rate of the water vapor towards the sodium-water interface. The surface reaction rate is modelled as illustrated in the following equation.

$$\Gamma_{sf} = Mo_g S \frac{D_{H_2O}}{l_0} (Y_{H_2O} - Y_{H_2O,interface}) \tag{3.2}$$

where Γ_{sf} is the surface reaction rate, Mo_g is the total molar amount of gaseous speices, S represents the interfacial area density, D_{H_2O} is the effective binary diffusivity, l_0 is the characteristic length and Y_{H_2O} is the volume fraction of water vapor in the reference particle. $Y_{H_2O,interface}$ refers to the volume fraction of water vapor at the interface. According to the assumption of an infinitely fast reaction at the interface, water vapor is supposed to be consumed completely indicating $Y_{H_2O,interface} = 0$.

In fact, the mass flux rate of water vapor is equivalent to the coupled effect of diffusion and advection. However, in the particle methods, the advection process is naturally replaced by the particle movement. Therefore, Eq. 3.2 is represented by the diffusion flux of water vapor induced by concentration gradient. The modelling is adequate only when the particle size is sufficiently small. Otherwise the advection effect may be neglected, which induces an underestimated surface reaction rate.

In Eq. 3.2, the surface reaction rate depends on the characteristic length, which is equal to the particle size in the current model. The variation on the particle size will influence on the magnitude of surface reaction rate. For a sophisticated work, one need to use dimensionless variable to substitute the particle size in order to get the consistent results without the limitation of the choice of particle size. But currently, this present study just applies this modelling and aims for the completion of the whole modelling.

In this methodology, gaseous particles are the only ones taken into consideration of conducting chemical reactions with adjacent liquid sodium particles or with sodium vapor inside itself. It is reasonable to assign gaseous particles to dominate the reaction because its relatively small

number of particles compared to that of background sodium particles.

The right side of Eq. 3.2 represents the diffusive water vapor towards the interface inside the reference particle. The characteristic length d represent the diffusion length of water vapor to the interface in each particle. The diffusion coefficient of water vapor D_{H_2O} among multiple species within neighbor particles are estimated by utilizing the binary diffusion equation as follows:

$$D_{A-B} = \frac{10^{-3} T^{1.75} \left[\frac{1}{M_A} + \frac{1}{M_B}\right]^{1/2}}{P_{abs}[(\sum v)_A^{1/3} + (\sum v)_B^{1/3}]^2} \tag{3.3}$$

where D_{A-B}, T, P_{abs}, M, $\sum v$ are binary gas phase diffusivity of A in B, temperature, absolute pressure, molecular weights and molecular volumes, respectively.

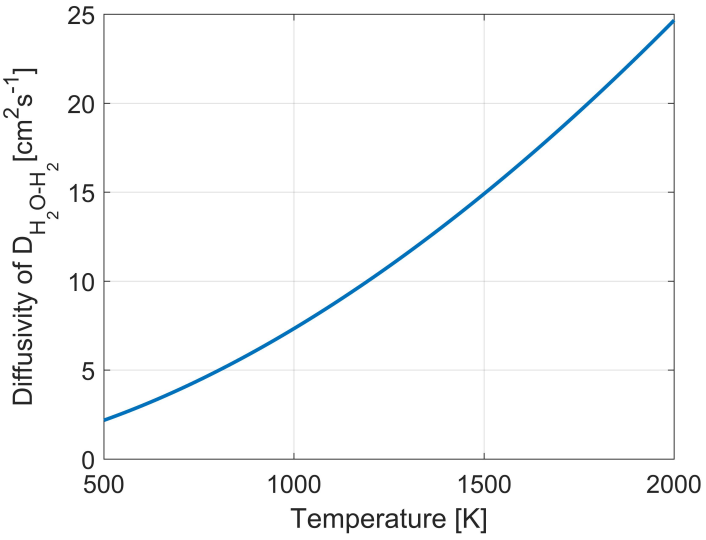

Figure 3.2 – Dependence of binary diffusivity coefficient between H_2O and H_2 on temperature

In this modelling, the diffusion efficient is dependent on the particle temperature and the relationship can be observed in Fig. 3.2.

Molecular volumes of investigated species are listed in Table. 3.1. Dimensionless molecular volumes of Na and $NaOH$ vapor are not available from references because of no existence at the room temperature. An alternative way to approximately estimate their values is proposed here. The binary diffusion coefficient of Na vapor in Ne is measured at 300K in references. By implementing Eq. 3.3, the value of sodium vapor molecular volume can be calculated. A simple summation of three elements Na, O and H produces the molecular volume of $NaOH$ vapor.

In the gaseous particle, the volume of liquid components is neglected and volume fractions of

Table 3.1 – Dimensionless diffusion volumes of investigated species

Species	Diffusion Volumes	Species	Diffusion Volumes
H	2.31	H_2	7.07
O	6.11	H_2O	12.7
Ne	5.59	$NaOH$	24.5
Na	17.0		

each gaseous specie can be represented as follows:

$$Y_{H_2O} + Y_{H_2} + Y_{Na_g} + Y_{NaOH_g} = 1 \tag{3.4}$$

As a difference from the volume fraction, another parameter named mole fraction is defined as follows:

$$Z_{H_2O} + Z_{H_2} + Z_{Na_g} + Z_{NaOH_g} + Z_{Na_l} + Z_{NaOH_l} = 1 \tag{3.5}$$

The volume fraction is mainly used for calculating the diffusion behaviour among gaseous species, while the mole fraction is frequently used in the energy calculation part.

After calculating the binary diffusion coefficient of H_2O in each other gas phase specie, the diffusion coefficient of H_2O in a mixture of species can be evaluated using Eq.(3.5).

$$\frac{1 - Y_{H_2O}}{D_{H_2O}} = \frac{Y_{H_2}}{D_{H_2O-H_2}} + \frac{Y_{Na_g}}{D_{H_2O-Na_g}} + \frac{Y_{NaOH_g}}{D_{H_2O-NaOH_g}} \tag{3.6}$$

The interfacial area density S modelled on the framework of particle methods is proportional to the ratio of liquid sodium particle number density to the initial one.

$$S = \frac{6\beta_{l,g}}{l_0} \tag{3.7}$$

$$\beta_{l,g} = \frac{1}{n_0} \sum_{j=l,i=g} \omega(\|\mathbf{r_j} - \mathbf{r_i}\|) \tag{3.8}$$

where $\beta_{l,g}$ is the ratio of neighbor liquid sodium number density to n_0, and l_0 is the particle diameter. The interface area density is formulated with the consideration of $\beta_{l,g}$ because the limitation of diffusion direction affects the surface reaction rate as well. If the reference gaseous particle is fully surrounded by liquid sodium, water vapor can diffuse in all direction which reduces the diffusion length and promotes the reaction rate consequently.

Table 3.2 – Coefficients in the rate constant equation

Coefficients	A_0	B_0	E_0
Values	4.434e4	0.8812	2.441e4

3.4 Gas-Phase Reaction Model

In addition to the surface reaction model where water vapor reacts with sodium in neighboring liquid particles, a gas-phase reaction model is proposed to account for the reaction between water vapor and sodium vapor. In the particle with multiple gaseous components, water vapor and sodium vapor are assumed to be in a homogeneous mixture. The gas-phase reaction rate is therefore modelled by applying the rate equation as follows:

$$\Gamma_{gp} = K(T)\left[Mo_g Y_{Na_g}\right]\left[Mo_g Y_{H_2O}\right] \tag{3.9}$$

where $K(T)$ is the rate constant and can be formulated in the form of the Arrhenius law.

$$K(T) = A_0 T^{B_0} e^{-E_0/T} \tag{3.10}$$

Empirical coefficients A_0, B_0 and E_0 are adopted from the reference work [5] as shown in Table. 3.2. The dependence of rate constant for the gas-phase reaction on temperature is shown in Fig. 3.3.

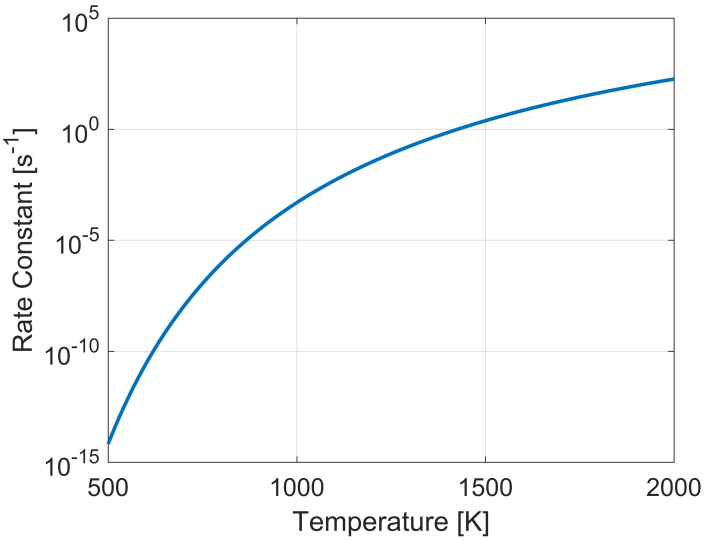

Figure 3.3 – Dependence of rate constant on the temperature

3.5 Evaporation and Condensation

The composition of Na and $NaOH$ vapor in gaseous particles play an important role in influencing the magnitude of both surface reaction rate and gas-phase reaction rate. Adequate evaporation and condensation models for the two species are necessary for the simulation of sodium-water reaction. In the surface reaction model, changes of volume fraction of both species will vary the diffusion coefficient of water vapor among all gaseous species, which results in the variation of surface reaction rate for interfacial particles. In the gas-phase reaction model, variation of Na vapor mole amount has an instant impact on the gas-phase reaction rate.

As seen from the plot, the saturated pressure has an exponential relation with the boiling point, which means only an exponentially change of pressure will have a comparable influence on the boiling temperature. Therefore, it is reasonable to simplify the model by considering the pressure change is limited and the boiling point of sodium hydroxide is stable in this study. Because of the existence of many other components as nucleation sites, it is rarely possible that liquid sodium hydroxide will be superheated without evaporation or sodium hydroxide vapour being supercooled without condensation. It indicates the liquid and gaseous sodium hydroxide can be in an equivalent state.

Therefore, constant boiling points for Na and $NaOH$ vapor are adopted in this study. The boiling point of liquid $NaOH$ at atmospheric pressure as 1663K is used and the boiling point of liquid Na is 1155K. As deliberated in the assumptions, phase temperature is not considered in the multi-component particle whereas an equilibrium temperature will be calculated for each particle.

The latent heat for liquid $NaOH$ evaporation in a standard condition is -219.12kJ/mol, as shown in Eq. 3.11. The negative value represents an exothermal reaction. Eq. **??** presents the standard enthalpy change of sodium-water reaction as -177.46kJ/mol, which can be considered as the reaction heat released at an equilibrium temperature at 298K.

$$NaOH(l) \rightarrow NaOH(g), \Delta H^{298} = -219.12 kJ/mol \tag{3.11}$$

It can be noted that the latent heat of liquid $NaOH$ is larger than the reaction heat, which indicates the sodium hydroxide cannot be heated up by itself to surpassing the boiling point. If we neglect the pressure influence, a circulate process can be imagined that the amount of liquid $NaOH$ will be increased by the generation in the reaction. One can assume the particle is heated up surpassing 1663K due to the chemical heat released. However, by the means of $NaOH$ evaporation, the particle temperature can be moderated sufficiently not above the boiling point of $NaOH$.

This characteristic provides the idea on modelling the evaporation and condensation of $NaOH$ in this study. The evaporation rate within one particle in one time-step depends on the

heat storage in the particle. If the particle temperature surpasses the boiling point of sodium hydroxide and liquid sodium hydroxide has its content at the same time, it is reasonable to consider an adequate amount of sodium hydroxide taking part in the evaporation to overcome the superheating situation. As mentioned, the assumption of evaporation and condensation rates are infinitely fast, which can ensure a sufficient evaporation or condensation for the sake of preventing the superheating or supercooling situation. However, the existing amount of both species, liquid and gaseous sodium hydroxide, may be insufficient to recover to the boiling point or have a surplus amount. In consequence, the evaporation and condensation rate of $NaOH$ can be formulated as follows:

$$\Gamma^{e}_{NaOH} = \begin{cases} \frac{\sum_m (Mo_i Z_m c_{p,m})(T_i - T_{s,NaOH})}{\Delta h_{l,NaOH}}, & (T_i \geq T_{s,NaOH}, \Gamma^{e}_{NaOH} < Mo_i Z_{NaOH(l)}) \\ Mo_i Z_{NaOH(l)}, & (T_i \geq T_{s,NaOH}, \Gamma^{e}_{NaOH} \geq Mo_i Z_{NaOH(l)}) \\ 0, & (T_i < T_{s,NaOH}) \end{cases} \tag{3.12}$$

$$\Gamma^{c}_{NaOH} = \begin{cases} \frac{\sum_m (Mo_i Z_m c_{p,m})(T_{s,NaOH} - T_i)}{\Delta h_{l,NaOH}}, & (T_i \leq T_{s,NaOH}, \Gamma^{c}_{NaOH} < Mo_i Z_{NaOH(g)}) \\ Mo_i Z_{NaOH(g)}, & (T_i < T_{s,NaOH}, \Gamma^{c}_{NaOH} \geq Mo_i Z_{NaOH(g)}) \\ 0, & (T_i > T_{s,NaOH}) \end{cases} \tag{3.13}$$

where Γ^{e}_{NaOH} and Γ^{c}_{NaOH} are the evaporation and condensation amount in mol per time-step for $NaOH$, respectively. $\Delta h_{l,NaOH}$ is the latent heat of $NaOH$, which can be calculated from the standard enthalpy difference between gas and liquid phases. $T_{s,NaOH}$ is the saturated temperature of $NaOH$.

In terms of sodium evaporation, based on the assumption and initial condition, there is no liquid sodium diffusion from liquid particles to gaseous particles. The Na evaporation and condensation models are highly simplified in this study because they contribute less to the maximum temperature formation than $NaOH$. As liquid sodium has an excellent conductivity as the coolant and sufficient amount compared to leaked water vapor in the steam generator, the evaporation of liquid sodium induced by the temperature increment of liquid particles is not considered. Instead, the sodium evaporation occurring at the phase interface is taken into the consideration in the model because remarkable amount of heat is released induced by the surface reaction for interfacial particles.

Therefore, the sodium evaporation rate depends on the surface reaction rate. Only liquid sodium particles which take part in the surface reaction will be considered in the evaporation

model. The Na evaporation rate is formulated in Eq. 3.14.

$$\Gamma^{e}_{Na,j} = \begin{cases} \lambda_e S \gamma_{s,i} \frac{T_i - T_{s,Na}}{T^{1/2}_{s,Na}} \frac{\omega(|\mathbf{r_j} - \mathbf{r_i}|, r_e)}{n_0} & ,(T_i \geq T_{s,Na}) \\ 0 & ,(T_i < T_{s,Na}) \end{cases} \tag{3.14}$$

where $\Gamma^{e}_{Na,j}$ is the evaporation rate in mol per time-step for each liquid particle which conducts surface reaction with gaseous particles. $\gamma_{s,i}$, S, T_i and $T_{s,Na}$ are the surface reaction rate, the interfacial area density, the temperature of investigated gaseous particle i and sodium saturated temperature, respectively. The coefficient of λ_e is set to 0.1.

The condensation of sodium vapor occurs in gaseous particles where sodium vapor exists due to the evaporated sodium at the interface. A well-known Silver-Simpson model is applied for the modelling of sodium condensation rate.

$$\Gamma^{c}_{Na,i} = \begin{cases} \lambda_c S Mo_g R^{1/2} (1 - Y_i) \frac{T_i - T_{s,Na}}{T^{1/2}_{s,Na}} & ,(T_i \leq T_{s,Na}) \\ 0 & ,(T_g > T_{s,Na}) \end{cases} \tag{3.15}$$

where $\Gamma^{c}_{Na,i}$ is the condensation rate in mol per time-step in the gaseous particle i and the coefficient λ_c is set to 0.1 as well.

3.6 Modelling of Reaction Energy

3.6.1 Enthalpy and Heat Transfer

Eq. 3.1 shows the standard enthalpy of formation, which can be considered as the reaction energy released under standard conditions at the temperature of 298K. However, the chemical reaction conducts at varied temperature conditions in the reality. It is not practical to use the standard energy change of -177.46kJ/mol in the simulation. This study proposed a sophisticated method to calculate the reaction energy by means of the calculation of total enthalpy change.

First, one has to calculate the total enthalpy of each species based on the following equation.

$$h_{i,m} = Mo_i (Z_m C_{p,m} (T_i - T_{298}) + \Delta_f h^{\Theta}_m) \tag{3.16}$$

where $h_{i,m}$ is the total enthalpy of species m in particle i. $\Delta_f h^{\Theta}_m$ is the standard enthalpy of formation of species m. Mo_i is the total mole amount of all species in the particle i. Z_m and

Table 3.3 – Standard enthalpy of investigated species

Species	$H_2O(g)$	$H_2(g)$	$Na(g)$	$NaOH(g)$	$Na(l)$	$NaOH(l)$
Standard Enthalpy $\Delta_f h_m^{\Theta}$ [kJ/mol]	-241.83	0.0	107.5	-197.76	2.41	-416.88

$C_{p,m}$ are the mole fraction and molar heat capacity of species m, respectively. T_i is the particle temperature and T_{298} is the temperature at 298K.

It can be straightforward to get the total enthalpy definition for each multi-component particle by the summation of each species' enthalpy as follows:

$$h_i = Mo_i \sum_m (Z_m C_{p,m}(T_i - T_{298}) + \Delta_f h_m^{\Theta}) \tag{3.17}$$

where h_i is the total enthalpy of particle i. For gaseous particles, species m refer to 6 components, which are $H_2O(g)$, $H_2(g)$, $Na(g)$, $NaOH(g)$, $Na(l)$ and $NaOH(l)$. However, liquid particles only have one species which is $Na(l)$. The standard enthalpy values of six species investigated in this study are listed in Table. 3.3.

Concerning gaseous particles with multiple components, the overall heat conductivity k_i for each specific particle is calculated as follows:

$$k_i = \frac{1}{2}\left[\sum_j Z_j k_j + (\sum_j \frac{Z_j}{k_j})^{-1}\right] \tag{3.18}$$

Heat conductivity between two particles with varied components can be derived by assuming no heat resistance at the interface, which turns out to be the harmonic mean value:

$$k_{i,j} = \frac{2k_i k_j}{k_i + k_j} \tag{3.19}$$

In the present model, the heat transfer between gas and liquid phase species in the same gaseous particle is not considered. For the heat conductivity between gaseous and liquid particles at the interface, the value calculated by using Eq. 3.19 in fact is underestimated compared to the realistic heat transfer coefficient. The convective heat transfer coefficient used in SERAPHIM is 10,000 W/m^2/K, which is about tens of times larger than the estimated conductivity for the initial gaseous and liquid particles.

Sodium-water reactions are characterised with considerable reaction heat release. In the reaction model, reaction heat is assumed to be carried by reaction products of hydrogen and sodium hydroxide

3.6.2 Governing Equations

The present research deals with multi-component and multi-phase chemical reaction models in the Lagrangian frame. Two varied phases of particles are taken into account when building the governing equations. As mentioned in the reaction models, surface reaction and gas-phase reaction will only generate products in the gaseous particles. Gaseous components will conduct the diffusion among gaseous particles while there is no liquid diffusion concerned in this study. Therefore the main concern in this research is modelling the physical phenomena reasonably among gaseous particles.

This research focuses on modelling the reaction process at the phase interface and the propagation of reaction zones among tube bundles. The dynamic change does not contribute a lot to the overall release and propagation of reaction energy in a longer duration than the time scale of some rapid phenomena, such as reaction and adiabatic expansion. Hence, for the simplification, the pressure change due to the density and temperature variation of gaseous particles is neglected in the present work. A detailed simplification strategy will be explained after the introduction of governing equations.

The mass conservation for multiple species in particle method is ensured by the transport equations as follows:

For gaseous species in gaseous particles:

$$\frac{DMoZ_m}{Dt} = \underbrace{\nabla \cdot (D_m \nabla Mo_g Y_m)}_{\text{2nd step}} + \underbrace{\Gamma_m^{sf} + \Gamma_m^{gp}}_{\text{1st step}} + \underbrace{\Gamma_m^e - \Gamma_m^c}_{\text{3rd step}} \tag{3.20}$$

where Mo is the total mole amount of all 6 species in the particle. Z_m is the molar fraction of species m. D_m is the diffusion coefficient of species m. Mo_g is the total mole amount of all 4 gaseous species in the particle. Y_m is the volume fraction of gaseous species m. Γ_m^{sf} and Γ_m^{gp} refer to the molar change of species m induced by surface reaction and gas-phase reaction, respectively. Γ_m^e and Γ_m^c correspond to the molar change of species m induced by evaporation and condensation, respectively.

For liquid species in gaseous particles:

$$\frac{DMoZ_m}{Dt} = -\Gamma_m^e + \Gamma_m^c + \Gamma_m^{sf} + \Gamma_m^{gp} \tag{3.21}$$

For liquid species in liquid particles:

$$\frac{DMoZ_{Na}}{Dt} = -\Gamma_{Na}^{sf} - \Gamma_{Na}^e \tag{3.22}$$

where Γ_{Na}^{sf} represents the mole amount of liquid sodium participating in the surface reaction in the liquid particle. Γ_{Na}^e is the mole amount of liquid sodium to be vaporised.

The momentum equation is given in Eq. 3.23. The discretising method has been introduced in the Chapter 2.

$$\frac{\mathrm{D}\rho\mathbf{u}}{\mathrm{D}t} = -\nabla P + \nabla\cdot\left(\mu\nabla\mathbf{u}\right) + \mathbf{f} \tag{3.23}$$

The energy equation is formulated as:

$$\frac{Dh}{Dt} = \underbrace{V\nabla\cdot k\nabla T}_{\text{2nd-3rd step}} + \underbrace{S_{sf,Na}}_{\text{1st step}} + \underbrace{S_{dif,in} + S_{dif,out}}_{\text{2nd step}} + \underbrace{S_e + S_c}_{\text{3rd step}} \tag{3.24}$$

where h is the total enthalpy of all 6 species in the particle. V is the particle volume. $S_{sf,Na}$, $S_{dif,in}$, $S_{dif,out}$, S_e, S_c are the enthalpy change of the particle induced by liquid sodium participation in surface reaction, incoming species diffusion, outgoing species diffusion, evaporation and condensation, respectively. Because all reactants and products are in the same particle in gas-phase reaction with no heat distributed to neighbouring particles, the total enthalpy change induced by gas-phase reaction is 0 in the investigated particle.

Concerning the molar fraction and volume fraction, the following relationship exists. The two variables will be updated simultaneously a few times in the calculation using a fractional step method.

$$\frac{DMoZ_m}{Dt} = \frac{DMo_g Y_m}{Dt} \tag{3.25}$$

3.6.3 Numerical Procedure

Regarding the fractional step method, one first only consider the contribution of reactions (Γ_m^{sf}, Γ_m^{gp}) to the molar change in Eq. 3.20 to get a first intermediate value ($Mo_i^{n'}$, $Z_{m,i}^{n'}$) for each species. As mentioned, $Mo_{g,i}^{n'}$ and $Y_{m,i}^{n'}$ will be calculated at the same time.

$$Mo_i^{n'} Z_{m,i}^{n'} - Mo_i^n Z_{m,i}^n = (\Gamma_m^{sf} + \Gamma_m^{gp})\Delta t \tag{3.26}$$

With an updated volume fraction $Y_m^{n'}$ for gaseous species, a new diffusion coefficient $D_m^{n'}$ will be calculated as well, which is used in the second intermediate step calculation considering the diffusion term in Eq. 3.20. Therefore, use Eq. 3.25 to obtain the second intermediate values ($Mo_{g,i}^{n''}$, $Y_{m,i}^{n''}$, $Mo_i^{n''}$, $Z_{m,i}^{n''}$) for each particle.

$$\frac{Mo_{g,i}^{n''} Y_{m,i}^{n''} - Mo_{g,i}^{n'} Y_{m,i}^{n'}}{\Delta t} = \frac{2d}{n_0\lambda}\sum_{j\neq i}\frac{2D_{m,i}^{n'} D_{m,j}^{n'}}{D_{m,i}^{n'} + D_{m,j}^{n'}}(Mo_{g,j}^{n'} Y_{m,j}^{n'} - Mo_{g,i}^{n'} Y_{m,i}^{n'})\omega(\left\|\mathbf{r_j} - \mathbf{r_i}\right\|) \tag{3.27}$$

So far, the molar change of species due to reaction and diffusion are taken into account.

In terms of enthalpy change, Eq. 3.28 shows the total enthalpy of the investigated particles just after chemical reaction with the assumption of no heat being transported or distributed to other particles.

The total enthalpy at the first intermediate step is given as:

$$h_i^{n'} = h_i^n + (S_{sf,Na})\Delta t \tag{3.28}$$

The total enthalpy h_i of each particle is calculated as follows:

$$h_i = Mo_i \sum_m (Z_{m,i}(C_{p,m}(T_i - T_{298}) + \Delta_f h_m^\Theta)) \tag{3.29}$$

The total enthalpy at the second intermediate step can be obtained as:

$$h_i^{n''} = h_i^n + (S_{sf,Na} + S_{dif,in} + S_{dif,out})\Delta t \tag{3.30}$$

$$S_{sf,Na}\Delta t = \sum_j (\Gamma_{sf,j}(C_{p,Na(l)}(T_j - T_{298}) + \Delta_f h_m^\Theta)) \tag{3.31}$$

where $\Gamma_{sf,j}$ is the mole amount of liquid sodium participating in the surface reaction for neighbouring liquid sodium particle j.

$$S_{dif,in}\Delta t = \sum_{m,in} (Mo_i^{n''} Z_{m,i}^{n''} - Mo_i^{n'} Z_{m,i}^{n'})(C_{p,m}(T_j - T_{298}) + \Delta_f h_m^\Theta) \tag{3.32}$$

$$S_{dif,out}\Delta t = \sum_{m,out} (Mo_i^{n''} Z_{m,i}^{n''} - Mo_i^{n'} Z_{m,i}^{n'})(C_{p,m}(T_i - T_{298}) + \Delta_f h_m^\Theta) \tag{3.33}$$

Now it is available to calculate the equilibrium temperature $T_i^{n'}$ after reaction and diffusion. $h_i^{n''}$ can also be expressed by using the unknown $T_i^{n'}$ as follows:

$$h_i^{n''} = Mo_i^{n''} \sum_m (Z_m^{n''}(C_{p,m}(T_i^{n'} - T_{298}) + \Delta_f h_m^\Theta)) \tag{3.34}$$

Substitute Eq. 3.30 in Eq. 3.34, the equilibrium temperature $T_i^{n'}$ for each particle can be calculated. Then the enthalpy change induced by the heat conduction among particles is calculated as follows:

$$\frac{Mo_i^{n''}\sum_m(Z_m^{n''}C_{p,m}(T_i^{n''}-T_i^{n'}))}{\Delta t} = V\frac{2d}{n_0\lambda}\sum_{j\neq i}k_{i,j}(T_j^{n'}-T_i^{n'})\omega(\|\mathbf{r_j}-\mathbf{r_i}\|) \tag{3.35}$$

where $T_i^{n''}$ is the temperature value for each particle after the heat conduction.

Finally, evaporation and condensation of Na and $NaOH$ will be considered by comparing the temperature of $T_i^{n''}$ to their boiling points. Because no evaporation and condensation occurs for H_2O and H_2, $Z_{H_2O}^{n''}$ and $Z_{H_2}^{n''}$ are equal to $Z_{H_2O}^{n+1}$ and $Z_{H_2}^{n+1}$, respectively.

For example of $NaOH$, the following equations are used for the calculation of Mo_i^{n+1} and $Z_{NaOH(l)}^{n+1}$ in gaseous particles.

$$Mo_i^{n+1}Z_{NaOH(l)}^{n+1} = Mo_i^{n''}Z_{NaOH(l)}^{n''} - \Gamma_{NaOH(l)}^{e} + \Gamma_{NaOH(g)}^{c} \tag{3.36}$$

$$Mo_i^{n+1}Z_{NaOH(g)}^{n+1} = Mo_i^{n''}Z_{NaOH(g)}^{n''} + \Gamma_{NaOH(l)}^{e} - \Gamma_{NaOH(g)}^{c} \tag{3.37}$$

The temperature T_i^{n+1} at $n+1$ time-step can be calculated in Eq. 3.38.

$$Mo_i^{n+1}\sum_m(Z_m^{n+1}(C_{p,m}(T_i^{n+1}-T_{298})+\Delta_f h_m^{\Theta})) = Mo_i^{n''}\sum_m(Z_m^{n''}(C_{p,m}(T_i^{n''}-T_{298})+\Delta_f h_m^{\Theta})) \tag{3.38}$$

For example of Na, the following equations are used for the calculation of Mo_i^{n+1} and $Z_{Na(l)}^{n+1}$ in gaseous particles.

$$Mo_i^{n+1}Z_{Na(l)}^{n+1} = Mo_i^{n''}Z_{Na(l)}^{n''} - \Gamma_{Na(l)}^{e} + \Gamma_{Na(g)}^{c} \tag{3.39}$$

$$Mo_i^{n+1}Z_{Na(g)}^{n+1} = Mo_i^{n''}Z_{Na(g)}^{n''} + \Gamma_{Na(l)}^{e} - \Gamma_{Na(g)}^{c} \tag{3.40}$$

Because the sodium evaporation comes from the liquid particles, the calculation of temperature T_i^{n+1} at $n+1$ time-step is slightly different from Eq. 3.38.

$$Mo_i^{n+1}\sum_m (Z_m^{n+1}(C_{p,m}(T_i^{n+1}-T_{298})+\Delta_f h_m^{\Theta})) = Mo_i^{n''}\sum_m (Z_m^{n''}(C_{p,m}(T_i^{n''}-T_{298})+\Delta_f h_m^{\Theta})) + \sum_j (\Gamma_j^e(C_{p,Na(l)}(T_j-T_{298})+\Delta_f h_m^{\Theta})) \tag{3.41}$$

Up to now, the proposed fractional step method for discretising the mass and energy governing equations is shown from time step n to $n+1$.

4 Simulation and Verification

Chapter 2 illustrates the modification and improvement of the original MPS method in terms of the thermo-hydraulic framework. Chapter 3 gives a thorough explanation of modelling the chemical reaction on the basis of particle methods. This chapter is focused on the investigation of the simulation results by coupling both thermo-hydraulic and chemical reaction models using particle methods.

4.1 Particle and Time-Step Size

Before the simulation, a discussion on the choice of particle and time-step size is conducted firstly. In the original MPS method, the time-step size limited by Courant number has been applied, which depends on the maximum velocity and particle size shown in Eq. **??**.

$$\Delta t \leq min(C_c \frac{d}{\|\mathbf{u_i}\|}) \tag{4.1}$$

where Δt is the time-step size. C_c is the Courant number, normally smaller than 0.2. d is the particle diameter and $\mathbf{u_i}$ is the velocity of particle i.

The viscosity, mass diffusion and heat transport equations are solved explicitly in the present method, which in fact requires the consideration on choosing adequate time-step and particle size based on the diffusion number.

The diffusion number constrained by the viscosity, heat conductivity, mass diffusion coefficient is given as follows:

$$\Delta t \leq min(C_d \frac{d^2 \rho_i}{2\mu_i}) \tag{4.2}$$

$$\Delta t \leq min(C_d \frac{d^2 \rho_i C_p}{k_i}) \tag{4.3}$$

$$\Delta t \leq min(C_d \frac{d^2}{D_i}) \tag{4.4}$$

where C_d is the diffusion number.

As mentioned, the gas-liquid heat conductivity in my case is much underestimated than the coefficient used in SERAPHIM. A larger heat conductivity also requires a smaller time-step.

The particle size also has the influence on the surface reaction rate and heat transportation process. Sensitivity analysis needs to be done in the future work concerning this point. Another concern is that a larger particle size may not reflect some detailed thermo-hydraulics phenomena. But concerning the application on sodium-water reaction, the estimation on the products and temperature distribution is in priority.

4.2 Analytical Conditions

To start with, a preliminary chemical reaction in a simplified model without tubes is conducted. The structure of tube bundles has the influence on the propagation of steam jet and reaction zone. Excluding the tube structure to conduct the simulation can make it available to investigate the characteristics of reaction phenomena independently.

The configuration for the simulation is shown in Fig. 4.1. The geometric dimensions of the configuration are listed in Table. 4.1. Particles used in this simulation case have a diameter as 0.01 m. The breach for leakage steam is located at the bottom center of the configuration, with a width as three times of the particle diameter.

Liquid sodium particles are filled in the model up to the height of 1.5 m with a free-surface. Above the sodium surface, no particle is arranged inside the sodium tank. In order to verify the mass and energy conservation, the configuration is closed at the top to prevent any leakage of particles departing from the computation domain. The margin of the void space above the sodium surface is sufficiently large to not influence a continuous injection of steam particles.

The velocity of steam particles is assigned as 400 m/s initially on the vertical direction with no horizontal profiles until surpassing the bottom wall. The detail of initial particle density for two phases is presented in Table. 4.1 as well. The initial temperature of leakage steam is 641 K while the temperature of background sodium is set at 742 K.

In this simulation case, steam particles are continuously injected into the sodium side with a

Table 4.1 – Geometric dimensions and initial conditions for simulation cases.

Geometric Dimensions		Initial Conditions	
Items	Value	Items	Value
Particle diameter	0.01 m	Steam velocity	X: 0 m/s, Y: 400 m/s
Inner width of sodium tank	1.01 m	Steam density	2.0 kg/m^3
Height of liquid sodium	1.50 m	Sodium density	896.0 kg/m^3
Thickness of simulation domain	0.01 m	Temperature of steam	641 K
Breach width	0.03m	Temperature of liquid sodium	742 K

duration of 10 ms. After 10 ms, no more new steam particles will be added into the computation domain while the simulation continues until 20 ms.

4.3 Investigation of Simulation Results

The purpose of this simulation is to investigate the reaction process in a short duration time and verify the reaction model. As the sodium-water reaction is very aggressive and complex, the transient physical property is largely varied by the simulation time. It is of great importance to investigate the transient physical property of particles. Therefore, four timestamps during the simulation are chosen for the analysis, which are at 1 ms, 5 ms, 10 ms and 15 ms.

As mentioned, the transient property varies considerably along the simulation time for the sodium-water chemical reaction. The transient property is important as some extreme values can result in specific phenomena, such as explosion due to the high temperature and pressure. By investigating the transient property, one can have an intuitive impression on how the reaction undergoes and verify the model quantitively.

In this research, time-averaged physical properties are investigated as well. Considering the impact on the tube failure, the failure frequency of tubes depends on the cumulative periods of distribution of high temperature and corrosive reaction products. It is reasonable to figure out the location where high temperature and corrosive products appear longer in the simulation.

4.3.1 Velocity Field

In the case of applying the high-speed steam injection, the velocity attenuation is of great importance for the investigation. The absolute speed of each particle at 5ms and 10ms in the simulation has been plotted in Fig. 4.1.

As shown in Fig. 4.1, the initial injection velocity attenuates frequently around the exit of leakage. From the point view of momentum conservation, though the steam particles are injected with very high velocity, they slows down considerably when interact with liquid

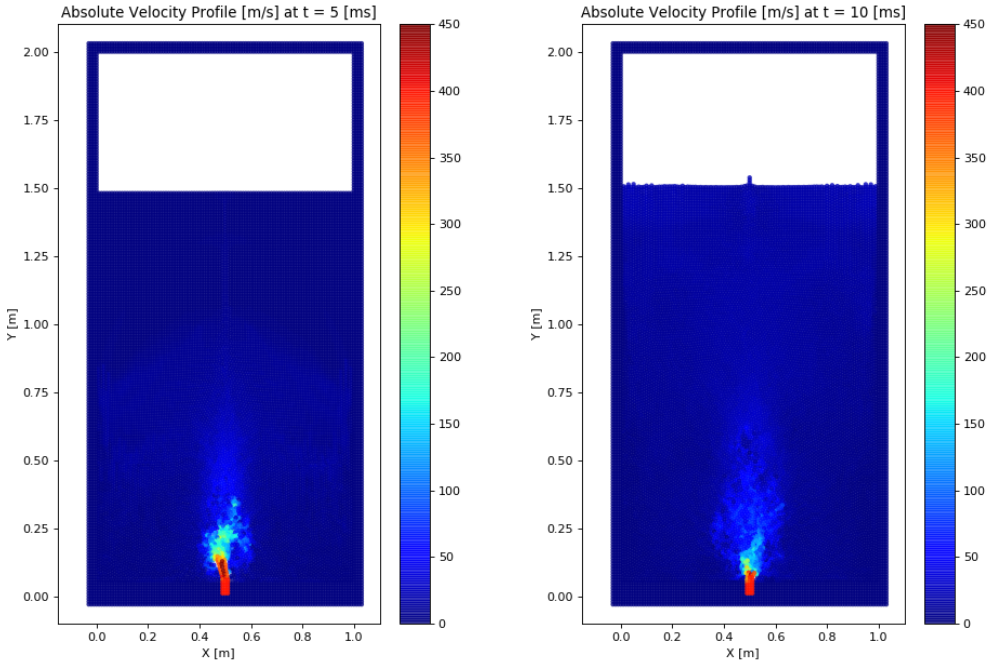

(a) t = 5ms (b) t = 10ms

Figure 4.1 – Absolute velocity profile at 5ms and 10ms

sodium particles which are much heavier than steam particles.

Since the compressibility of gas phase is not fully developed, no constraction or expansion will take place around the leakage exit. In order to achieve the stability of computation, average particle density are taken into account for interfacial gaseous particles. By doing so, an efficient momentum exchange between two phases will avoid the overlap of particles and mitigate extremely high acceleration for lighter density particles. Therefore, steam particles can be smoothly injected into the liquid sodium side without causing the instability of computation.

It can be observed that some particles around the breach reach a velocity of over 400 m/s. Due to the slowing down of particle at the interface, steam particles are accumulated around the breach and the number density of particles are much higher locally. Therefore, high-speed particles will obtain horizontal velocity profiles as well because of the pressure gradient caused by number density variation.

It raises a question that whether the compressibility of gas phase has a large effect on the simulation results. As a difference from the practical issue, this simulation case adopts a constantly initial velocity as one boundary condition whereas in the reality pressure at the injection side is constant. The former one is used in this simulation for the aim of simplification. In a more

practical case, high pressurised water vapor will expand first because of the pressure difference from the background sodium. After water vapor obtains high speeds, the distribution of vapor around the leakage exit becomes dilute, which in feedback results in contraction of water vapor. Therefore, a relatively stable reaction zone forms when the strength of expansion and contraction are equivalent.

As this research is mainly focusing on the reaction consequence, it is reasonable to neglect the compressibility around the leakage exit while investigating the reaction process at the phase interface.

4.3.2 Distribution of Reactants and Products

In this section, a thorough investigation on different reactants and products is conducted. Excluding the initial two reactants of water vapor and liquid sodium, and two products of hydrogen and liquid sodium hydroxide, sodium vapor and sodium hydroxide vapor induced by the evaporation are considered as well.

Fig. 4.2 presents the water vapor mole amount at 1ms, 5ms, 10ms and 15ms, respectively. In all figures, the mole amount of water vapor shows a gradient distribution from red to blue, representing a higher concentration to a lower one. The initial mole amount of water vapor is 1.11e-4 mol per particle. During the simulation, this initial value is the maximum value as well.

At 1ms, one can notice that higher distributions of mole amount exist in the jet interior and lower ones at the interface. It makes sense that the reaction takes place at the interface and consumes water vapor frequently, while the water vapor in the jet interior does not take part in the reaction because of no contact with liquid sodium at the early beginning of simulation.

The gradient distribution of water vapor mole amount observed at the interface has a width more than one particle diameter. It indicates the consequence of mass diffusion of water vapor from neighbouring particles to interfacial particles. In Fig. 4.2a, a continuous water vapor distribution can still be observed while in Fig. 4.2b, Fig. 4.2c and Fig. 4.2d, dispersed distribution are shown due to the impact of reaction and oscillation of injection jet. Some water vapor particles are exhausted in the reaction process of liquid sodium. It is more obviously that after stopping the injection at 10 ms, the distribution of water vapor at 15 ms are more diluted.

Fig. 4.3 with hydrogen mole amount plotted present an opposite situation to the water vapor. At 1 ms in Fig. 4.3a, hydrogen is built-up at the interfacial gaseous particles. With the injection moving forward, the initially interfacial particles are mainly still situated at the interface conducting the reaction with liquid sodium. Therefore, interfacial particles accumulate the reaction products of hydrogen and sodium hydroxide along the simulation until they pass into the interior of water vapor jet.

The distribution of sodium vapor mole amount in particles are presented in Fig. 4.4, while the distribution of sodium hydroxide vapor mole amount is shown in Fig. 4.5. All these figures show a similar characteristic that the distribution of sodium vapor and sodium hydroxide vapor are more dispersed than water vapor and hydrogen. Because generating both components is based on the evaporation model, only when particles with higher temperature than their boiling points, sodium and sodium hydroxide vapor can be generated, which is not a continuous process. The diffusion coefficient of both components are much smaller than water vapor and hydrogen. Therefore, the diffusion impact of both components on their distributions is relatively small. The diffusion happens from higher concentration to lower one which means they diffuse from the generation sites to other location where no reaction happens. Therefore, it is more likely that both components diffuse from the particles at high temperature to the ones at low temperature, which results in an instant condensation into liquid components. Therefore, the distribution of sodium vapor and sodium hydroxide vapor are more dispersed than water vapor and hydrogen.

In this model, there are four gaseous components which are water vapor, hydrogen, sodium vapor and sodium hydroxide vapor. In gaseous particles, due to the condensation of sodium vapor and sodium hydroxide vapor, these particles are not fully occupied by gaseous components. Fig. 4.7 present the volume fraction of hydrogen among the other gaseous components. It is much evident that hydrogen is accumulated in the interfacial particles which will suppress the chemical reaction rate.

In Fig. 4.7, evolutions of total mole amount of six components along the simulation time are plotted, respectively. As mentioned, the water vapor injection continuous until 10 ms. Therefore, it is observed that the evolution rate of all components mitigates after 10 ms. Though the cumulative generation of hydrogen in interfacial particles has a negative feedback on the its generation rate, the continuous injection and progressively increasing surface of reaction zones compensate the negative feedback. Thus, an almost constant generation rate of hydrogen can be observed in Fig. 4.7d.

Concerning the condensation of sodium vapor and sodium hydroxide vapor, the reduction tendency of evolution curves in Fig. 4.7 shows the phenomena. On one hand, since there is no more injection of new water vapor particles after 10 ms, the total reaction rate decreases and less chemical reaction heat is released to keep particles at higher temperature than their boiling points. On the other hand, mass diffusion and heat conduction continue to dissipate the heat to neighbouring particles. It can be sure that sodium hydroxide vapor starts to condensate earlier and more quickly than sodium vapor, which can be noticed from Fig. 4.7.

Fig. 4.8 presents the vapor fraction of sodium hydroxide with respect to the simulation time. The maximum vapor percentage of sodium hydroxide is around 4%, which indicates the latent heat of sodium hydroxide evaporation is considerably larger than the reaction heat released. Only 4% of evaporation of liquid sodium hydroxide can suppress the high temperature to the level of its boiling point, which can be observed in the next section.

4.3.3 Temperature Field

In this section, transient temperature profiles are plotted in Fig. 4.9 at four different timestamps. As the reaction takes place firstly at the interface, the reaction heat is released into the interfacial particles. As a consequence, high temperature particles are mainly situated at the interface as shown in Fig. 4.9. The particles around the leakage exit are nearly new water vapor particles with initial temperature values. After 10 ms, the high temperature zone appear in the interior of water vapor jet due to the convection of interfacial particles to the inner part.

As mentioned in the previous section, only 4% of the evaporation of liquid sodium hydroxide can mitigate particle temperature to the boiling point. It indicates that no particle after the reaction will have a temperature surpassing the boiling point of sodium hydroxide, which can be observed in Fig. 4.9 where the maximum temperature is around 1650 K.

Apart from the transient temperature, time-averaged temperature profiles are shown in Fig. 4.10. The time-averaged temperature distribution differs from the transient temperature that a more gradient distribution can be observed. Moreover, the high temperature zones appear around two sides of the leakage exit at the beginning and then propagate to the interior of water vapor jet with a certain distance from the breach. The maximum time-averaged temperature is around 1400 K.

Once particles are injected into the liquid sodium, particles on two sides of the jet will contact with sodium for a much longer time than those at other locations. Due to the termination of injection, gaseous particles moves much slower after 10 ms. It is accounted for the high temperature zone occur in the inner part as well departing from the breach with a distance.

4.4 Verification of Mass and Energy Conservation

In this simulation case, chemical reaction, mass diffusion, evaporation and condensation have the influence on the mass evolution of each component. To verify the accuracy of those models implemented, three elements of hydrogen, oxygen and sodium are investigated with their mass evolution during the period of reaction.

The total mass evolution for each isotope is plotted in Fig. 4.11. The flat curves of toal mass evolution for three isotopes indicate the mass conservation has been achieved. The modelling of reaction, mass diffusion, evaporation and condensation are proved to be solved accurately in this research.

For the verification of energy conservation, the absolute enthalpy evolution of all species in the configuration is plotted in Fig. 4.12. Likewise, a flat curve of enthalpy evolution has been achieved in this multidisciplinary simulation. The modelling of reaction energy, enthalpy change induced by diffusion, evaporation and condensation, and heat conduction are proved to be solved in the computation correctly.

After the verification of the implemented models, validation of simulation results by comparing to experimental data or validated date is necessary for proving the feasibility and credibility of implementing the proposed models for further research.

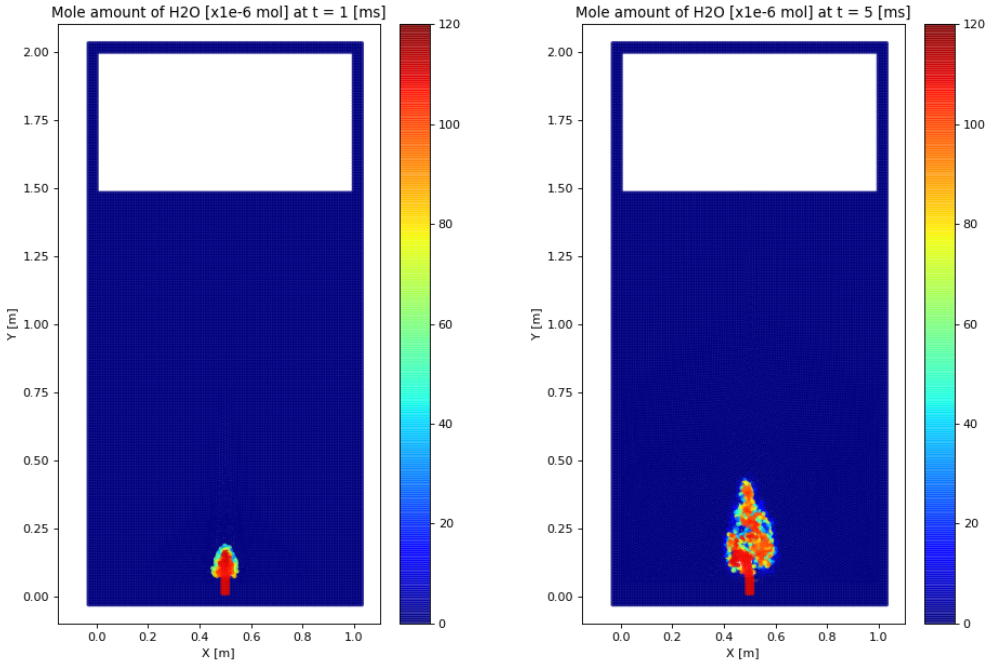

(a) t = 1ms

(b) t = 5ms

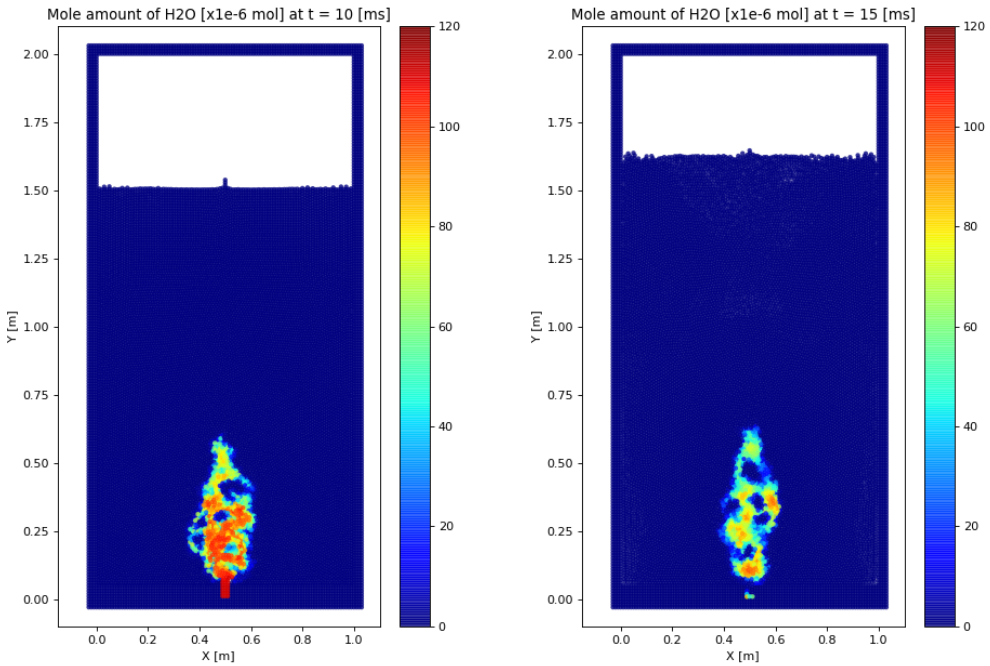

(c) t = 10ms

(d) t = 15ms

Figure 4.2 – Mole amount distribution of H_2O at 1, 5, 10 15ms

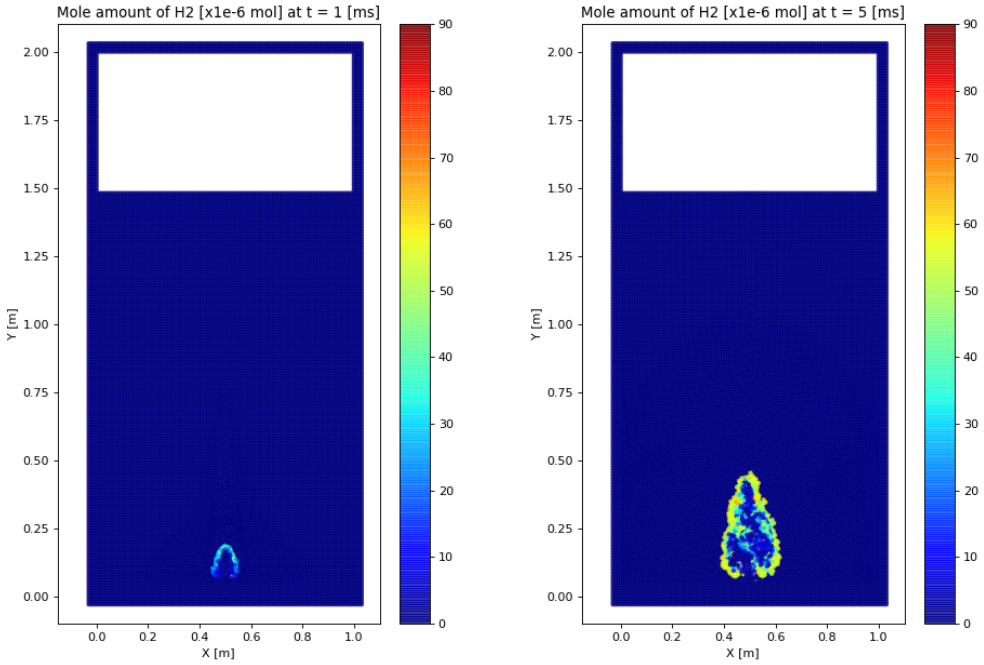

(a) t = 1ms

(b) t = 5ms

(c) t = 10ms

(d) t = 15ms

Figure 4.3 – Mole amount distribution of H_2 at 1, 5, 10 15ms

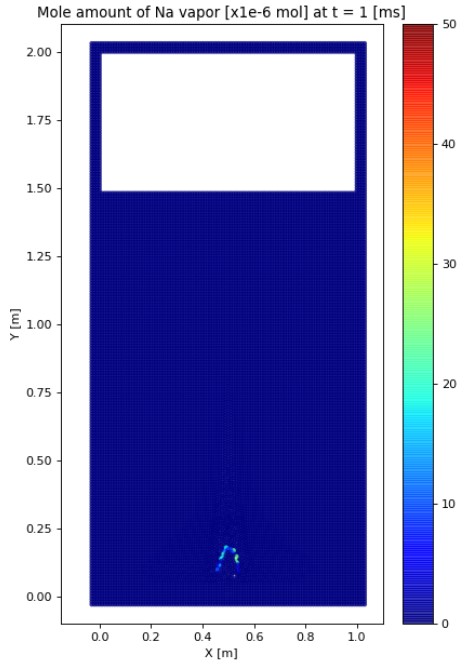

(a) t = 1ms

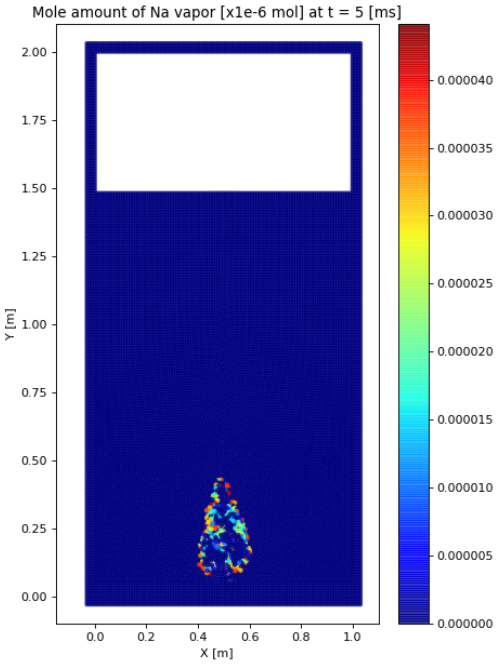

(b) t = 5ms

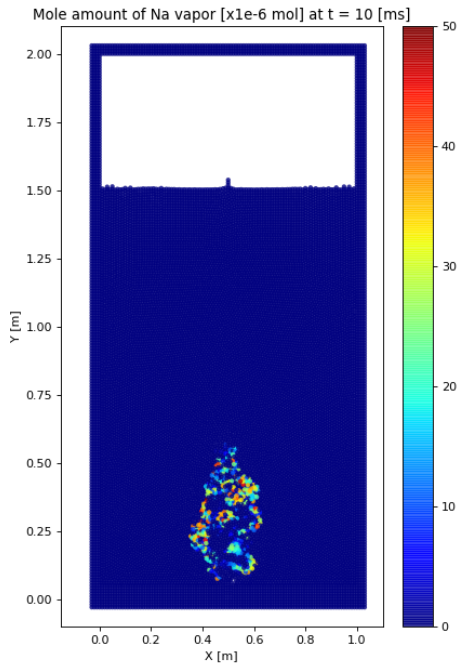

(c) t = 10ms

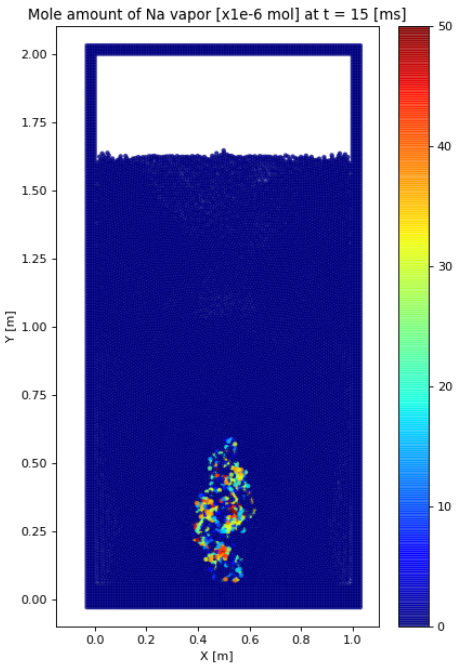

(d) t = 15ms

Figure 4.4 – Mole amount distribution of Na Vapor at 1, 5, 10 15ms

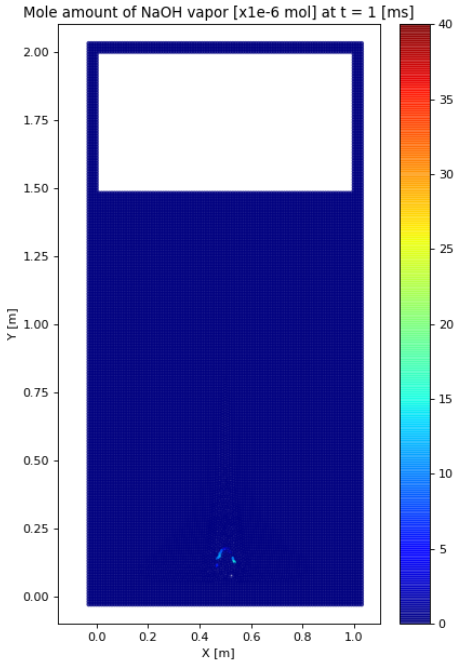

(a) t = 1ms

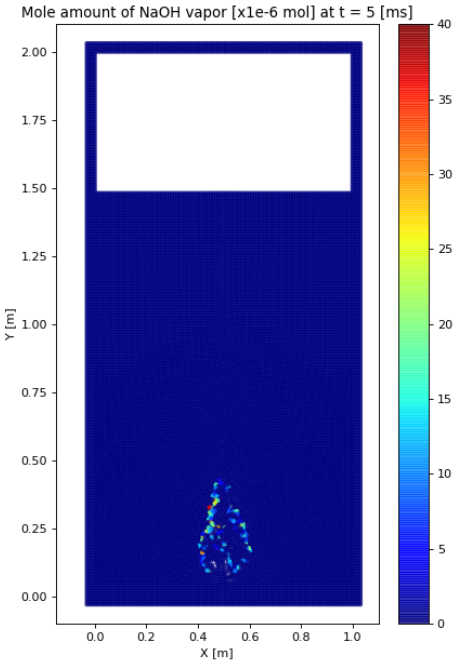

(b) t = 5ms

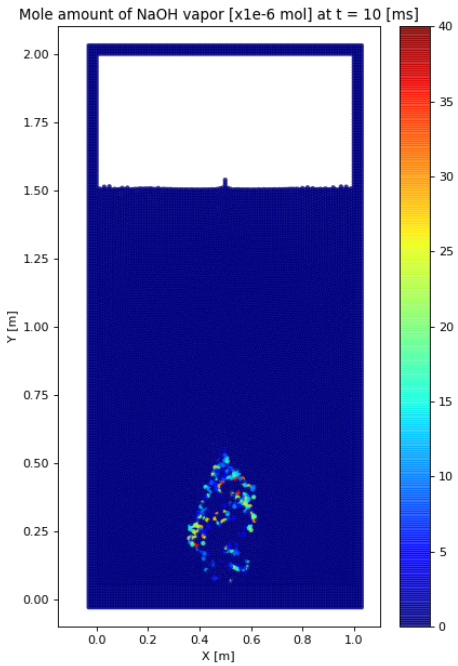

(c) t = 10ms

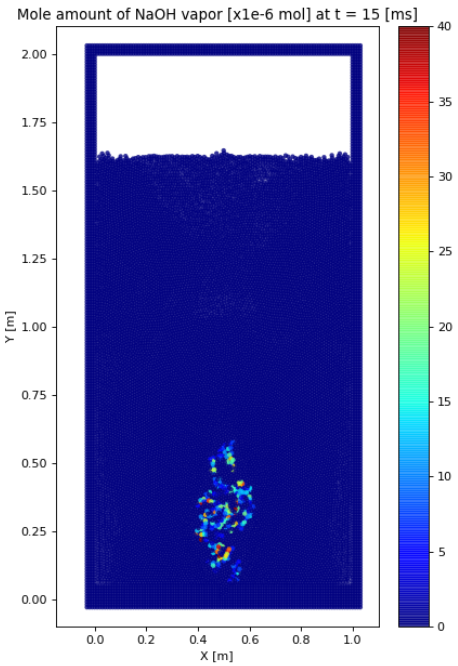

(d) t = 15ms

Figure 4.5 – Mole amount distribution of NaOH Vapor at 1, 5, 10 15ms

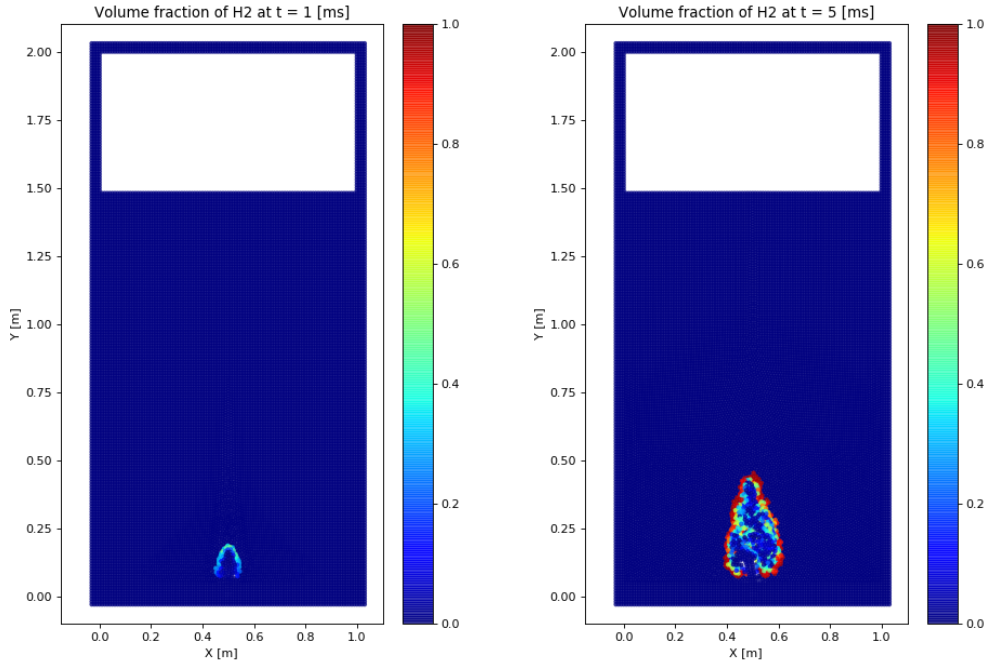

(a) t = 1ms

(b) t = 5ms

(c) t = 10ms

(d) t = 15ms

Figure 4.6 – Volume fraction of H_2 at 1, 5, 10 15ms

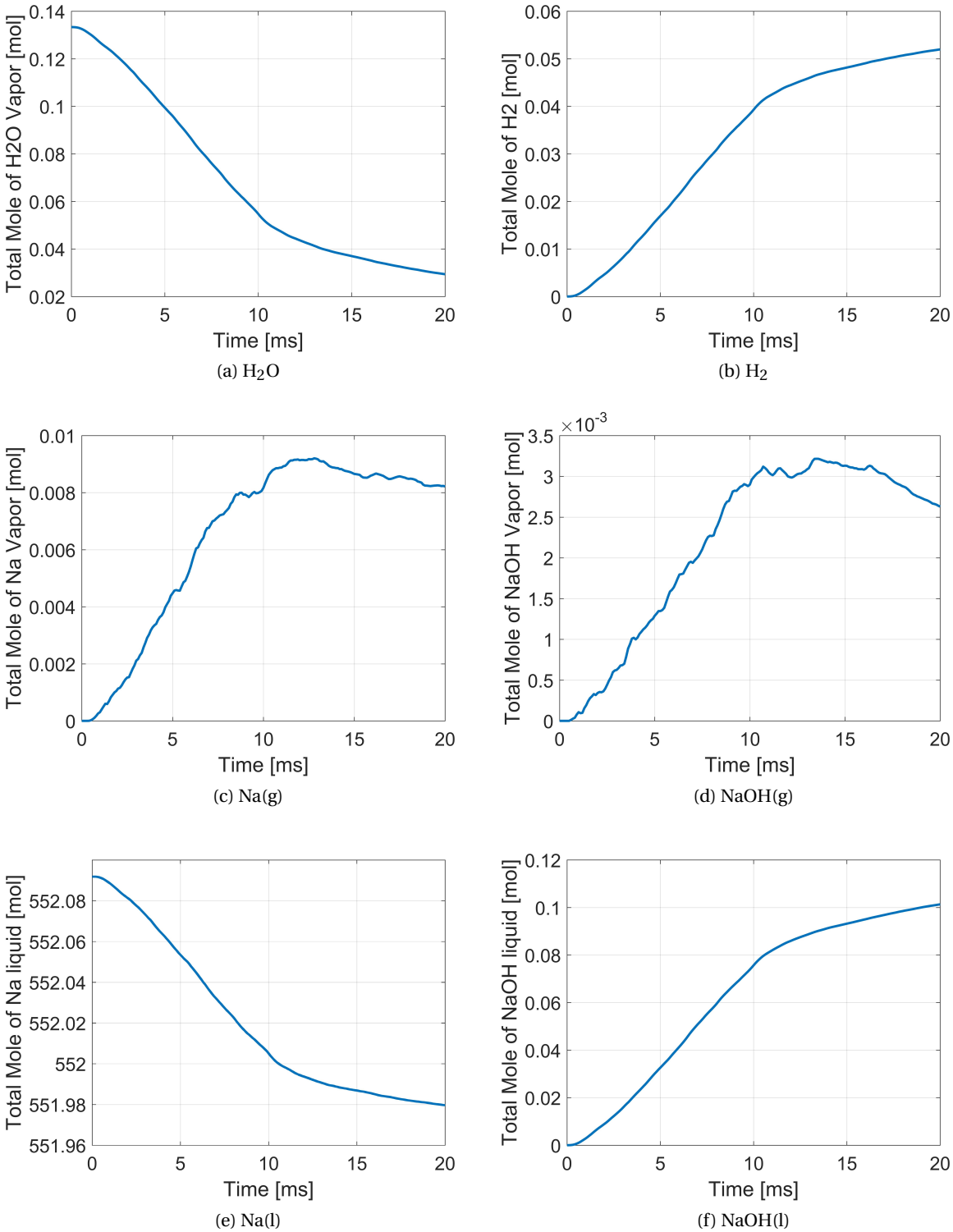

(a) H_2O (b) H_2 (c) Na(g) (d) NaOH(g) (e) Na(l) (f) NaOH(l)

Figure 4.7 – Evolution of molar amount of H_2O, H_2, Na(g), NaOH(g), Na(l), NaOH(l) within 20 ms.

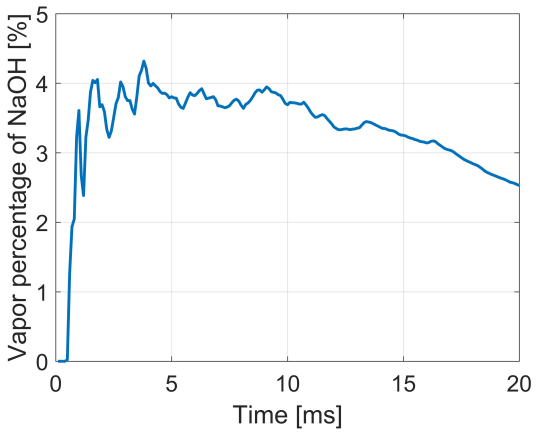

Figure 4.8 – Vapor fraction of NaOH within 20 ms.

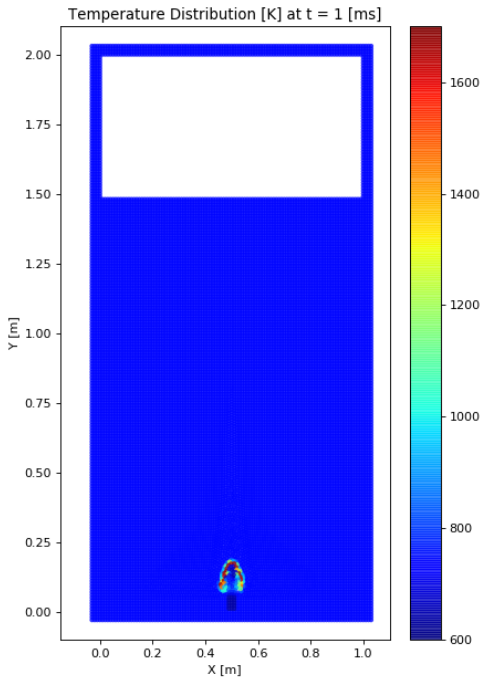

(a) t=1ms

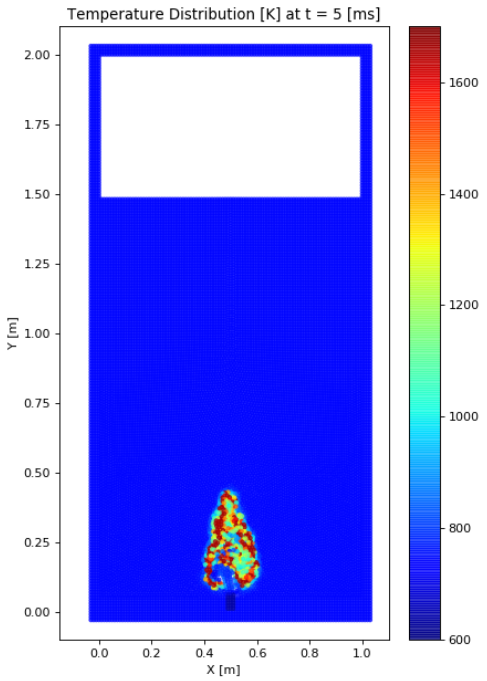

(b) t=5ms

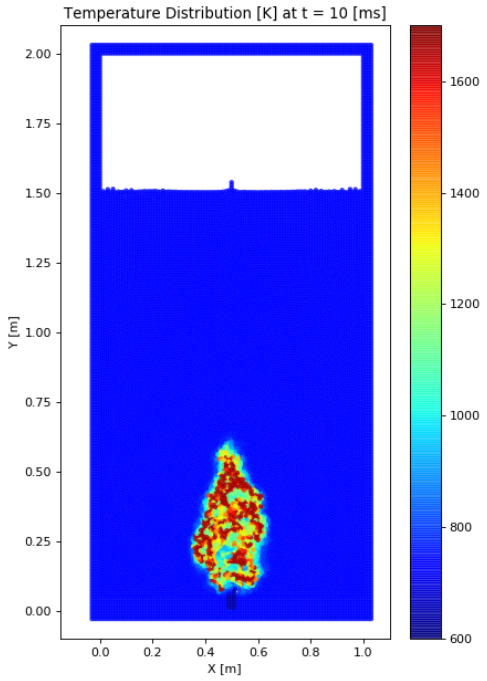

(c) t=10ms

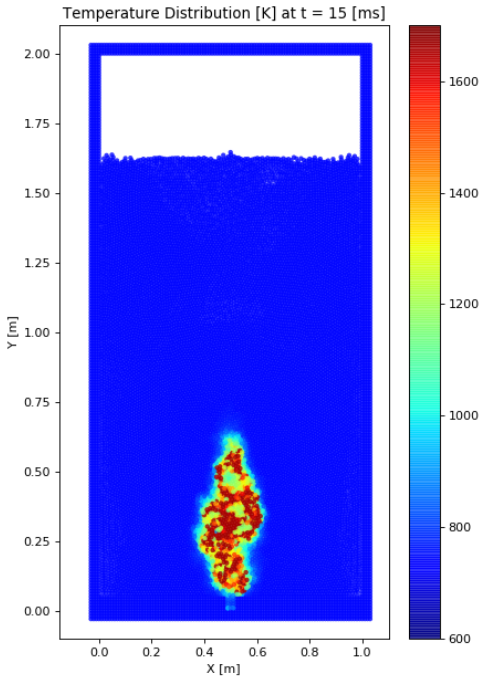

(d) t=15ms

Figure 4.9 – Temperature Profile at 1, 5, 10 and 15 ms

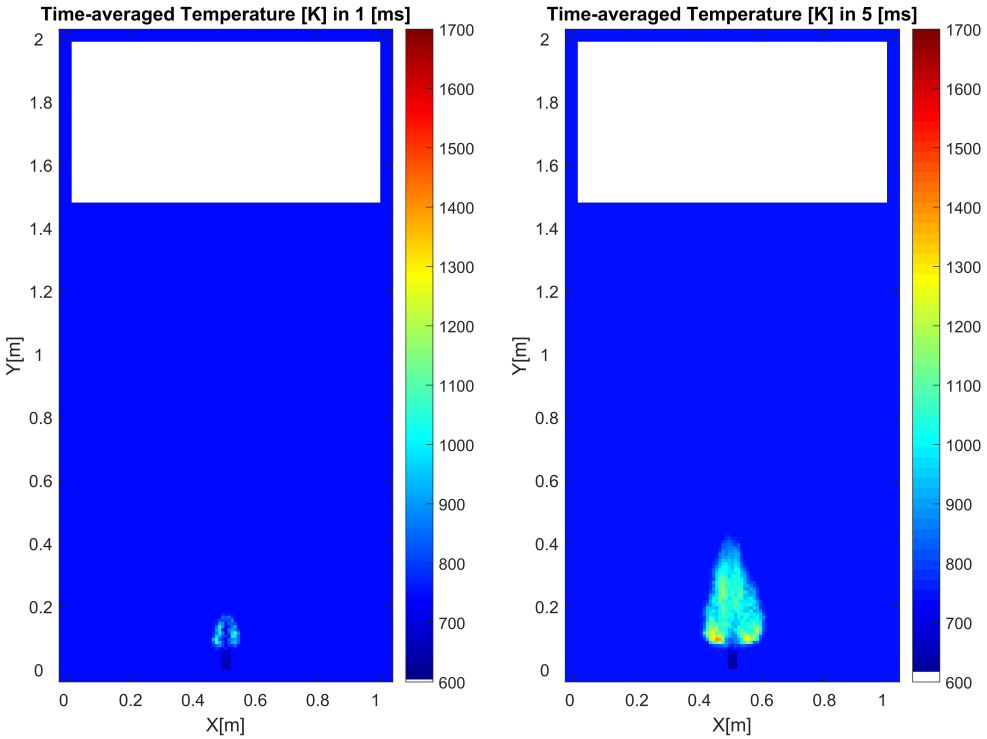

(a) 0-1ms

(b) 0-5ms

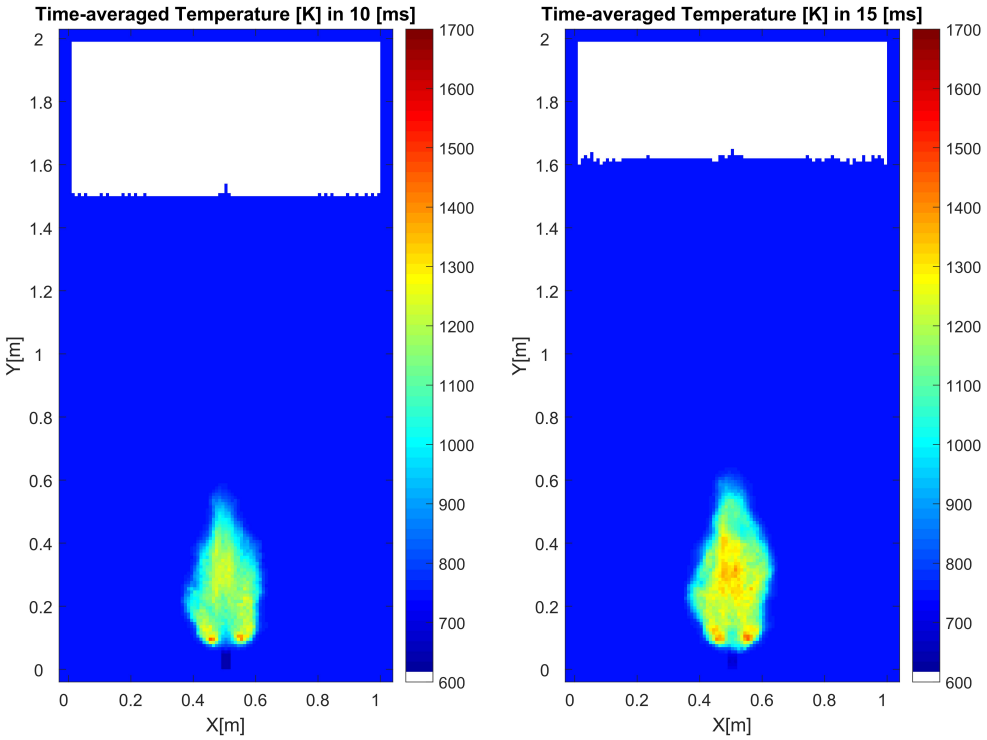

(c) 0-10ms

(d) 0-15ms

Figure 4.10 – Time-averaged temperature profile in 1, 5, 10 and 15ms

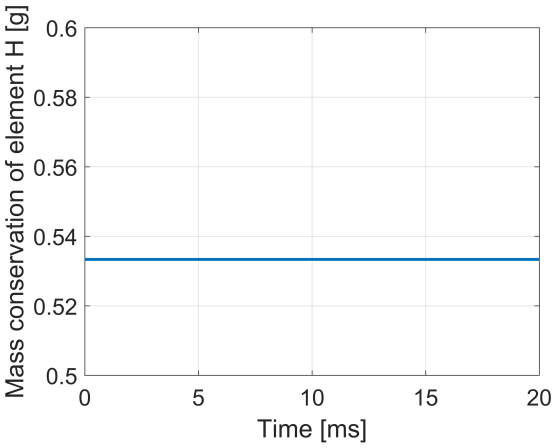

(a) H

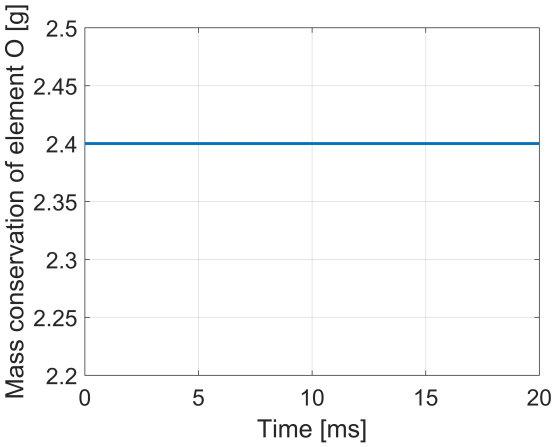

(b) O

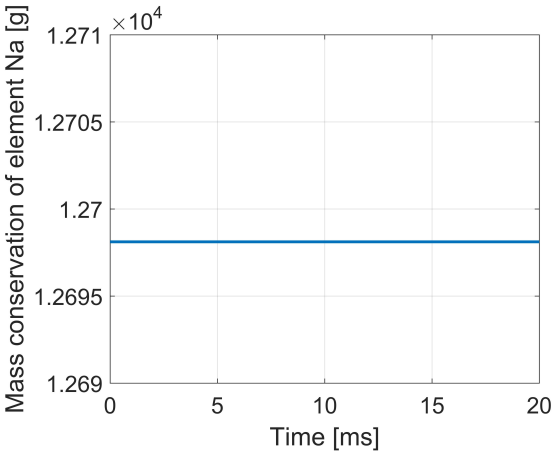

(c) Na

Figure 4.11 – Mass conservation of element H, O and Na

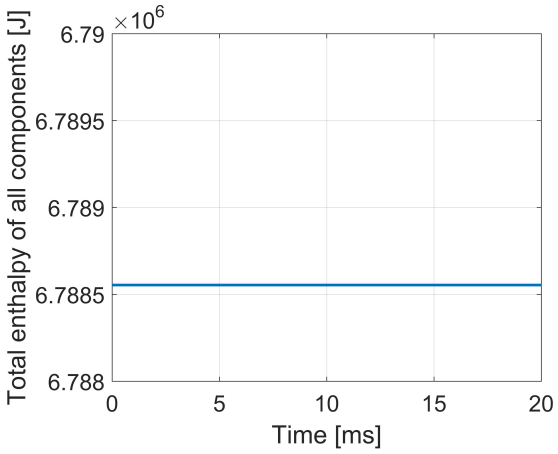

Figure 4.12 – Enthalpy conservation over 20ms

5 Application in Configuration with Tube Bundles

In the former chapter, simulations of sodium-water chemical reaction are conducted without the interference of heat-exchanger tubes. Heat exchanger tubes are equipped in the steam generator for the aim of cooling the sodium coolant which brings out the heat from the reactor core, and heating up the pressurised water for the usage in the second loop. The configuration of tube bundles in the steam generator has the influence on the flowing trajectory of leaked steam jet and the propagation of chemical reaction zones, given a leakage incident of steam jet in the steam generator.

The breach of the failed tube can occur at any location and the jet leakage has the possibility to be injected in the steam generator at all directions. Therefore, the most adjacent target tube depends on the location of the breach and the direction of steam jet. It is of great importance to estimate the evolution of reaction zones in the steam generator once an incident takes place or to locate the failed tube and the breach by monitoring the reaction zones.

For the validation of the study of this thesis, configurations including tube bundles are used for the investigation of simulation results under the influence of complex conditions. This chapter starts with an investigation on simulations with a single tube and discuss the impact of a single target tube on the development of reaction zones. In the second section, investigation on the effect of sub-channels between tubes will be conducted by applying multiple tubes in the same configuration of models presented in the former chapter. For a further application and validation, a full-scale model of steam generator with 95 tubes is constructed for comparing the simulation results to the ones calculated by using SERAPHIM. Reasonable and similar phenomena of the reaction reflected from the results will be presented and explained in this chapter.

By utilising more practical configurations for simulations, the modelling methodology can be somehow validated by obtaining the similar phenomena as the observation in experiments and incidents.

5.1 Simulation with a Single Tube

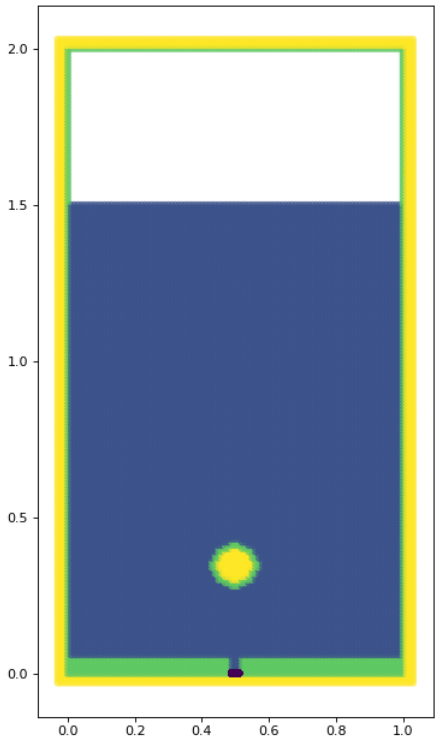

Figure 5.1 – Model configuration with a single tube

Table 5.1 – Geometric dimensions and initial conditions for simulation cases.

Geometric Dimensions		Initial Conditions	
Items	Value	Items	Value
Particle diameter	0.01 m	Steam velocity	X: 0 m/s, Y: 10 m/s
Inner width of sodium tank	1.01 m	Steam density	2.0 kg/m^3
Height of liquid sodium	1.50 m	Sodium density	896.0 kg/m^3
Thickness of simulation domain	0.01 m	Temperature of steam	641 K
Breach width	0.03m	Temperature of liquid sodium	742 K

Firstly, a single tube inside the model will be investigated for the aim of investigating the thermo-hydraulic impact by the change of the structure. The same simulation conditions as in the previous chapter are adopted. Comparison of simulation results before and after the inclusion of a single tube will be conducted.

As illustrated in Fig. 5.1, a tube configuration is set up in the model and surrounded by the liquid sodium. The geometry and initial conditions are listed in Table. 4.1, which are almost the same as the condition used in Chapter 4 except the initial velocity. The steam jet starts from the same location as in the previous models. The tube diameter is about the size of 16 times of particle diameters. For the simplification of investigation, the heat conduction between particles and tube wall are not considered.

With regard to the initial conditions, water vapor jet with a width of 3 particle diameters and an initial velocity of 10 m/s is injected into the liquid sodium side.

Fig. 5.2 shows the transient temperature of each particle at 10ms and 20ms respectively. In the first 20ms, Fig. 5.2 presents a relatively symmetric temperature distribution when the front of water vapor does not have a direct contact with the target tube wall.

However, with the simulation going on and the approach of water vapor to the target tube wall, the temperature profile at 40 ms and 60 ms starts becoming asymmetric, which is due to the disturbance escalation of flow jet. If the momentum is conserved, the total momentum may have values on either the left or right horizontal direction. Given the front lighter particles situated slightly on the left side, the sequential water vapor particles will moving towards the left side due to the less inertia of lighter density particles compared to heavier sodium particles. In consequence, a short flow jet will move towards to the left side.

Concerning the distribution of reactant and products, water vapor and hydrogen are selected for the investigation and plotted in Fig. 5.3, and Fig. 5.4 respectively. Consistent phenomena and features of distribution can be observed.

5.2 Simulation with Multiple Tube Bundles

As a difference from the first section, this section is mainly focusing on the study of the influence from the gaps between tubes. The vertical arrangement of tubes is shown in Fig. 5.5. This configuration contains 21 tubes, each of which has a diameter as long as 16 particle diameters.

The initial simulation condition is set as the same as the previous section that an initially vertical velocity of 10m/s is assigned to injected particles.

In Fig. 5.6, transient temperature values of each fluid particle have been plotted with respect to the simulation at 10, 20, 30 and 50 ms, respectively.

As indicated from the above figures showing the temperature profiles, the transient temperature for particles are lower than 1500 K, which is lower than the boiling point of NaOH. Therefore, it can be observed later that the evaporation of NaOH does not take place within 50 ms but only occurs in a very short period after 50ms.

Furthermore, under the influence of multiple tubes, the heigh temperature region is mainly distributed around the tube walls. Because there is no heat conduction considered in this model from particles to tube walls, the temperature of interfacial water vapor particles will decrease due to the heat conduction with liquid sodium.

Time-averaged particle temperature is calculated for estimating the accumulating impact of temperature distribution in terms of a longer period, which is plotted in Fig. 5.7. Since the temperature is averaged from the beginning of injection to the selected time step, the time-averaged particle temperature profile is dependent on the local evolution from the start of the simulation. The initial temperature of all particles is definitely lower than the ones after chemical reaction takes place. Thus, the time-averaged particle temperature is reasonably smaller than the transient values.

Fig. 5.8 plots the molar evolution of six species within 60 ms. As explained that the transient temperature is lower than the boiling point of NaOH, almost no NaOH vapor is generated along the period of 60 ms. The evolution of sodium vapor oscillates a few times indicating the change of dominance process between evaporation and condensation.

The total enthalpy evolution for each species is presented in Fig. 5.9. Investigation of mass and enthalpy conservation is plotted in Fig. 5.10, where flat evolution indicates the converged mass and enthalpy are achieved. Transient and time-averaged molar amount of water vapor are plotted in Fig. 5.11 and Fig. 5.12, respectively. The transient mole amount of hydrogen at 4 timestamps is plotted in Fig. 5.13. Based on the result of molar amount of each gaseous species, volume fraction of gaseous species in the gaseous particles can be calculated and presented in Fig. 5.12. By comparing the hydrogen volume fraction distribution to the transient temperature distribution, one can note the in a short time period, the location with higher hydrogen concentration normally is observed with higher temperature. Because in a short period time, the hydrogen volume fraction is just around 50% which means there is still a large amount of water vapor inside the particle. The reaction heat releasing rate has not been reduced to be lower than the heat transfer rate, which indicates a continuous increment of temperature. For a longer simulation with hydrogen volume fracton larger than 80%, the phenomena can be inversely observed.

5.3 Simulation in a Full-Scale Steam Generator

This section presents the investigation of sodium-water chemical reaction in a full steam generator model with multiple tube bundles. As mentioned in the introduction, SERAPHIM is a numerical code used for simulating sodium-water chemical reaction with sufficient validation by experiments. Therefore, the simulation results obtained from the present method are compared to the ones calculated in SERAPHIM with the similar configuration and conditions for the sake of validation. Due to some limitation of the present method, setting the exactly same boundary conditions with SERAPHIM is very difficult. Therefore, some boundary conditions will be varied and a discussion on this variation will be presented later.

The full model used in MPS simulations has 95 tubes with a ruptured tube shown in Fig. 5.18, where water vapor is injected vertically into the liquid sodium side. The gravitational force direction is set with a rightwards rotation of 23 degree with respect to its originally vertical direction as the gravity arrow shows in Fig. 5.18. Water vapor is discharged from the nozzle inside the ruptured tube with a depth of 3 particle diameters. It is for the sake of the stability of calculation to force injected particles to have constantly initial velocities before entering into the sodium side. All four sides of the configuration are constructed with particle walls as free slip boundaries except an exit with a free surface on the top left corner. It differs from the boundary conditions used in SERAPHIM simulations. Constant pressure is set on the horizontal top and bottom sides, while free slip boundaries are set on the left and right sides in the SERAPHIM case.

Initial conditions are tabulated in the Table. 5.2. Two particles per row are arranged in the nozzle and kept with a diameter of 0.004m. To approach to a long simulation period, a large amount of particles have to be injected into the sodium side. For the sake of the completion of simulation by limited computational sources, the number of particles to be injected is expected to be as small as possible by means of adopting a large particle diameter. Likewise, the time step is expected to be sufficiently large while ensuring the computing stability and convergence of solutions. Based on this consideration, a low discharging velocity of 1.0 m/s is applied in this validation case. Though some physical phenomena may be neglected by using large diameter and time steps such as turbulence and surface tension, the main concern in this simulation is to have an overview of the reaction on the large scale of a full steam generator. Therefore, the initial conditions in this case are applicable to investigate the overall temperature distribution and particle propagation among tube gaps.

Table 5.2 – Initial conditions for an integrated simulation with 95 tubes.

Initial conditions	MPS	SERAPHIM
Particle diameter	0.004 m	-
Breach width	0.008 m	0.008m
Initial Velocity.	1.0 m/s	1.0 m/s
Water Vapor Temperature	641K	620 K
Water Vapor Density	2.0 kg/m^3	0.52 kg/m^3
Sodium Temperature	742K	732 K
Sodium Density	896.0 kg/m^3	896.0 kg/m^3
Initial time step	1e-4 s	-
Simulation period	2.0 s	2.0 s

5.4 Comparison to SERAPHIM Results

To start with, the absolute velocity distribution of gaseous particles is investigated and averaged in 1.0-2.0s, which is plotted in Fig. 5.19. As one can notice, the flow trajectory of gaseous

particles is mainly distributed among the tube gaps along the inversely gravitational direction induced by the bouyancy. In addition to the channel where the main trajectory locates, some of gaseous particles spread to neighbouring tube channels. The right channel with respect to the main one is occupied by wall particles at its end near the free surface, which depresses the upwards movements of gaseous particles. Therefore, it can be observed particle trajectory is much denser in the left channel than that in the right one. The averaged speed for most gaseous particles ranges in 0-2.0 m/s and it becomes smaller when approaching to the free surface. Because gaseous particles have a tendency to spread near the free surface, they get surrounded by more liquid particles with larger viscosity values. In consequence, the velocity value is depressed by the increasing viscosity impact.

For the sake of validation of the results from MPS, simulation results performed in SERAPHIM by Dr. A. Uchibori [30] are used for the comparison.

The time-averaged gas phase velocity profile from SERAPHIM during 1.0-2.0s is plotted on Fig. 5.20. The averaged velocity ranges from 0 to 2.5m/s, which is slightly larger than the result in MPS. It is because of the gaseous particles contain liquid species in the particle methods. Meanwhile, a larger density of 2 kg/m^3 is used in MPS cases compared to the density about 0.53 kg/m^3 used in SERAPHIM. In fact, SERAPHIM uses the initial condition of constant pressure and temperature to calculate the density. The jet trajectory in both methods has a good agreement as well.

Fig. 5.21 present the time and mass averaged temperature of both gaseous and liquid particles, which almost has no large difference from the results averaged by enthalpy. It is noted that the temperature mitigates along the distance far away from the breach. Generally, the temperature distribution is lower than 700 ^oC except some locations with extreme values around 800 ^oC. It is because no liquid sodium particles pass through the corresponding grid. In this simulation, the grid size is the same as the particle diameter which results in gaseous particles keep occupying the same grid without liquid particles moving in.

The time-averaged temperature from SERAPHIM results presented in Fig. 5.22 has the similar phenomenon that maximum temperature appear in a short range from the breach. As mentioned, the heat conductivity between gas and liquid phase used in SERAPHIM is tens of time larger than the value used in MPS. The heat transfer from gaseous particles to liquid sodium particles in MPS is not as fast as in SERAPHIM, which results in higher temperature observed in MPS simulation. Furthermore, SERAPHIM considers modelling the compressibility of gas phase. The heat dissipation by volume expansion can also be expected, which reduces the local temperature as well. Finally, the density of water vapor used in MPS is around 4 times larger than in SERAPHIM. The reaction rate is expected to be larger in the MPS case. After the same period of heat conduction, the remaining heat is much larger in MPS cases as well. The above explanations can account for the observation of higher temperature in MPS results.

Fig. 5.21 shows the time and mass averaged temperature of gaseous particles during 1.0-2.0s. The mass averaged value is calculated by the mass fraction multiplied by the temperature

values of gaseous and liquid particles. One can notice the maximum temperature about 800 ^oC around the first target tube and then the temperature is moderated sharply around the second target tube along the trajectory channel. As mentioned in the section of governing equations, the energy for gas expansion is not considered in this work, which will definitely induce higher temperature in this simulation than the realistic phenomena.

The distribution of NaOH concentration in MPS and SERAPHIM results are plotted in Fig. 5.23 and Fig. 5.24, respectively. The NaOH concentration is about twice larger than SERAPHIM results because the density used in MPS is around 4 times larger. NaOH is more spreading in MPS rather than being concentrated beside tube walls observed in SERAPHIM. It is because that the particle size is much larger than the mesh size used in SERAPHIM, which accounts for the spreading observation. The order of the magnitude and distribution of the NaOH concentrations shows the acceptable consistency in the two methods.

The time-averaged volume fraction of H_2O in gaseous particles from MPS is presented in Fig. 5.27, while the time-averaged volume fraction profile of H_2O from SERAPHIM calculation is plotted in Fig. 5.26. With the initial velocity of 1 m/s injection, the water vapor is consumed immediately after discharged into the sodium side. It accounts for the zero volume fraction of water vapor observed in SERAPHIM results. The results obtained from MPS also has the similar observation that except the small region around the breach, water vapor is exhausted completely. For the region around the breach, it can be understood that a larger water vapor density used in MPS results in insufficient consumption near the exit.

The time-averaged volume fraction profile of H_2 in gaseous particles are shown in the Fig. 5.27, while the volume fraction of H_2 from SERAPHIM shown in Fig. 5.28. There is also consistency on H_2 distribution in both methods. The volume fraction is the same as 1.0 after the first target tube. Around the first target tube, because the underestimated heat transfer, sodium evaporation occurs in MPS simulations. Though H_2 distribution is much wider in SERAPHIM, at the same location the void fraction presented in Fig. 5.29 from SERAPHIM is almost 0, which actually indicates little amount of hydrogen concentration. In MPS method, because H_2 is constrained inside the particle and particle size is much larger, such phenomena can not be reproduced.

Though some differences are observed in the above figures which are induced by the different modelling and initial conditions in MPS, the main characteristic of the results from both methods can be noticed. It indicates the validity of the developed MPS method for simulating the sodium-water reaction.

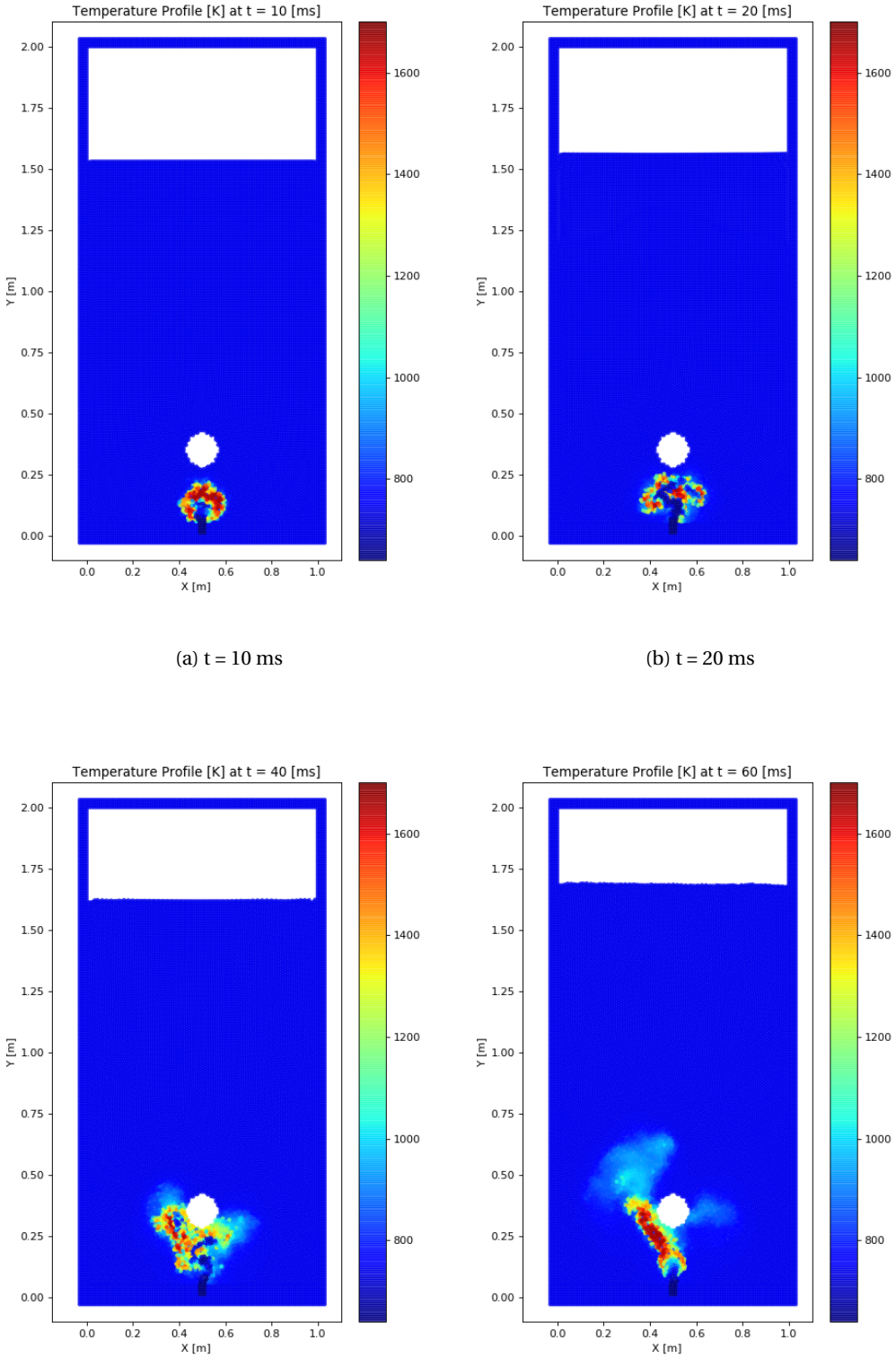

(a) t = 10 ms

(b) t = 20 ms

(c) t = 40 ms

(d) t = 60 ms

Figure 5.2 – Transient temperature profile

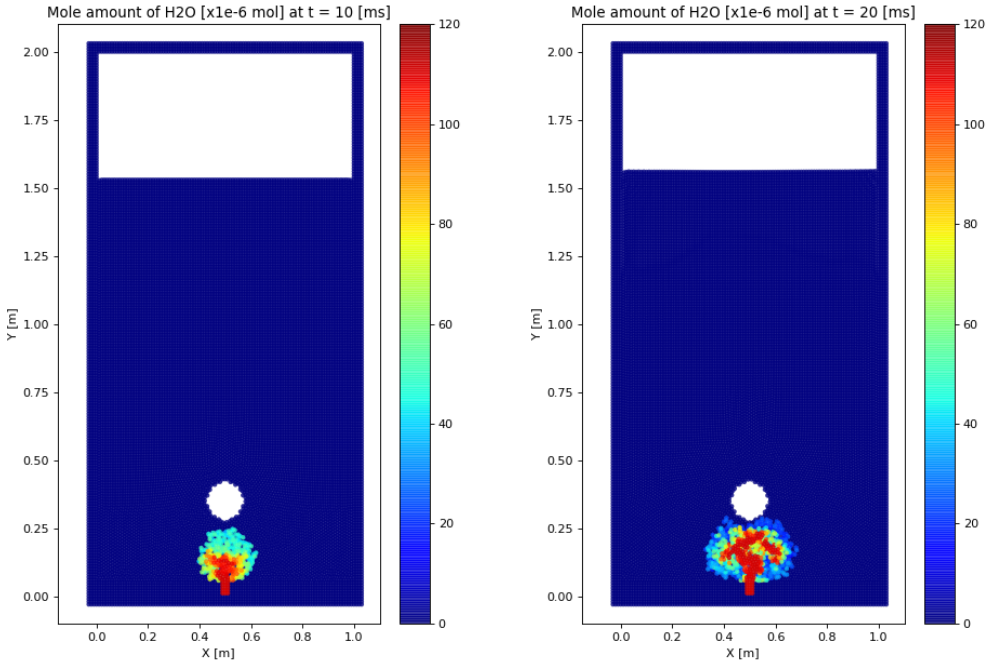

(a) t = 10 ms

(b) t = 20 ms

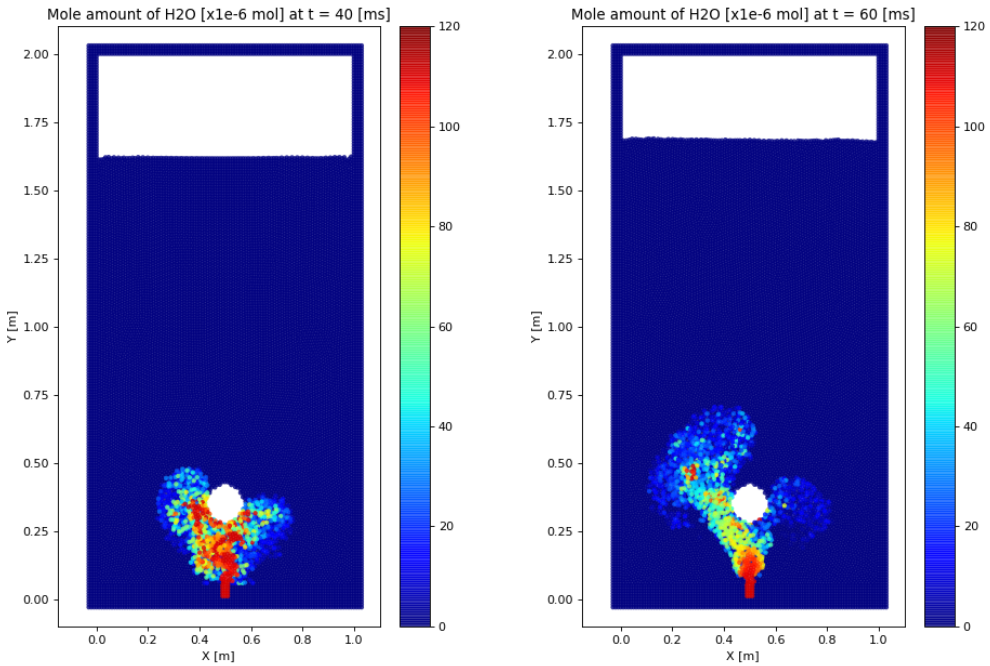

(c) t = 40 ms

(d) t = 60 ms

Figure 5.3 – Mole amount distribution of H_2O vapor at 10, 20, 40 and 60 ms

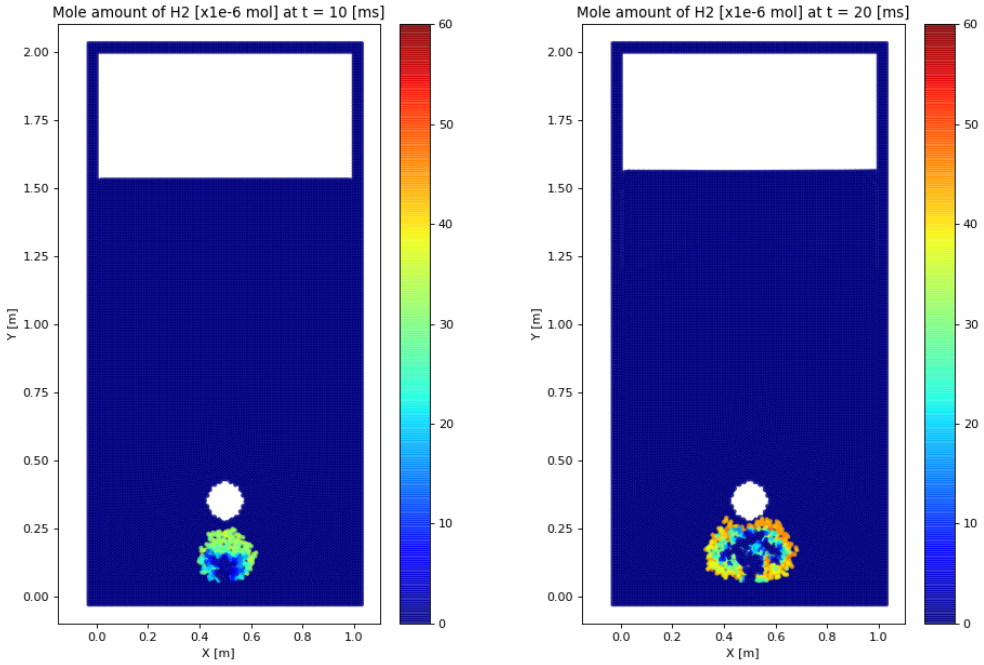

(a) t = 10 ms

(b) t = 20 ms

(c) t = 40 ms

(d) t = 60 ms

Figure 5.4 – Mole amount distribution of H_2 at 10, 20, 40 and 60 ms

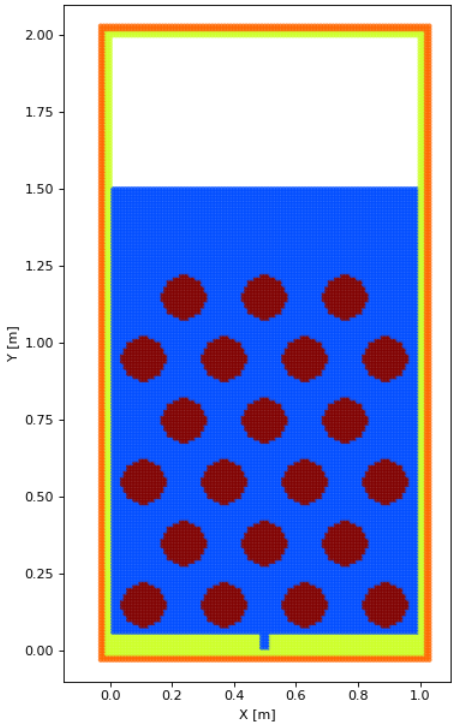

Figure 5.5 – Model configuration with 21 tubes

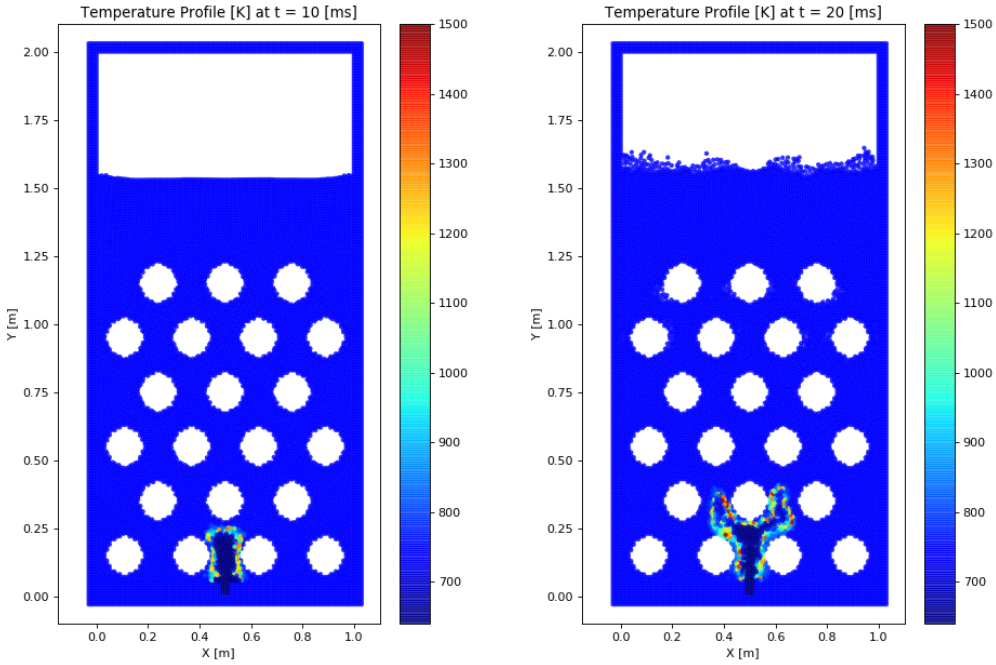

(a) t = 10 ms

(b) t = 20 ms

(c) t = 30 ms

(d) t = 50 ms

Figure 5.6 – Transient temperature profile

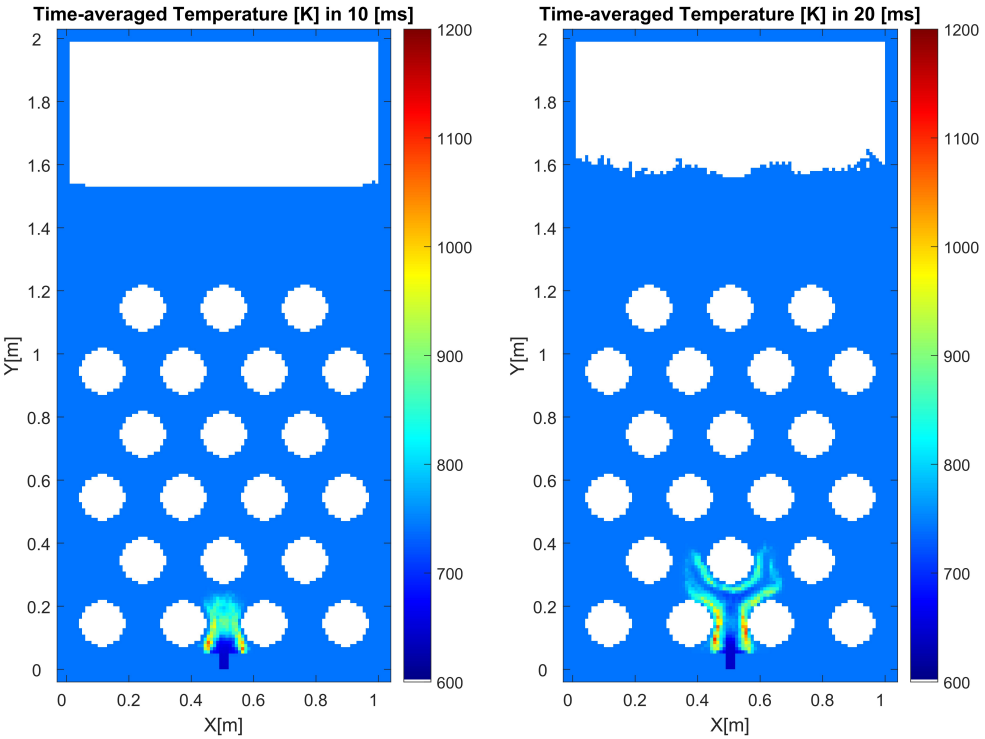

(a) t = 10 ms

(b) t = 20 ms

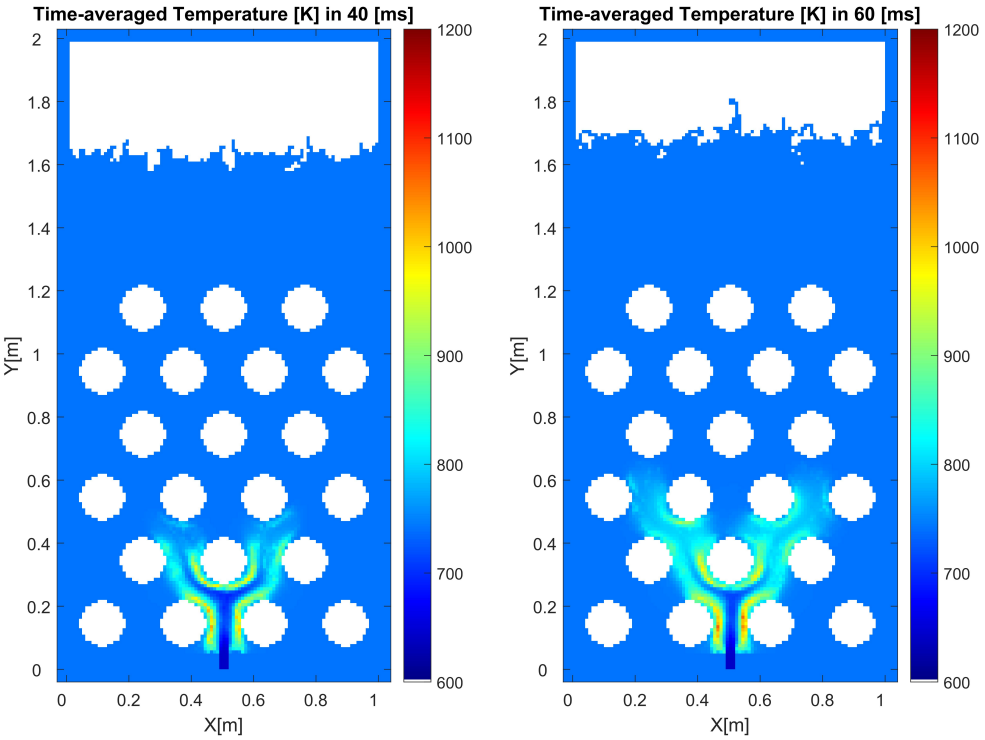

(c) t = 40 ms

(d) t = 60 ms

Figure 5.7 – Time-averaged temperature profile within 10 and 20ms respectively

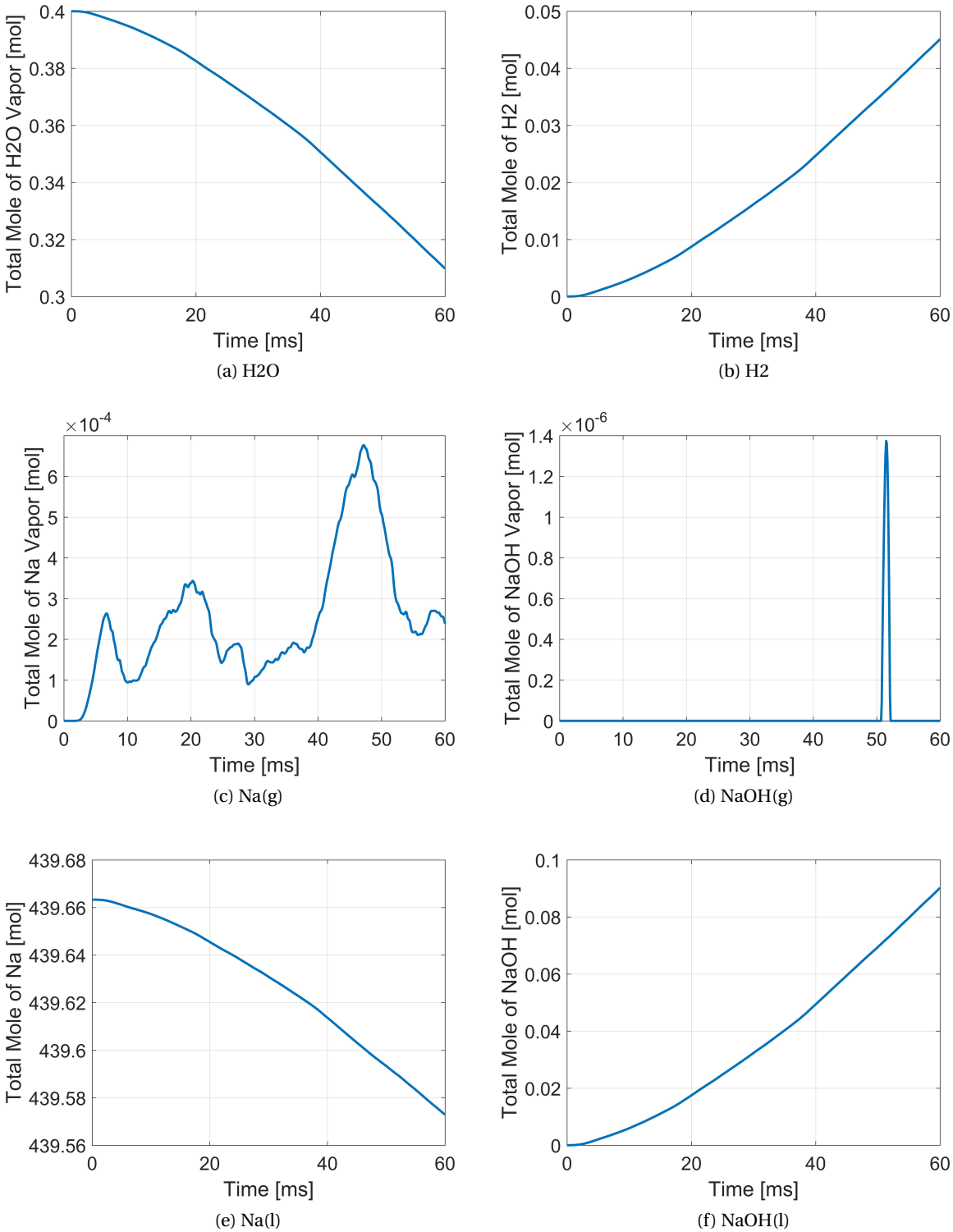

(a) H2O (b) H2

(c) Na(g) (d) NaOH(g)

(e) Na(l) (f) NaOH(l)

Figure 5.8 – Molar evolution of six species within 60 ms.

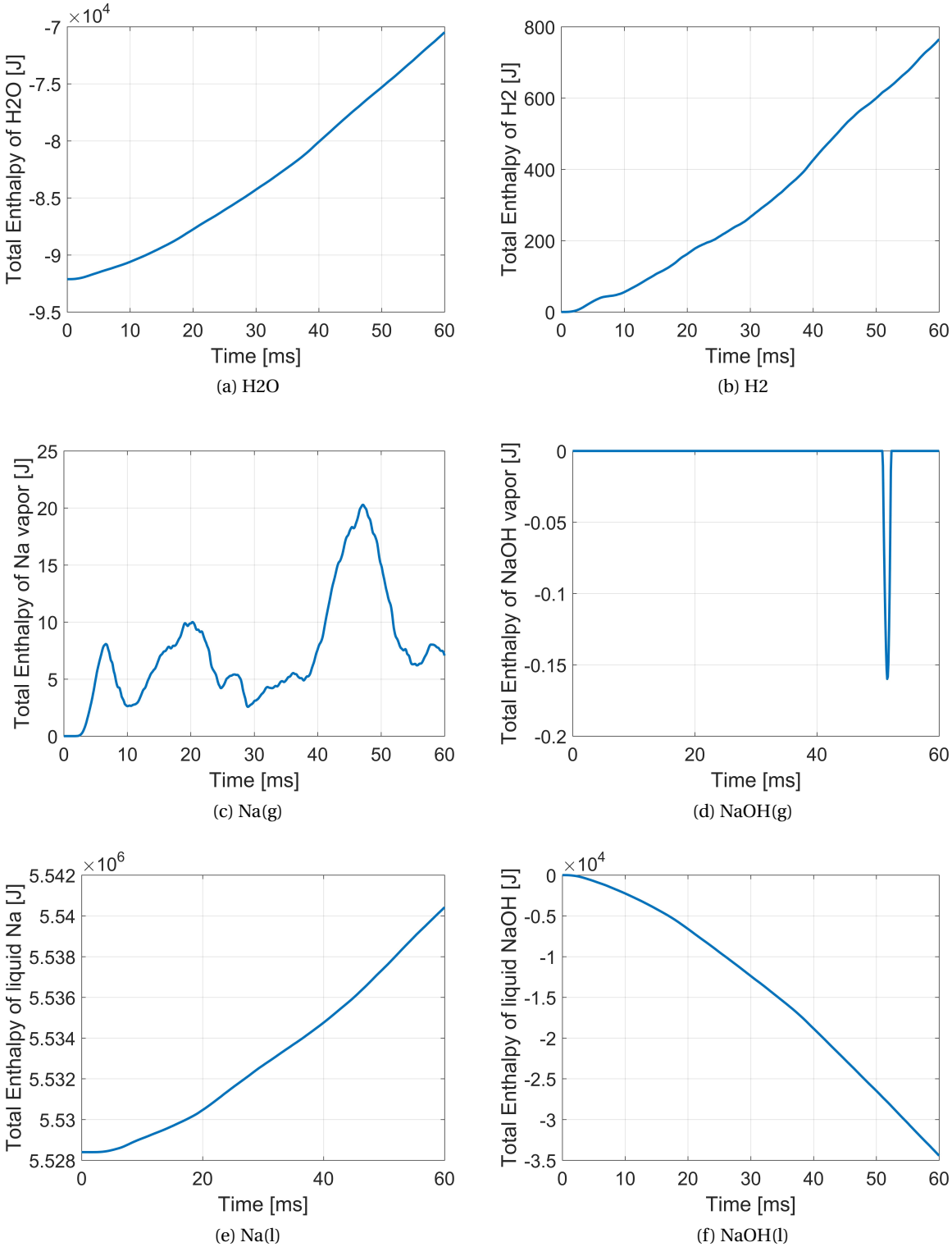

(a) H2O (b) H2

(c) Na(g) (d) NaOH(g)

(e) Na(l) (f) NaOH(l)

Figure 5.9 – Enthalpy evolution of six species within 60 ms.

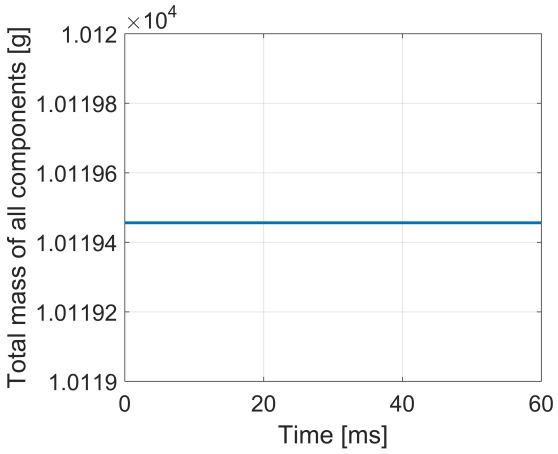

(a) Mass conservation

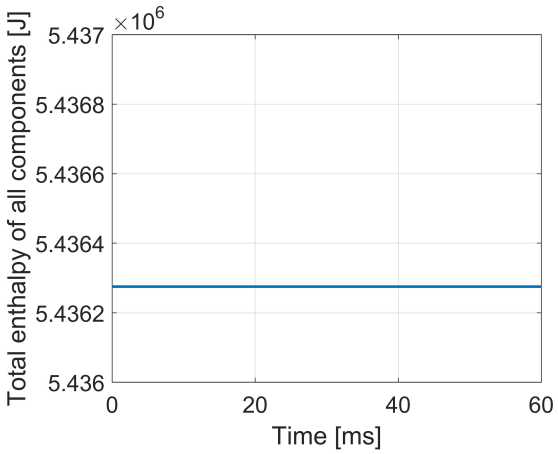

(b) Enthalpy conservation

Figure 5.10 – Conservation of mass and enthalpy within 60ms

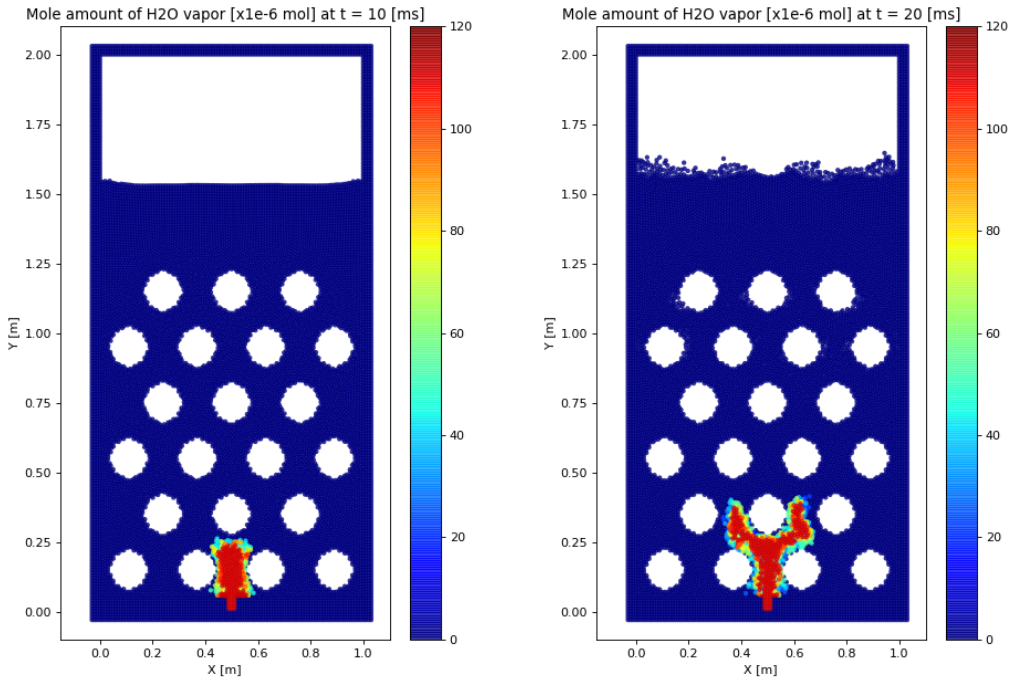

(a) t = 10 ms

(b) t = 20 ms

(c) t = 40 ms

(d) t = 60 ms

Figure 5.11 – Mole amount distribution of H_2O vapor at 10, 20, 40 and 60 ms

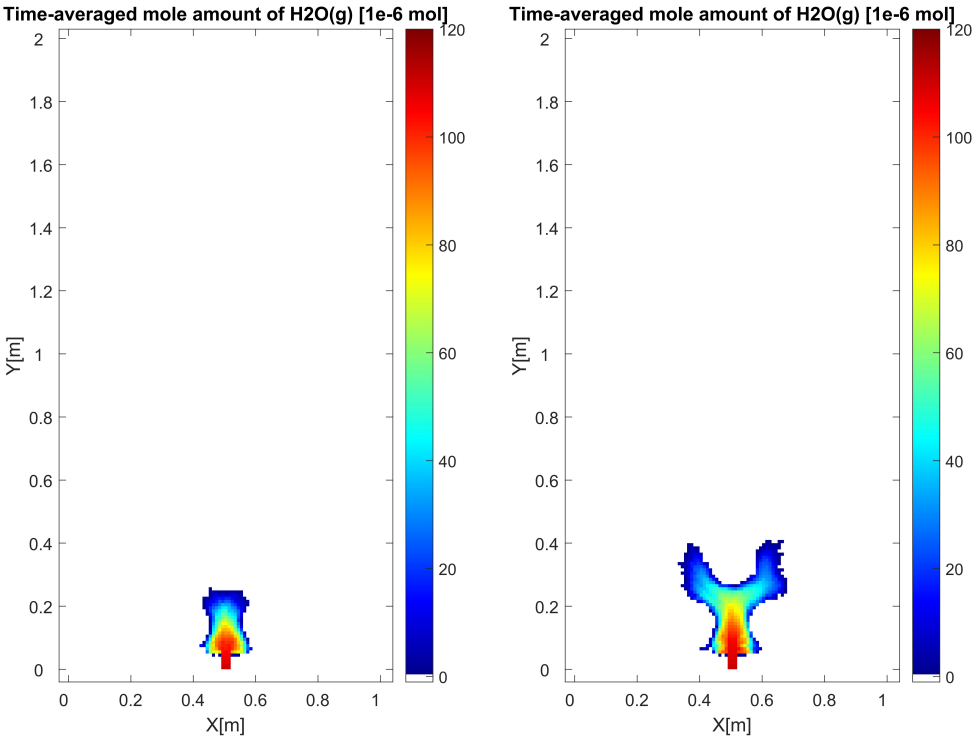

(a) 0 - 10 ms

(b) 0 - 20 ms

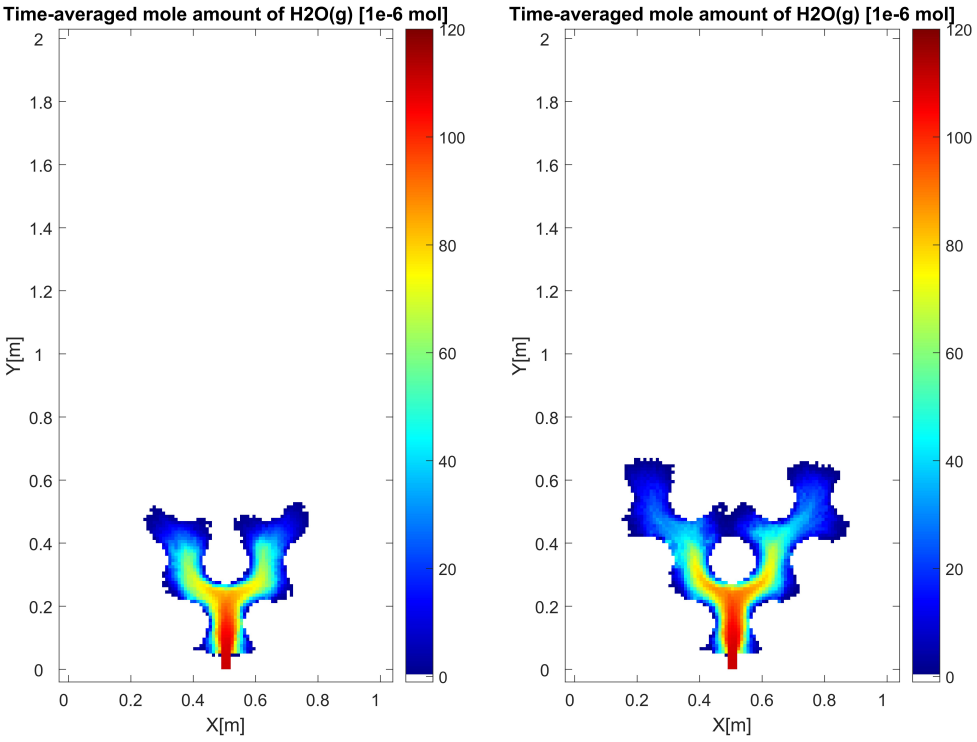

(c) 0 - 40 ms

(d) 0 - 60 ms

Figure 5.12 – Time-averaged mole amount of H_2O vapor within 10, 20, 40 and 60 ms

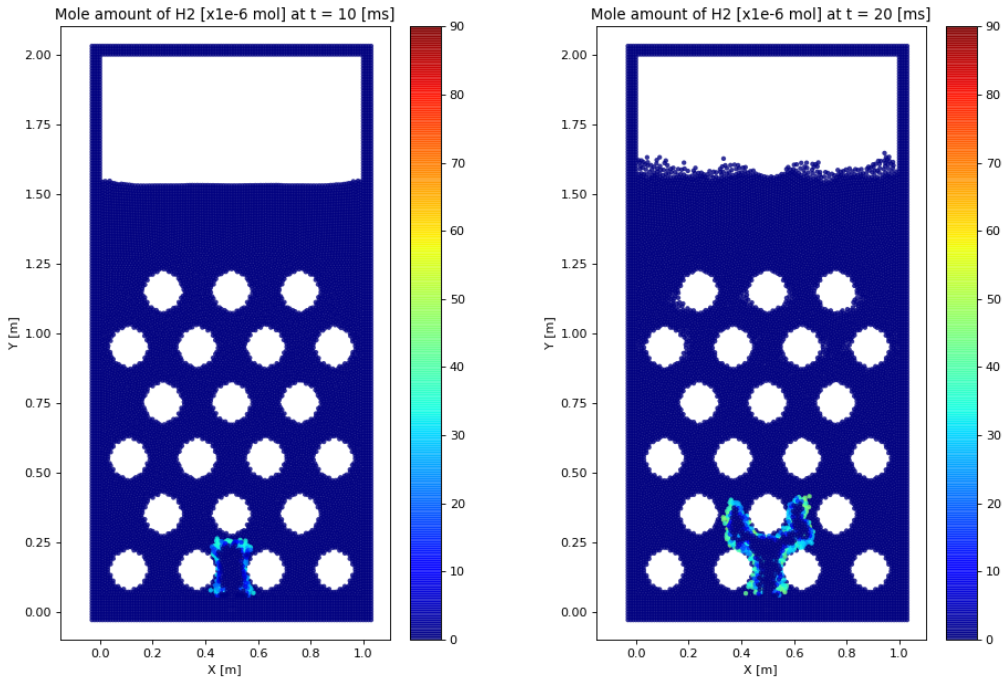

(a) t = 10 ms

(b) t = 20 ms

(c) t = 40 ms

(d) t = 60 ms

Figure 5.13 – Mole amount distribution of H_2 at 10, 20, 40 and 60 ms

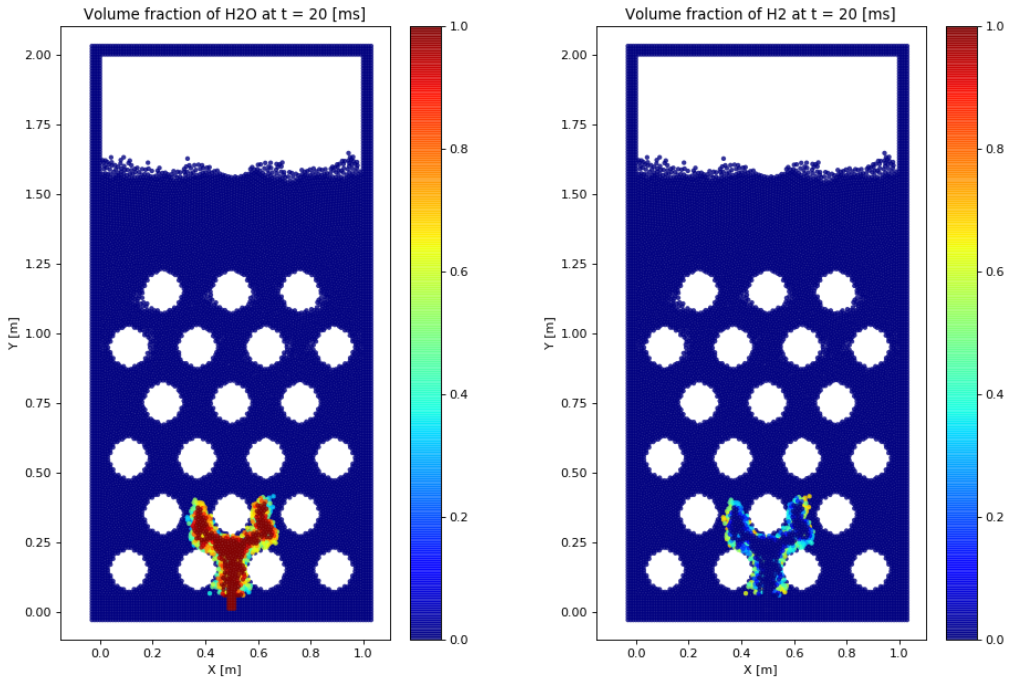

(a) H2O at 20ms

(b) H2 at 20ms

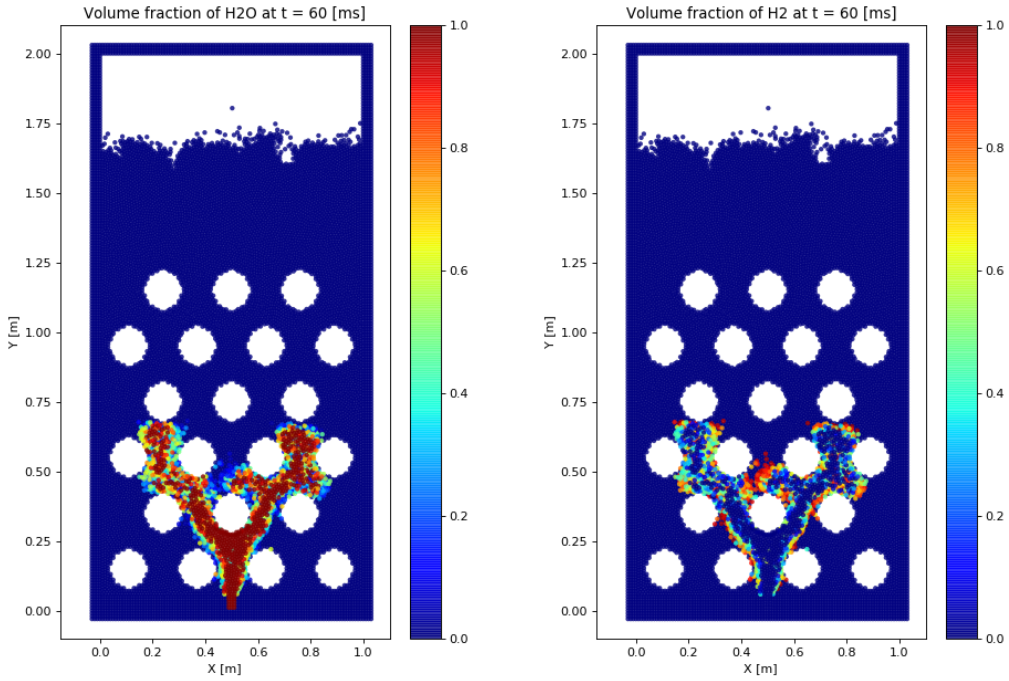

(c) H20 at 60ms

(d) H2 at 60ms

Figure 5.14 – Volume fraction of $H2O$ and H_2 at 20ms

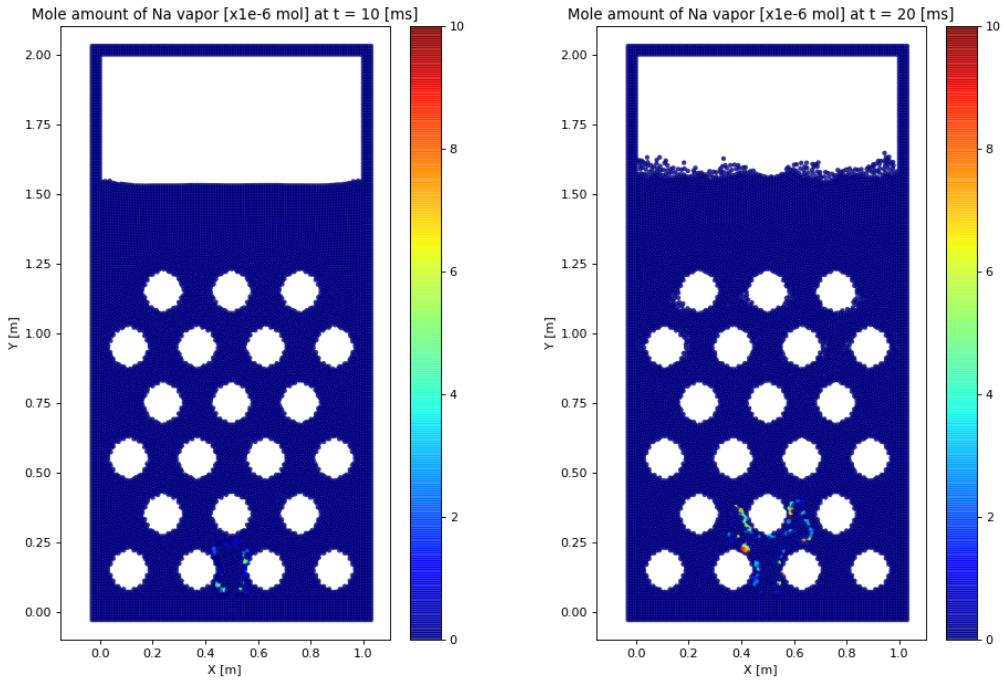

(a) t = 10 ms

(b) t = 20 ms

(c) t = 40 ms

(d) t = 20 ms

Figure 5.15 – Mole amount distribution of Na vapor at 10, 20, 40 and 60 ms

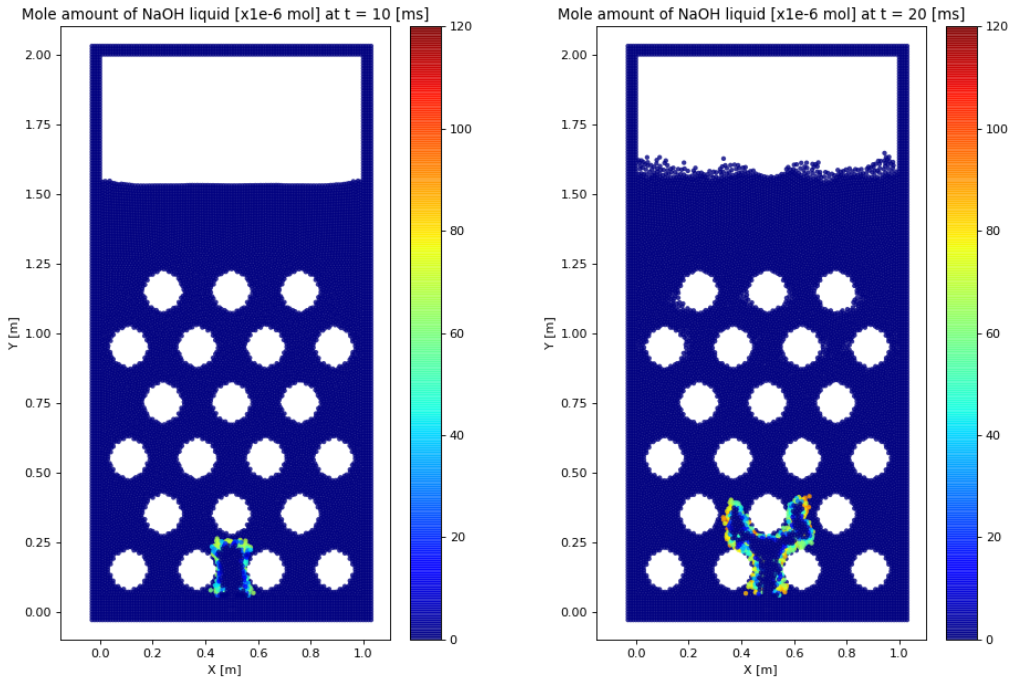

(a) t = 10 ms

(b) t = 20 ms

(c) t = 40 ms

(d) t = 20 ms

Figure 5.16 – Mole amount distribution of $NaOH$ liquid at 10, 20, 40 and 60 ms

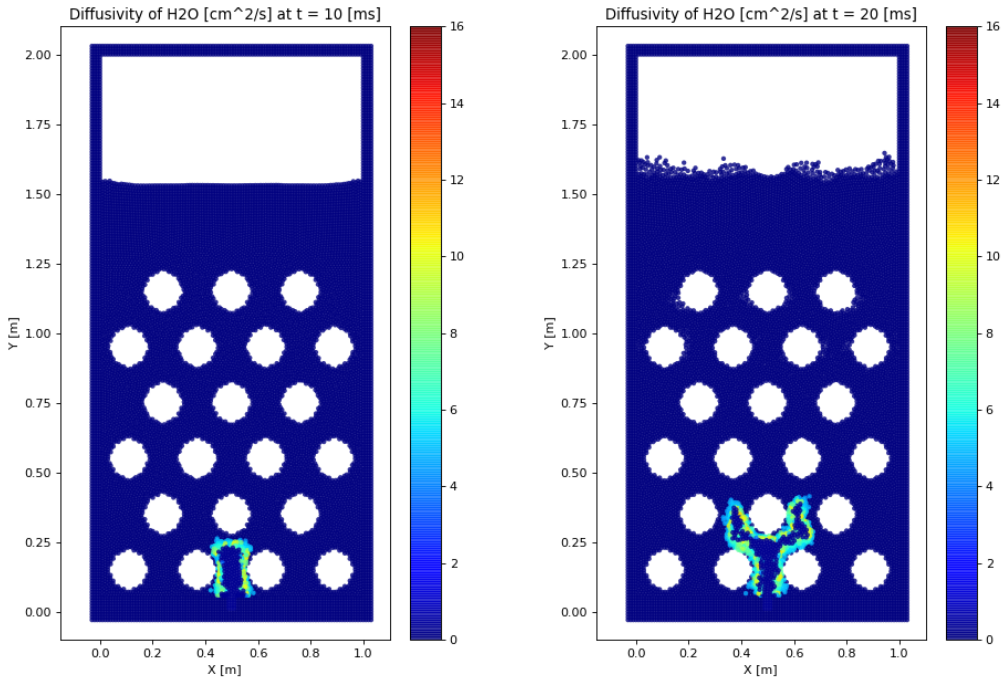

(a) t = 10 ms

(b) t = 20 ms

(c) t = 40 ms

(d) t = 60 ms

Figure 5.17 – Diffusion coefficient of H_2O among gaseous particles at 10, 20, 40 and 60 ms.

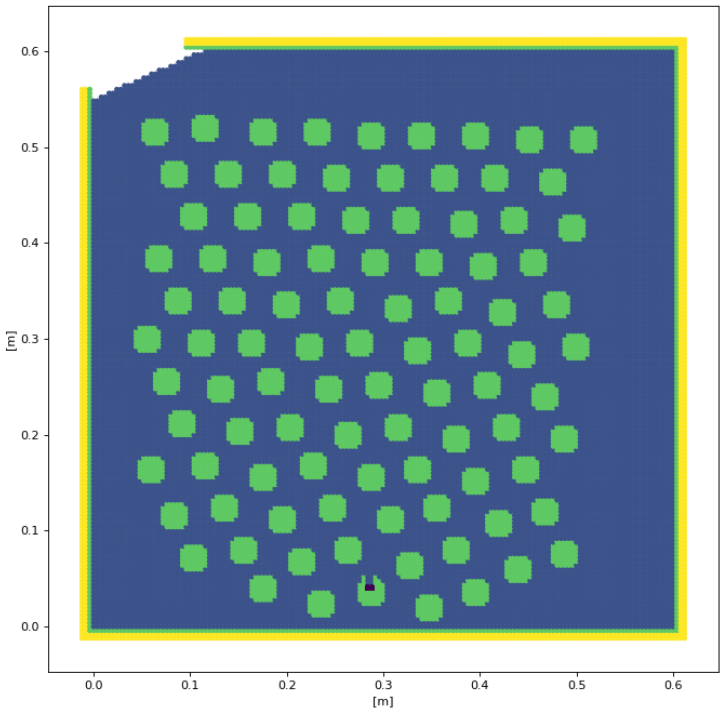

Figure 5.18 – Model configuration of a full-scale steam generator

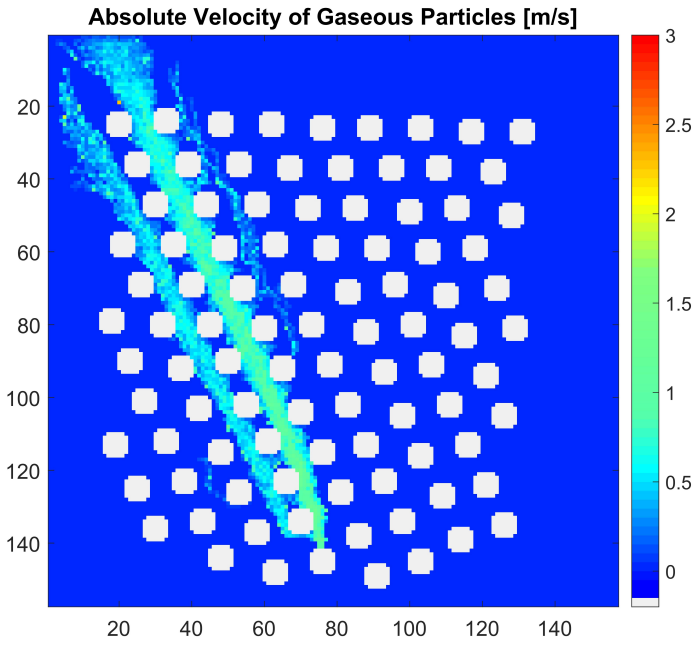

Figure 5.19 – Time-averaged absolute velocity in [m/s] of gaseous particles from MPS during 1.0-2.0s

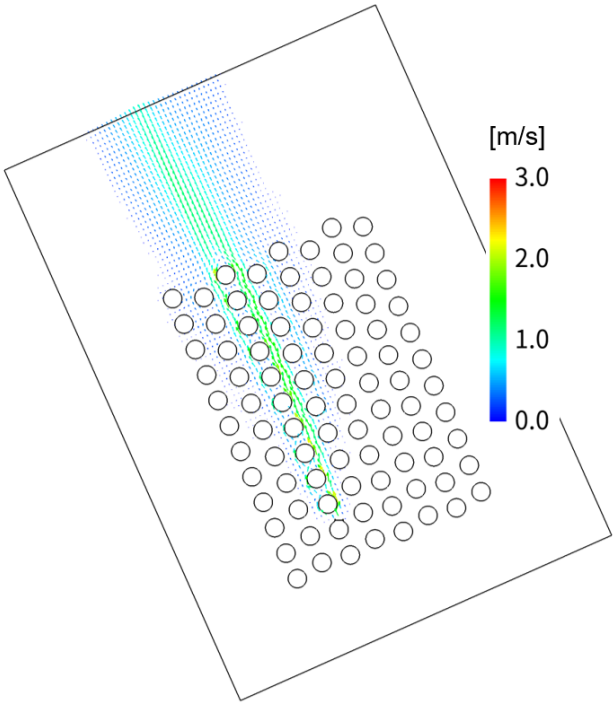

Figure 5.20 – Time-averaged gas phase velocity from SERAPHIM during 1.0-2.0s[30]

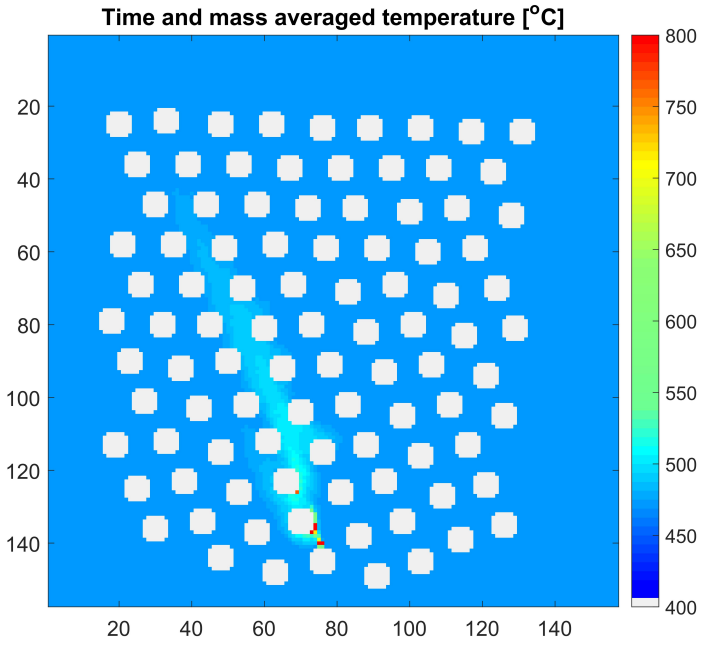

Figure 5.21 – Time and mass averaged temperature in $[^oC]$ from MPS during 1.0-2.0s

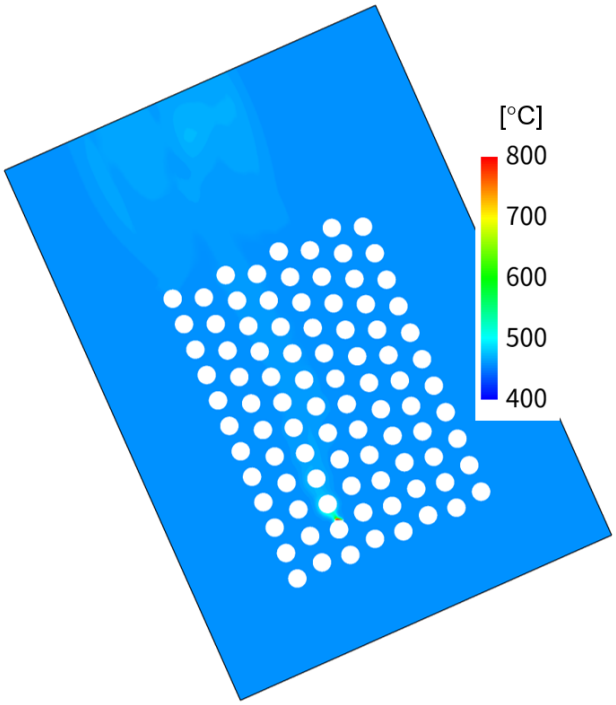

Figure 5.22 – Time-averaged mass-averaged temperature from SERAPHIM during 1.0-2.0s[30]

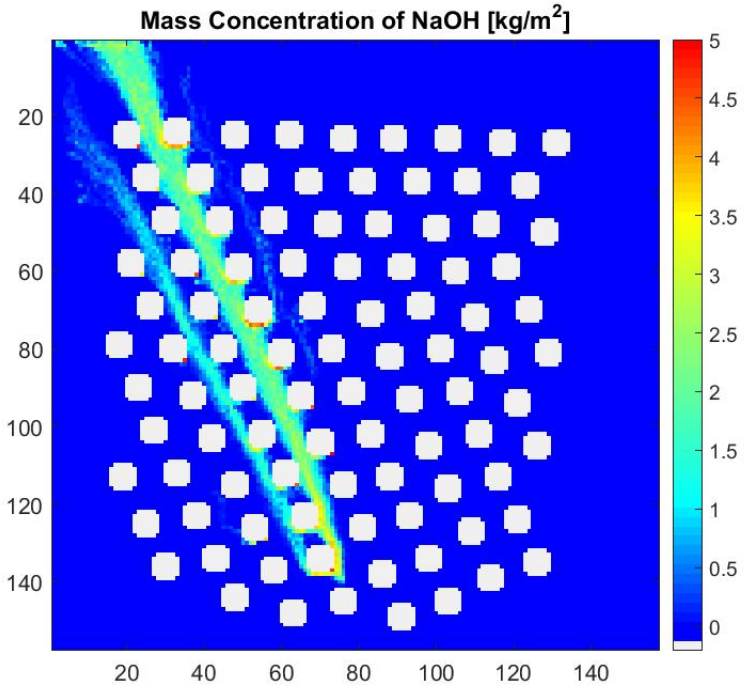

Figure 5.23 – Time-averaged mole amount of NaOH in [mol] in gaseous particles from MPS during 1.0-2.0s

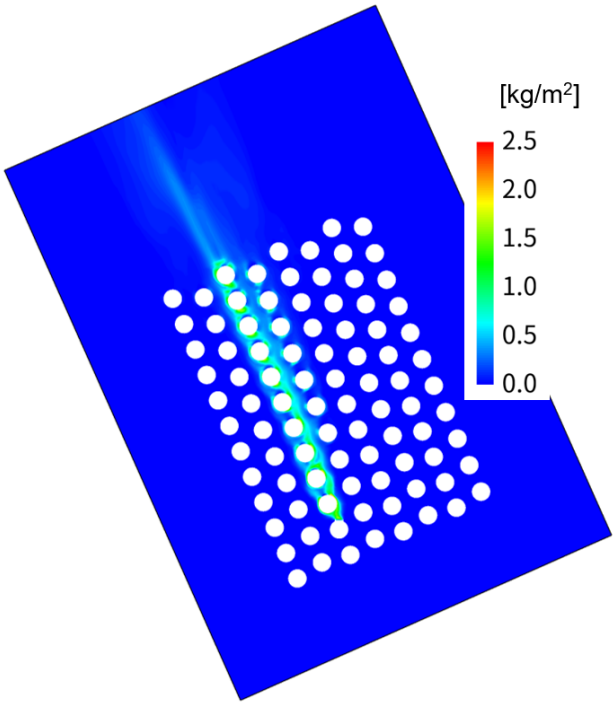

Figure 5.24 – Time-averaged NaOH from SERAPHIM during 1.0-2.0s[30]

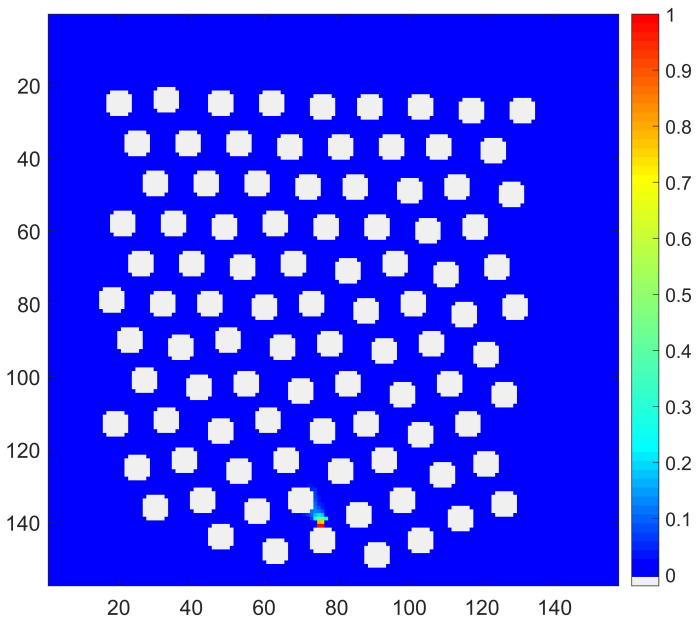

Figure 5.25 – Time-averaged volume fraction of H_2O in gaseous particles from MPS during 1.0-2.0s

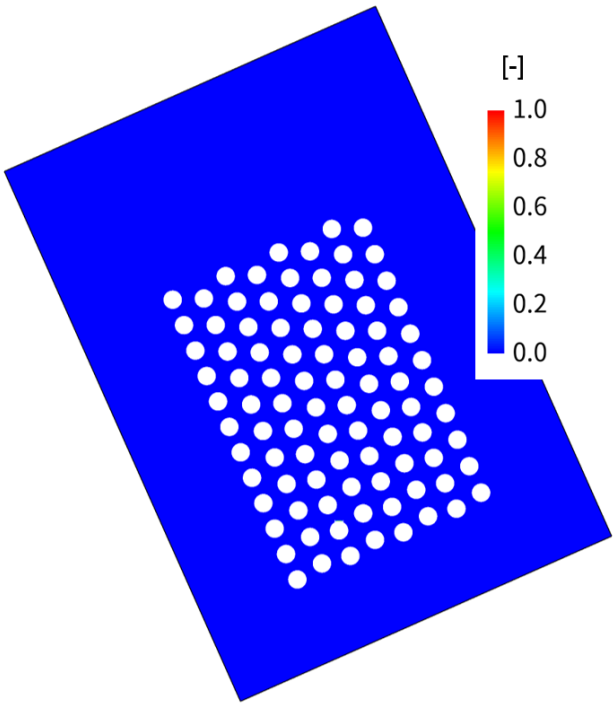

Figure 5.26 – Time-averaged volume fraction of H_2O vapor from SERAPHIM during 1.0-2.0s[30]

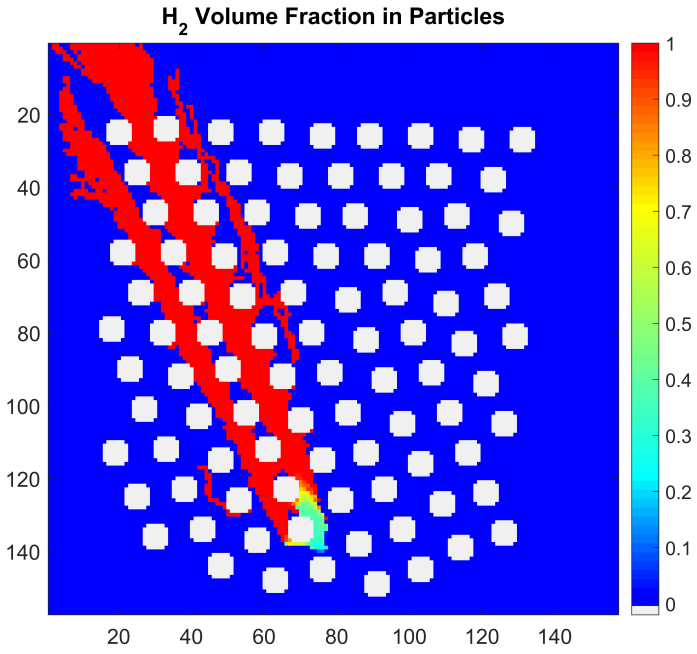

Figure 5.27 – Time-averaged volume fraction of H_2 in gaseous particles from MPS during 1.0-2.0s

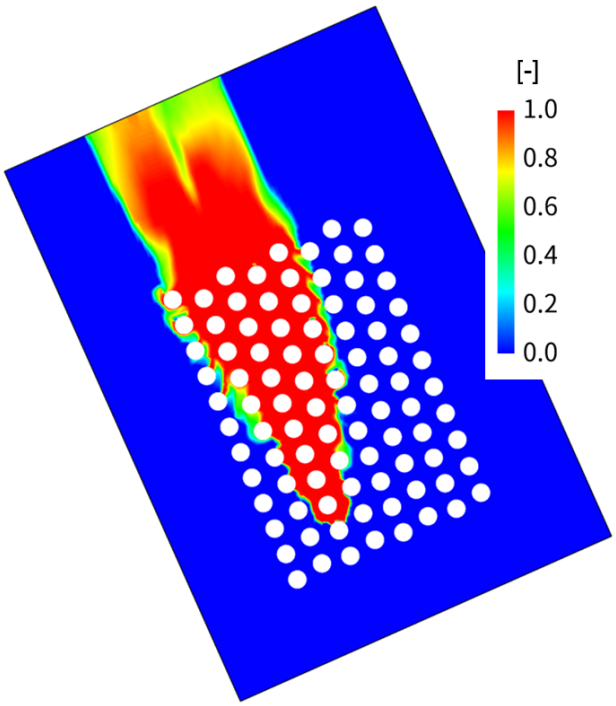

Figure 5.28 – Time-averaged volume fraction of H_2 from SERAPHIM during 1.0-2.0s[30]

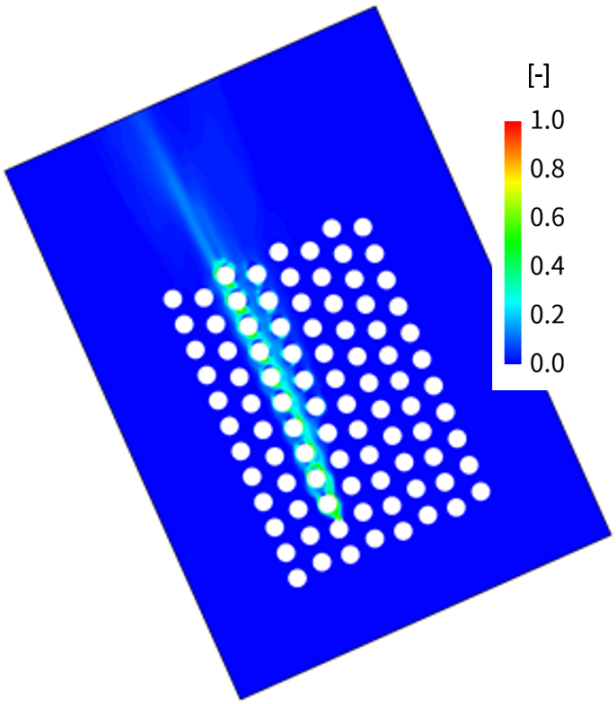

Figure 5.29 – Time-averaged void fraction from SERAPHIM during 1.0-2.0s[30]

6 Conclusions

A new methodology has been developed on the basis of MPS method with the feasibility to simulate multi-disciplinary sodium-water chemical reactions. It also has the applicability to simulate a multiphase and multi-density high-speed jet flow with stable numerical solutions.

To be specific, the particle method is proposed to using the averaging density for interfacial particles to avoid the extremely large acceleration for lighter particles. Moreover, the particle method has also been developed with the feasibility of simulate multi-component particles given a complex phenomena including many physical mechanism. The mass diffusion and heat transfer models for multi-component particles coupled with reaction models are developed and verified with the applicability for many other reaction simulation.

As a difference from other methodologies modelling the sodium-water reaction, the reaction energy in this research is calculated solely based on the enthalpy change induced the species transformation in reactions, the species diffusion, evaporation and condensation process, rather than adopting a constant reaction heat at the standard temperature.

Simulation cases presented in this work have shown the validity of the proposed methodology via the investigation on the velocity profiles, reactants and products concentration profiles, and temperature of reaction zones in sodium-water reactions. Mass and energy conservation have been verified even considering the evaporation and condensation of sodium and sodium hydroxide. Water and hydrogen mole amount distribution have presented reasonable phenomena. Furthermore, the validation of the present method has been done by the simulation in a full-scale of steam generator, which shows a good agreement with the SERAPHIM results. It indicates the proposed method of this study can promisingly provide more insights for further investigations based on the simulation results.

Bibliography

[1] Ruggieri J-M., et al., Sodium-Cooled Faster Reactor (SFR) System Safety Assessment, 2017.

[2] Takata T., Yamaguchi A., Fukuzawa K., Matsubara K., Numerical methodology of Sodium-Water Reaction with Multiphase Flow Analysis., Nucl. Sci. Eng., 2005; 140:221-236.

[3] Boardman C.E., Hui M., Neely H.H., Test Results of Sodium-Water Reaction Testing in Near Prototypical LMR Steam Generator, Proc. IARA/IWGFR Specialists' Mtg. Steam Generator Failure and Failure Propogation Experience, Aix-en-Provence, 1990, France.

[4] David, L., et al., A small scale experiment and a simplified model to investigate the runaway of sodium-water reaction, Int. J. Heat Mass Transf., 2019; 144:118542.

[5] Takata T., Yamaguchi A., Numerical approach to the safety evaluation of sodium-water reaction, J. Nucl. Sci. Technol., 2003; 40:708-718.

[6] Uchibori A., et al., Improvement of Steam Generator Tube Failure Propagation Analysis Code LEAP for Evaluation of Overheating Rupture, J. Nucl. Sci. Technol., 2019; 56:201-209.

[7] Furfaro, D., et al., Towards sodium combustion modeling with liquid water, J. Comput. Phys., 2020; 403:109060.

[8] Carnevali, S., Proust C., Soucille M., Unsteady aspects of sodium-water-air reaction, Chen. Eng. Res. Des., 2013; 91:633-639.

[9] Koshizuka S, Oka Y. Moving-particle semi-implicit method for fragmentation of incompressible fluid. Nucl. Sci. Eng. 1996; 123:421-434.

[10] Duan G., Chen B., Koshizuka S., Xiang H., Stable Multiphase Moving Particle Semi-implicit Method for Incompressible Interfacial Flow, Comput. Method Appl. M., 2017; 318:636-666.

[11] Khayyer A., Gotoh H., Enhancement of Performance and Stability of MPS Mesh-Free Particle Method for Multiphase Flows Characterized by High Density Ratios, J. Comput. Phys., 2013; 242:211-233.

[12] Chen R., et al., Three-dimensional Numerical Simulation of the HECLA-4 Transient MCCI Experiment by Improved MPS Method. Nucl. Eng. Des., 2019; 347:96-107.

[13] Kondo M, Koshizuka S. Improvement of stability in moving particle semi-implicit method. Intl. J. Numer. Meth. Fluids. 2011; 65:638-654.

[14] Shimizu Y, Gotoh H, Khayyer A. An MPS-based particle method for simulation of multiphase flows characterized by high density ratios by incorporation of space potential particle concept. Comput. Math. Appl. 2018; 76:1108-1129.

[15] Duan G, Chen B, Zhang X, Wang Y. A multiphase MPS solver for modeling multi-fluid interaction with free surface and its application in oil spill. Comput. Method Appl. M. 2017; 320:133-161.

[16] Duan G, Koshizuka S, Chen B. A contoured continuum surface force model for particle methods. J. Comput. Phys. 2015; 298:280-304.

[17] Brackbill J.U., Kothe D.B., Zemach C.. A continuum method for modeling surface tension. J. Comput. Phys. 1992; 100:335-354.

[18] Goldman R.. Curvature formulas for implicit curves and surfaces. Comput. Aided Geom. Des.. 2005; 22:632-658.

[19] Li J, Jang S, Yamaguchi A. Enhancement of Pressure and Curvature Calculation for the Moving Particle Semi-Implicit Method. Proc. 2018 26th Int. Conf. on Nucl. Eng.; 2018 Jul. 22-26; London (England). p.V008T09A037-V008T09A037.

[20] Hysing S., Turek S., Kuzmin D., Parolini N., Burman E., Ganesan S., Tobiska L.. Quantitative benchmark computations of two-dimensional bubble dynamics. Intl. J. Numer. Meth. Fluids. 2009; 60:1259-1288.

[21] Lee B., Park J., Kim M., Hwang S.. Step-by-step Improvement of MPS method in simulating violent free-surface motions and impact-loads. J. Comput. Phys. 2009; 60:1259–1288.

[22] Tanaka M, Masunaga T. Stabilization and smoothing of pressure in MPS method by quasi compressibility. Intl. J. Numer. Meth. Fluids. 2010; 229:4279–4290.

[23] Khayyer A, Gotoh H. Corrected higher order Laplacian for enhancement of pressure calculation by projection-based particle methods with applications in ocean engineering. J. Ocean Eng. Mar Energy 2015;1:361–376.

[24] Khayyer A, Gotoh H. Enhancement of stability and accuracy of the moving particle semi-implicit method. J. Comput. Phys. 2011;230:3093–3118.

[25] Bogatyrev A, Makeenkova O, Belalov V, Kucherenko M. Calculation of viscosity and diffusion coefficient in binary mixtures of dilute gases. Adv. Stud. Theor. Phys. 2017;11:283–296.

[26] Takashi T, Yamaguchi A. Numerical thermal-hydraulics study on sodium-water reaction phenomena. Proc. Int. Conf. on SNA2003'; 2003 Sep. 22-24; Paris (France).

[27] Takahashi R, Tomiyama A. [Consideration on computational method of two-phase flow problem]. Nihon-Genshiryoku-Gakkai Shi (J. At. Energy Soc. Jpn.). 1984; 26:988-998 [in Japanese].

[28] Kato K, Arae K, Narabayashi T, Ohshima H, Kurihara A. [Study on Sodium-water Reaction Phenomena in Steam Generator of Sodium-cooled Fast Reactor(21) visualization test using piping group mock up specimen for evaluation of wastage phenomena in steam generator for FBR], Proc. 2012 Annual Mtg. Atomic Energy Society of Japan; 2012 Sep. 19-21; Hiroshima (Japan) [in Japanese].

[29] A. KURIHARA et al., [Research on sodium-water reaction phenomena in steam generator of sodium-cooled commercial fast reactor (2) sodium-water reaction experiment under intermediate water leak condition," Proc. 2011 Annual Mtg. Atomic Energy Society of Japan; 2011 (in Japanese).

[30] Past Communication with A. Uchibori and W. Kosaka in JAEA; 2020.